Observation of electroweak WZjj production and studies on pile-up mitigation with the ATLAS detector

Louis Portales

▶ **To cite this version:**

Louis Portales. Observation of electroweak WZjj production and studies on pile-up mitigation with the ATLAS detector. Atomic Physics [physics.atom-ph]. Université Savoie Mont Blanc, 2020. English. NNT : 2020CHAMA023 . tel-03550156

HAL Id: tel-03550156
https://theses.hal.science/tel-03550156

Submitted on 31 Jan 2022

HAL is a multi-disciplinary open access archive for the deposit and dissemination of scientific research documents, whether they are published or not. The documents may come from teaching and research institutions in France or abroad, or from public or private research centers.

L'archive ouverte pluridisciplinaire **HAL**, est destinée au dépôt et à la diffusion de documents scientifiques de niveau recherche, publiés ou non, émanant des établissements d'enseignement et de recherche français ou étrangers, des laboratoires publics ou privés.

UNIVERSITÉ SAVOIE MONT BLANC

THÈSE

Pour obtenir le grade de

DOCTEUR DE L'UNIVERSITÉ SAVOIE MONT BLANC

Spécialité : **Physique Subatomique et Astroparticules**

Arrêté ministériel : 25 Mai 2016

Présentée par

Louis PORTALES

Thèse dirigée par **Emmanuel SAUVAN** et
codirigée par **Iro KOLETSOU**

préparée au sein du **Laboratoire d'Annecy de Physique des Particules**
dans **l'École Doctorale de Physique de Grenoble**

Observation de la production $WZjj$ électrofaible, et études sur la suppression des jets d'empilement avec le détecteur ATLAS

Observation of electroweak $WZjj$ production, and studies on pile-up mitigation with the ATLAS detector

Thèse soutenue publiquement le **1er Octobre 2020**,
devant le jury composé de :

Madame Edwige TOURNEFIER
Directrice de Recherche, LAPP, Présidente
Monsieur David CHARLTON
Professeur, Université de Birmingham, Rapporteur
Monsieur Juan ALCARAZ MAESTRE
Professeur, CIEMAT, Rapporteur
Monsieur Andreas HOECKER
Senior Scientist, CERN, Membre
Monsieur Dieter ZEPPENFELD
Professeur, Karlsruhe Institute of Technology, Membre

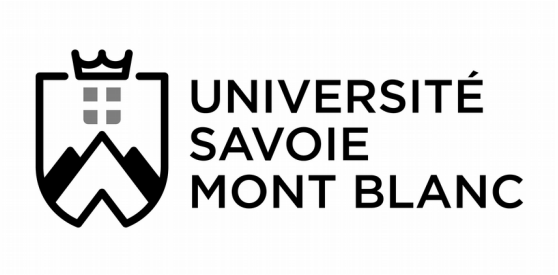
UNIVERSITÉ
SAVOIE
MONT BLANC

Acknowledgments

I would like to express my deep gratitude to all the people that helped me, and supported me, in one way or another, during the three-and-a-half years I spent at LAPP, having fun with the ATLAS experiment data.

The first persons I would like to thanks are my two supervisors, Iro Koletsou and Emmanuel Sauvan, for the incredible support throughout these three years of work, their constant availability, and the obvious passion and pleasure they constantly show to share their experience. I could not have hoped for a better supervisions.

Thanks to Francesco Costanza, with whom I closely collaborated in the last year or so, for the full Run 2 follow-up $WZjj$-EW analysis. I really enjoyed this collaboration and all the discussions that came with it.

I am also grateful to the other members of the past and present members of the LAPP diboson team, Angela Burger, Olympia Dartsi, Lucia Di Ciaccio, Corinne Goy, Narei Lorenzo Martinez and Luka Selem, for all the discussions and all the knowledge they shared with me. This extends to all the rest of the ATLAS team at LAPP. I spent an amazing period working among them. A special mention goes here to Nicolas Berger and Stephane Jezequel, for the tremendous help they provided, respectively on the statistical analysis development, and on the handling and understanding of the very complex computing framework used in ATLAS and at the IN2P3 computing center.

I would then like to thanks the people from the Jet-Etmiss performance group I have been working with, especially Matt Klein, Chris Delitszch and Steven Schramm, for all the help, and for the responsibilities they trusted me with.

Thanks to the members of my jury, Edwige Tournefier, Andreas Hoecker and Dieter Zeppenfeld, for agreeing to read my thesis, and my reviewers, Juan Alcaraz Maestre and Dave Charlton, for the detailed reading and feedback they provided on the manuscript.

Pour finir, merci à ma famille pour toujours avoir vu le meilleur en moi, et souvent plus que ça, et de m'avoir supporté jusqu'ici et de continuer à le faire quoi qu'il advienne.

Contents

Introduction **1**

1 Theoretical concepts and motivations **3**
1.1 Overview of the Standard Model of Particle Physics . . . 3
1.2 Electroweak theory and Electroweak Symmetry Breaking . . . 5
1.3 Collider phenomenology . . . 8
1.4 Diboson processes and Vector Boson Scattering . . . 12
1.4.1 Phenomenology and background contributions . . . 15
1.4.2 Signal modelling . . . 18
1.4.3 NLO corrections . . . 20
1.4.4 Experimental status of VBS searches . . . 22

2 The Large Hadron Collider and the ATLAS detector **25**
2.1 The LHC acceleration complex . . . 25
2.2 Particle collisions and luminosity . . . 27
2.3 A Toroidal LHC ApparatuS . . . 29
2.3.1 Coordinate system . . . 31
2.3.2 The Inner Detector . . . 31
2.3.3 The Electromagnetic Calorimeter . . . 33
2.3.4 The Hadronic Calorimeter . . . 35
2.3.5 The Muon Spectrometer . . . 36
2.3.6 The Trigger system . . . 37

3 Particle reconstruction **39**
3.1 Reconstruction of Electrons . . . 39
3.2 Reconstruction of Muons . . . 42
3.3 Reconstruction of Jets . . . 44
3.4 Neutrinos and the Missing Transverse Energy . . . 48

4 Identification and suppression of pile-up jets **51**
4.1 Pileup jets definitions . . . 51
4.2 The Jet-Vertex-Tagger algorithm . . . 52
4.3 The Forward Jet-Vertex-Tagger algorithm . . . 54

4.4 Improving the fJVT using jet shapes and kinematics . . . 57
4.4.1 MVfJVT development and training . . . 58
4.4.2 Performance validation . . . 63
4.5 Calibration studies for the forward taggers . . . 65
4.5.1 Calibration methodology . . . 65
4.5.2 Estimation of systematic uncertainties . . . 70
4.5.3 Calibration results . . . 74
4.5.4 Quark/gluon dependence of the MVfJVT . . . 78
4.6 Summary and discussion . . . 79

5 Observation of Electroweak $WZjj$ production and related studies 81
5.1 Event selection . . . 81
5.1.1 Lepton selection . . . 82
5.1.2 W and Z boson reconstruction . . . 84
5.1.3 Targeting VBS topology through jet selection . . . 85
5.2 Analysis methodology . . . 86
5.2.1 Background estimation . . . 86
5.2.2 Multivariate analysis for background discrimination . . . 91
5.2.3 Statistical analysis for signal extraction . . . 98
5.2.4 Estimation of systematic uncertainties . . . 102
5.3 Observation of $WZjj$-EW production with 36 fb^{-1} of data . . . 107
5.3.1 $WZjj$-EW fiducial cross-section measurement . . . 107
5.3.2 Comparison to CMS results . . . 119
5.4 Discussion and prospects . . . 123

Conclusion 125

Bibliography 129

Introduction

Vector Boson Scattering processes have been of great interest to the high-energy physics community since the beginning of the operation of the Tevatron collider, at Fermilab and LEP, at CERN, and has been one of the most sought after electroweak process at high-energy particle collider experiments since then. At this time, however, this interest was mostly driven by theoreticians, that identified the interest of these processes, especially when involving two longitudinally-polarised vector bosons [1], as a great tool to probe the electroweak symmetry breaking mechanism. From the experimental side, their study was much more challenging.

In hadron colliders, VBS processes are studied through the measurement of the rare fully-electroweak production of two bosons, associated to two hadronic jets ($VVjj$-EW). The $p\bar{p}$ collisions at $\sqrt{s} = 1.96$ TeV, and the integrated luminosity of 10 fb^{-1} provided by the Tevatron were not sufficient to access these very rare processes, and results from the CDF and DØ collaborations were limited to the inclusive diboson production [2]. The successor of the Tevatron, the Large Hadron Collider, pushed the pp collision energy up to $\sqrt{s} = 7$ TeV, then $\sqrt{s} = 8$ TeV in its first data-taking run, during which the first attempts at observing the $VVjj$-EW production were made [3, 4, 5]. However, the first observation of such processes was only made with the Run 2 of the LHC, with its increased $\sqrt{s} = 13$ TeV center-of-mass energy, and the 36 fb^{-1} of data collected in 2015 and 2016. This observation of the electroweak production of two same-sign $W^{\pm}$ bosons (ssWWjj-EW) was made first by the CMS experiment [6], with the two bosons decaying leptonically, taking advantage of the relatively high cross-section, and low irreducible background of this specific process.

This thesis work started shortly after this observation was published, and no other $VVjj$-EW process had been observed. The choice is made to study the fully-leptonic $WZjj$-EW production, that benefits from a cleaner final state than ss$WWjj$-EW, with three charged leptons and a neutrino originating from the W and Z decays, hence lower background arising from the final state lepton misidentification. However, its production cross-section is lower, and it is much more impacted by irreducible background, mainly from the $WZjj$-QCD production. A large part of this study regards the optimisation of the separation between the $WZjj$-EW and $WZjj$-QCD productions. Additional studies are made, concerning the suppression of pileup jets in the difficult forward detector region, in which no tracking information is available. The impact from such jets is found to be negligible in the present study, but their suppression is expected to play an important role in future $WZjj$-EW studies, as the signal topology, with its two forward tagging jets, could be easily mimicked due to pileup-jets being wrongly

selected.

The following chapters present and motivate the various studies performed, that allowed, and completed, the first observation of the $WZjj$-EW production [7]. In Chapter 1, the theoretical motivations and status of VBS studies are described. Chapter 2 presents the experimental setup for these studies, which consists of the LHC and the ATLAS detector. It is completed, in Chapter 3, by a description of the particle reconstruction methods that are employed to transform the raw data collected with ATLAS into actual information on the particles kinematics.

Chapter 4 details the studies performed on the development and characterisation of the forward pileup-jet tagging tools. In this chapter, Sections 4.1 to 4.3 contain descriptions of concepts and tools used as the basis for the personal work presented in Sections 4.4 and 4.5.

Chapter 5 finally details the analysis developed for the observation of the $WZjj$-EW production. The large majority of the points discussed in this chapter are personal contributions, and these are given in more detail in its introduction.

Chapter 1

Theoretical concepts and motivations

This chapter lays the theoretical foundations helpful in understanding the studies described in this thesis. In the first section, some useful concepts related to the Standard Model of particle physics are exposed, followed by a description of the electroweak theory that directly motivated the study of the $WZjj$ production. The following section describes more general concepts related to the high-energy particle collider phenomenology, that are required to understand some of the features of the observed collision events. The last section focuses on the specifics of diboson production, and vector boson scattering, and aims at motivating, and contextualizing the related studies, presented in Chapter 5.

1.1 Overview of the Standard Model of Particle Physics

The Standard Model (SM) is a Quantum Field Theory that describes the composition of the universe and the interactions between particles at the most fundamental scale. It has been successful, so far, at predicting the results from the measurements performed in the past 50 years of the parameters it constrains, with few noticeable exceptions that are not yet significant.

From the least abstract point of view, the SM predicts the existence of a relatively small number of fundamental particles, and their properties. These particles are classified as either fermions, or bosons, depending on what statistics they obey, that are respectively the Fermi-Dirac and Bose-Einstein statistics.

Fermions are the particles composing matter. They all have a half-integer spin, and obey the Pauli exclusion principle, that forbids the superposition of two of them in the same quantum state. The SM predicts the existence of 12 fermions, that can be further classified as quarks and leptons. A summary of their names and properties is given in Table 1.1

The quarks are electrically-charged particles, with a charge $q = +\frac{2}{3}e$, for the so-called up-type quarks, or $q = -\frac{1}{3}e$ for down-type quarks, and are paired into three generations, each containing one up-type and one down-type quark. The first-generation of quark, the up-quark (u) and down-quark (d), are the constituents of protons (uud), and neutrons (udd).

	Category Charge [e]	1^{st} generation	2^{nd} generation	3^{rd} generation
Quarks	up-type $q = +\frac{2}{3}$	up (u) $m = 2.16$ MeV	charm (c) $m = 1.27$ GeV	top (t) $m = 172.4$ GeV
	down-type $q = -\frac{1}{3}$	down (d) $m = 4.67$ MeV	strange (s) $m = 93$ MeV	bottom (b) $m = 4.18$ GeV
Leptons	Charged $q = +1$	electron (e) $m = 0.511$ MeV	muon (μ) $m = 105.7$ MeV	tau (τ) $m = 1.8$ GeV
	Neutral $q = 0$	e-neutrino (ν_e) $m \simeq 0$	μ-neutrino (ν_μ) $m \simeq 0$	τ-neutrino (ν_τ) $m \simeq 0$

Table 1.1: Summary of the fermions predicted in the SM and their properties. The uncertainties on the masses are not shown, but are available in Ref. [8].

The two other generations are composed of more exotic quarks, that are typically only created in high energy phenomena in nature, or in particle colliders. These are the charm- (c) and strange-quarks (s) for the second generation, and top- (t) and bottom-quarks (b) for the third.

Mirroring the quarks, three generations of leptons exist, each of these being composed of a charged, massive particle, and a neutral, light particle. The massive leptons are the electron (e), that, associated to protons and neutrons, forms the atoms, and the muon (μ) and tau-lepton (τ). The corresponding neutral particles are commonly referred to as neutrinos, but have distinct properties depending on their generation.

For both quarks and leptons, the second-generation particles have larger masses than those of the first generation, and similarly, the third-generation particles are the heaviest. For each of these twelve particles, a corresponding anti-particle exists. It is characterised by the exact same properties as its corresponding particle, to the exception of its opposite electric charge.

The bosons are integer-spin particles, either spin-1 for the vector bosons, that are the carriers of the gauge interactions between fermions, or spin-0 for the scalar Higgs boson. The most famous vector boson certainly is the photon (γ). It is massless, and neutral and is the carrier of the electromagnetic interaction between two electrically charged particles. The strong interaction, responsible of the cohesion of quarks forming, for instance, the protons and neutrons, is carried by gluons. Finally, the $W^{\pm}$ and Z^0 are massive bosons, and the carriers of the weak interaction, responsible of the decays of particles. These vector bosons cover all the known interactions, to the exception of gravity, whose description does not enter the SM. The Higgs boson is also predicted, as a consequence of the existence of the Higgs field, which explains the mass of the fermions and weak-interaction bosons, through the Higgs mechanism, that is described in Section 1.2.

All of the SM particle content and interactions can be expressed more formally through the concepts of symmetries and gauge invariance. For that purpose, every single particle is more conveniently represented by a quantum field. Taking the example of Quantum Electrodynamics (QED), that describes the electromagnetic interaction, one can write the Lagrangian representing the behaviour of a freely propagating fermion

$$L_0 = \bar{\psi} i\gamma^\mu \partial_\mu \psi - m\bar{\psi}\psi \,, \tag{1.1}$$

where $\psi(x,t)$ is the fermion field, γ^μ are gamma matrices and ∂_μ the differential operator, and m is the fermion mass. The Einstein convention is used here, with the indices $\mu = 0,1,2,3$ representing the space-time components x and t.

In order for QED to be valid as a gauge theory, this Lagrangian has to be invariant under the $U(1)$ gauge transformation $\psi \to e^{i\alpha}\psi$. For this condition to be verified, a term must be added to the Lagrangian, which now takes the form

$$L_{\text{QED}} = \bar{\psi} i\gamma^\mu \partial_\mu \psi - m\bar{\psi}\psi - e\bar{\psi}\gamma^\mu \psi A_\mu - \frac{1}{4} F_{\mu\nu} F^{\mu\nu} \,. \tag{1.2}$$

In this new expression, the gauge field A_μ is introduced, representing the photon, with the third term of the expression translatable into the interaction between a photon, a fermion and its anti-particle. The fourth term encodes the kinematics of the newly introduced photon field, with $F^{\mu\nu}$ that can be expressed as

$$F^{\mu\nu} = \partial^\mu A^\nu - \partial^\nu A^\mu \,. \tag{1.3}$$

1.2 Electroweak theory and Electroweak Symmetry Breaking

The electroweak (EW) theory provides a unified description of both the electromagnetic and weak interactions. It is obtained by replacing the $U(1)$ symmetry defining QED, requiring instead a $SU(2)_L \times U(1)_Y$ invariance, where the symmetry under a $U(1)_Y$ transformation mimics that of the QED, with the weak hypercharge Y taking the role of the electric charge e, and $SU(2)_L$ introduces the weak isospin T. These can be related to the electric charge Q through the Gell-Mann-Nishijima relation [9]

$$Q = T_3 + \frac{Y}{2} \,, \tag{1.4}$$

where T_3 is the third component of the isospin T.

The concept of chirality is also introduced, with a distinction between the left-handed fermion doublets, and the right-handed singlets

$$\begin{pmatrix}\nu_e\\ e\end{pmatrix}_L \ , \ \begin{pmatrix}\nu_\mu\\ \mu\end{pmatrix}_L \ , \ \begin{pmatrix}\nu_\tau\\ \tau\end{pmatrix}_L \ , \ e_R \ , \ \mu_R \ , \ \tau_R \ , \tag{1.5}$$

and

$$\begin{pmatrix}u\\ d\end{pmatrix}_L \ , \ \begin{pmatrix}c\\ c\end{pmatrix}_L \ , \ \begin{pmatrix}t\\ b\end{pmatrix}_L \ , \ u_R \ , \ d_R \ , \ c_R \ , \ ... \tag{1.6}$$

Following the same methodology as for QED, imposing its gauge invariance, the EW Lagrangian can be written as

$$L_{EW} = \bar{\psi} i\gamma^\mu \partial_\mu \psi - \frac{1}{4} F_{\mu\nu} F^{\mu\nu} - eY\bar{\psi}\gamma^\mu B_\mu \psi - g_W Y \bar{\psi}\gamma^\mu (T \cdot W_\mu)\psi - \frac{1}{4} W^i_{\mu\nu} W^{i\mu\nu} \ . \tag{1.7}$$

The first two terms are similar to L_{QED}. However, the term representing the coupling of fermions to photons is replaced by more general terms, and the W_μ and B_μ fields are introduced. The two charged vector bosons $W^\pm$ appear as linear combinations of the W_μ field components, $W^\pm_\mu = \frac{1}{\sqrt{2}}(W^1_\mu \mp W^2_\mu)$, while the photon is now created through the mixing of the B_μ and W_μ fields, as

$$A_\mu = B_\mu \cos\theta_W + W^3_\mu \sin\theta_W \ , \tag{1.8}$$

where θ_W is the weak mixing angle, and the Z_μ field, corresponding to the Z^0 boson, is generated similarly as

$$Z_\mu = -B_\mu \sin\theta_W + W^3_\mu \cos\theta_W \ . \tag{1.9}$$

In addition to introducing these new vector bosons, the non-Abelian nature of the $SU(2)_L$ group requires their self-couplings. Two types of couplings are predicted there: the triple gauge coupling (TGC) and quartic gauge couplings (QGC). These are represented in Figure 1.1. Note that the SM does not allow all combinations of vector bosons, and most notably forbids the couplings between three or four neutral gauge bosons at tree level.

Another important feature of L_{EW} at this stage is that no mass term is introduced for the two newly appearing bosons, while experimental observations [10, 11] were found that indicate they were massive. Additionally, the fermion mass term that appeared in L_{QED} is now absent, requiring the introduction of an additional mechanism to explain the origin of their mass. This is handled through the process of Electroweak Symmetry Breaking (EWSB),

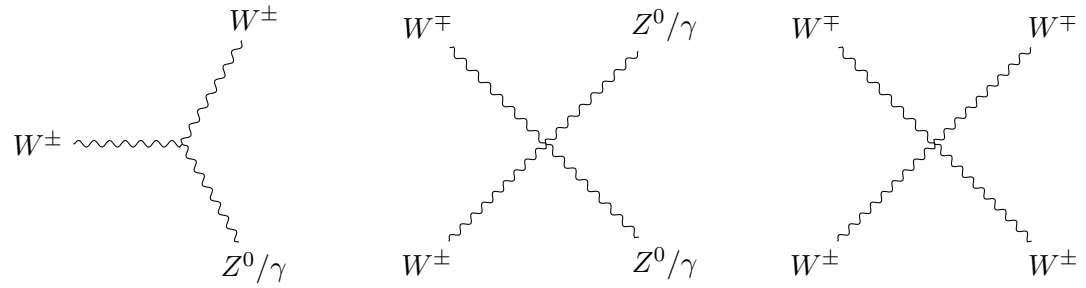

Figure 1.1: Feynman diagrams for the triple and quartic gauge couplings allowed in the SM.

and the introduction of the Higgs mechanism.

In this process, the weak-bosons masses are not introduced as additional terms in the Lagrangian, that would break its gauge invariance. Through spontaneous symmetry breaking, the mass of particles can instead be generated by introducing a new scalar field

$$\Phi = \begin{pmatrix} \Phi_+ \\ \Phi_0 \end{pmatrix} , \tag{1.10}$$

and its associated Lagrangian terms

$$L_\Phi = (D^\mu \Phi)^\dagger (D_\mu \Phi) - V(\Phi) , \tag{1.11}$$

where

$$V(\Phi) = \mu^2 |\Phi^\dagger \Phi| + \lambda |\Phi^\dagger \Phi|^2 . \tag{1.12}$$

In the Lagrangian expression, D^μ is the covariant derivative, whose introduction is part of the requirements for the preservation of the EW Lagrangian gauge invariance. The potential $V(\Phi)$ can behave in different ways, depending on the sign of μ^2. For $\mu^2 > 0$, a single ground state is found for $\Phi_0 = 0$. However, for $\mu^2 < 0$, the potential minima are not zero any more, but constitute a degenerated distribution at $\Phi_0^2 = \frac{-\mu^2}{2\lambda} \equiv \frac{v^2}{2}$, with $v \simeq 246$ GeV , following a rotational symmetry around $\Phi = 0$, as illustrated in Figure 1.2. As the field will always tend to its energy minimum, a vacuum state is chosen among these degenerated states, thus breaking the rotational symmetry. This vacuum state is chosen such that the $U(1)$ symmetry from QED is preserved while breaking the $SU(2)_L \times U(1)_Y$ symmetry, and is written as

$$\langle \Phi_0 \rangle = \frac{1}{\sqrt{2}} \begin{pmatrix} 0 \\ v \end{pmatrix} . \tag{1.13}$$

From this mininimum state, the scalar field can be rewritten in the frame of perturbation

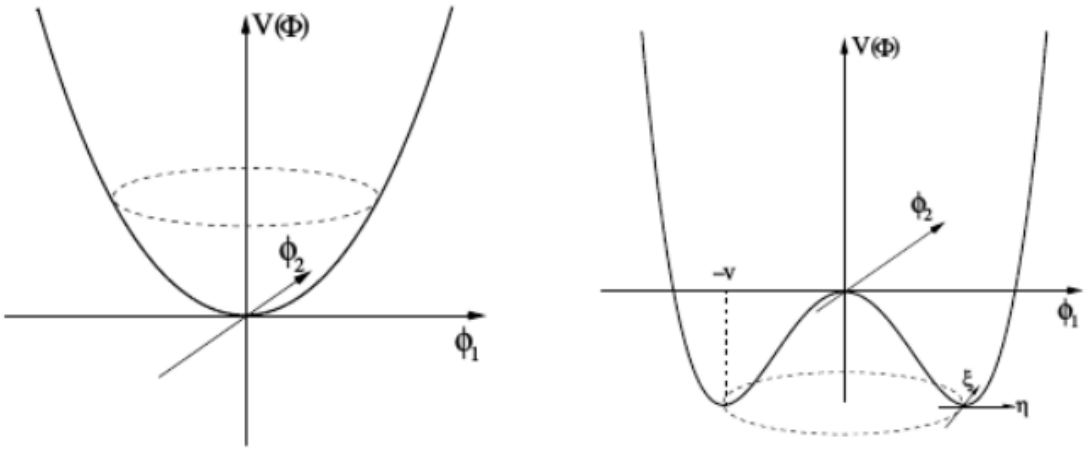

Figure 1.2: Schematic representation of $V(\Phi)$ for $\mu^2 > 0$ (left) and $\mu^2 < 0$ (right).

theory as

$$\langle \Phi \rangle = \frac{1}{\sqrt{2}} \begin{pmatrix} 0 \\ v + H(x) \end{pmatrix} , \tag{1.14}$$

where $H(x)$ is a perturbation around the vacuum expectation value. Through the breaking of the $SU(2)_L \times U(1)_Y$, the $W^{\pm}$ and Z bosons are generated, with no mass [12]. Three massless spin-0 Goldstone bosons are also generated in the process [13]. These bosons are then absorbed by the $W^{\pm}$ and Z bosons, which aquire a longitudinal polarisation component, and consequently become massive.

Introducing the new form of the field Φ into the Lagrangian from Equation 1.11 also predicts the existence of an additional massive particle, the Higgs boson, as well as its couplings to the other SM particles. This new scalar boson was observed with the ATLAS [14] and CMS [15] experiments in 2012, about 50 years after its prediction [16, 17].

1.3 Collider phenomenology

The production and study of massive vector bosons can be made thanks to particle collider experiments. Currently, the main experiments that allow such study are the ATLAS and CMS detectors, benefiting from the proton-proton (pp) collisions provided by the Large Hadron Collider (LHC).

As mentioned in Section 1.1, protons are composite particles, made of three quarks (q),

two up-quarks and one down-quark, bound together by gluons. Additionally, these gluons can generate $q\bar{q}$ pairs through energy fluctuations, referred to as sea quarks. All these particles, both quarks and gluons, can be collectively referred to as partons. These protons are packed into bunches and accelerated to ultra-relativistic momentum, before being collided at the center of the detectors. The energy of such collision is typically expressed as the square-root of the Mandelstam variable s, representing, in the case of the LHC, the center-of-mass energy of the two colliding protons. During these collisions, the components from two protons belonging to two of these bunches can interact. In the energy regime provided by the LHC, the QCD factorisation theorem [18] tells us that the proton collisions can be factorized into parton-level hard-scattering processes, whose occurrence probabilities are weighted by the parton distribution functions (PDF), reflecting the partons momentum distribution within the protons. The PDF are determined specifically for the probed energy regime using experimental data, and can be extrapolated to different energy regimes through the so-called DGLAP evolution equations [19, 20, 21]. This is done through large-scale combinations of results on probe processes from many deep-inelastic scattering (DIS) experiments, such as the ep experiments H1 and ZEUS at the HERA collider [22].

A large variety of PDF sets exists, determined using data from different experiment, and using different fitting methods. Results from the HERA experiments and from hadron colliders such as the Tevatron were originally used for the definition of PDF sets used in early LHC analyses [23, 24]. More recent updates combine these results with data from the LHC experiments are used in present LHC data simulation, with, for instance, the CT14 [25], NNPDF 3.0 [26] or MMHT14 [27] sets.

Some differences can be seen between the predictions from different PDF sets, as illustrated in Figure 1.3. This Figure compares the parton energy fraction dependence of the u-quark PDF as predicted by the three most recent PDF sets used in ATLAS at the energy scale $Q^2 = 100$ GeV^2. Some disagreements can be observed between the sets, as well as relatively large uncertainties attributed to the PDF sets themselves. These can have varying impacts depending on the final state that is studied, and require specific care in the evaluation of the PDF uncertainties. More details, specific to this thesis, are given in Section 5.2.4.

According to the QCD factorisation theorem, the cross section for the scattering of two protons A and B to create a final state F can be written as

$$\sigma(AB \to F + X) = \sum_{a,b} \int dx_1 dx_2 f_{a/A}(x1, \mu_F^2) f_{b/B}(x_2, \mu_F^2) \hat{\sigma}_{ab\to F}(x_1, x_2, \mu_R^2) \,, \tag{1.15}$$

where a and b are the partons constituting the protons A and B, and $f_{a/A}$ and $f_{b/B}$ the corre-

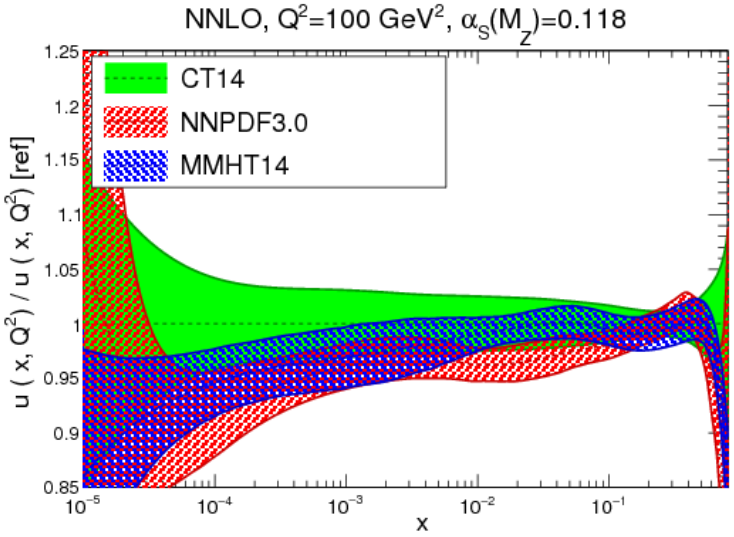

Figure 1.3: u-quark PDF comparison for the three PDF sets CT14, NNPDF 3.0 and MMHT14 at the energy scale $Q^2 = 100$ GeV^2. The PDF are normalised to the one obtained with CT14. [28]

sponding PDF, depending on the the parton energies $x_{1,2}$ and the factorisation scale μ_F^2, typically chosen to match the energy scale of the process studied.The last term, $\hat{\sigma}_{ab\to F}(x_1, x_2, \mu_R^2)$, represents the actual cross section of the process $ab \to F$, considering only the two partons in the initial state. It is evaluated based on the Feynman diagrams of the process of interest up to a given order in perturbation theory, with the Leading Order (LO) prediction typically being insufficient to properly describe the observation. The computation order can be expressed in terms of the coupling constants, with, for instance, for a process of $\mathcal{O}(\alpha^n \alpha_s^m)$ at LO, the next-to-leading-order (NLO) corrections that can be split into the NLO-EW corrections at $\mathcal{O}(\alpha^{n+1}\alpha_s^m)$ and the NLO-QCD corrections at $\mathcal{O}(\alpha^n \alpha_s^{m+1})$, with α and α_s respectively representing the electroweak and QCD coupling constants. This cross-section depends on an additional scale parameter μ_R called the renormalisation scale, that has to be considered in order to insure the non-divergence of the process, and is typically chosen to match the energy of the measured interaction. An example of such a scattering process is shown in Figure 1.4. Finally, X represents the remnants of the pp interactions that do not participate to the actual hard-scattering process, and are not accounted for in the left-side of the equation. Such interactions can occur between the remnants of the initial state protons, referred to as beam remnants. In addition, the initial state particle can spontaneously radiate a variety of partons and leptons, that have to be included as well for a proper description of the observations. These contributions to the observed event are collectively referred to as the underlying event.

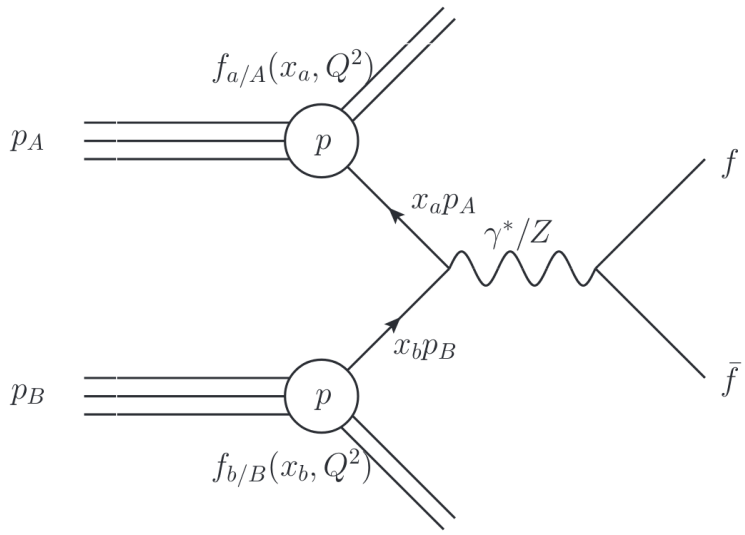

Figure 1.4: Illustration of cross-section calculation in a proton-proton collision at the LHC.[29]

One also has to take into account the hadronisation of partons, that cannot exist freely due to the low-energy QCD confinement. Partons produced during a collision event will radiate additional partons, for instance by splitting into quark-antiquark pairs recursively, until the produced parton have low-enough energies to bound into hadrons. In a similar way, final state leptons and photons undergo electromagnetically-driven cascading decays, with electrons radiating photons, and photons splitting into charged lepton pairs, until their energy becomes low enough to prevent such decays. These particle showers are simulated using the so-called parton-shower algorithms [30], which, although the name suggests otherwise, do simulate both partonic, and electromagnetic showers. In this thesis work, three distinct parton-shower algorithms are used, and overlaid to the processes predictions. These are SHERPA [31] and Herwig [32], both based on the cluster approximation [33], and PYTHIA [34] that uses instead the Lund model [35] for the hadronisation modelling.

The parton-shower overlay to LO predictions of the hard-scatter process is done in a straightforward way, by defining the energy threshold below which final state particles are accounted for in the parton-shower algorithm to correspond to the minimum energy of particles generated through the matrix element computation, in order to avoid double-counting of the final state particles. In the case of higher-order computation, such double counting can arise naturally due to the high-order term introducing parton radiations, and additional care has to be taken in order to avoid it.

A more complete picture of a full LHC event, including all the components mentioned

previously, is shown in Figure 1.5.

1.4 Diboson processes and Vector Boson Scattering

Diboson production has been extensively studied at the LHC since the beginning of its operation [36]. A common motivation for all these studies is the access to the trilinear boson self-coupling, that can be used to precisely test the SM predictions, as well as to constrain new physics models. For more practical reasons, their precise measurement can be of critical importance for Higgs production studies, as they help improving the control of very important backgrounds, with, for instance, the ZZ [37, 38] and W^+W^- [39, 40] productions closely resembling the $H \to ZZ^*$ [41] and $H \to WW^*$ [42] production modes. One can also use diboson final states in order to perform direct search of exotic resonances [43, 44], following new physics models predicting the decay of such particle into a pair of vector bosons that could rise, for instance, from mechanisms to include gravity to SM interactions [45].

The boson polarisation is also among the powerful SM parameters that can be tested in such processes, as done, for instance in the inclusive WZ measurement from ATLAS [46], as the existence of longitudinally polarised vector bosons is a direct consequence of the electroweak symmetry breaking. This last point is especially relevant for the subset of diboson processes studied in this thesis work, in which the vector bosons are scattering onto each other (VBS), as the unitarity of the scattering process of two longitudinally polarised vector bosons V_LV_L is only ensured if considering diagrams involving the exchange of a Higgs boson. In addition to the access to triple gauge coupling, their study allows a direct access to the quartic gauge boson coupling, that can only be studied through the VBS processes and the rarer triboson production.

A variety of Feynman diagrams can be drawn to represent the production of a pair of vector boson in a pp collision. The main diboson diagrams at LO do not contain any additional final state particles not originating from the decay of one of the two bosons. In the case of VBS processes, however, five diagrams exist at LO, and they all have in common two final-state quarks accompanying the bosons. These diagrams are shown in Figure 1.6. The final state is composed of two bosons $V = Z^0, W^\pm, \gamma$ and two quark-initiated jets, typically referred to as tagging jets. VBS processes always include two qqV vertices, and either a $WWVV$ vertex or two WWV vertices at LO. Neutral triple and quartic gauge couplings, involving only Z bosons or photons, are forbidden in the SM. This prevents, for instance, the scattering process $\gamma\gamma \to \gamma\gamma$ at tree level. It can however occur through the process involving a fermionic loop in place of the direct vector boson coupling. This process is not considered in the definition of

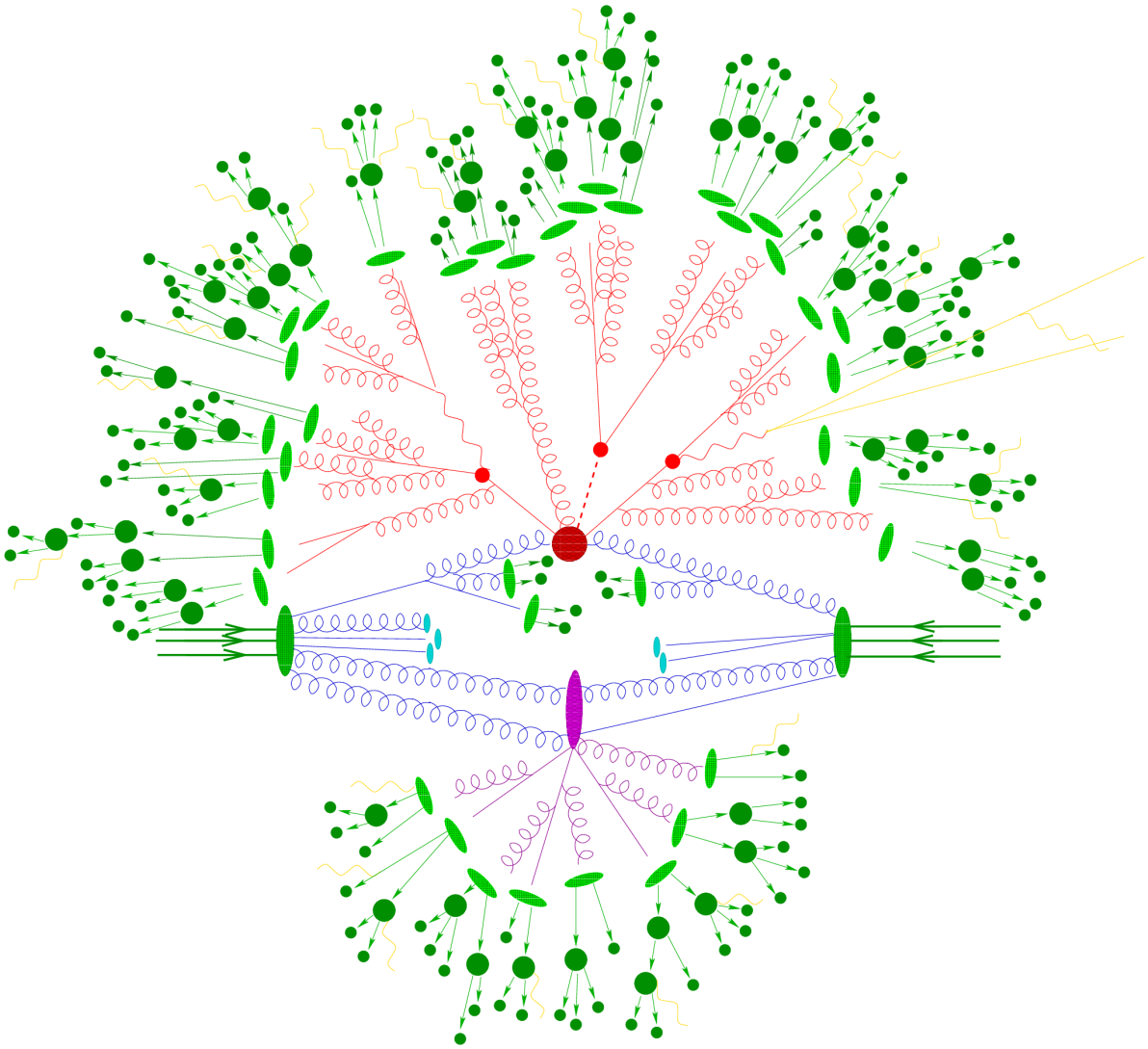

Figure 1.5: Sketch of a hadron-hadron collision as simulated by a Monte-Carlo event generator. The red blob in the center represents the hard collision, surrounded by a tree-like structure representing Bremsstrahlung as simulated by parton showers. The purple blob indicates a secondary hard scattering event. Parton-to-hadron transitions are represented by light green blobs, dark green blobs indicate hadron decays, while yellow lines signal soft photon radiation.[30]

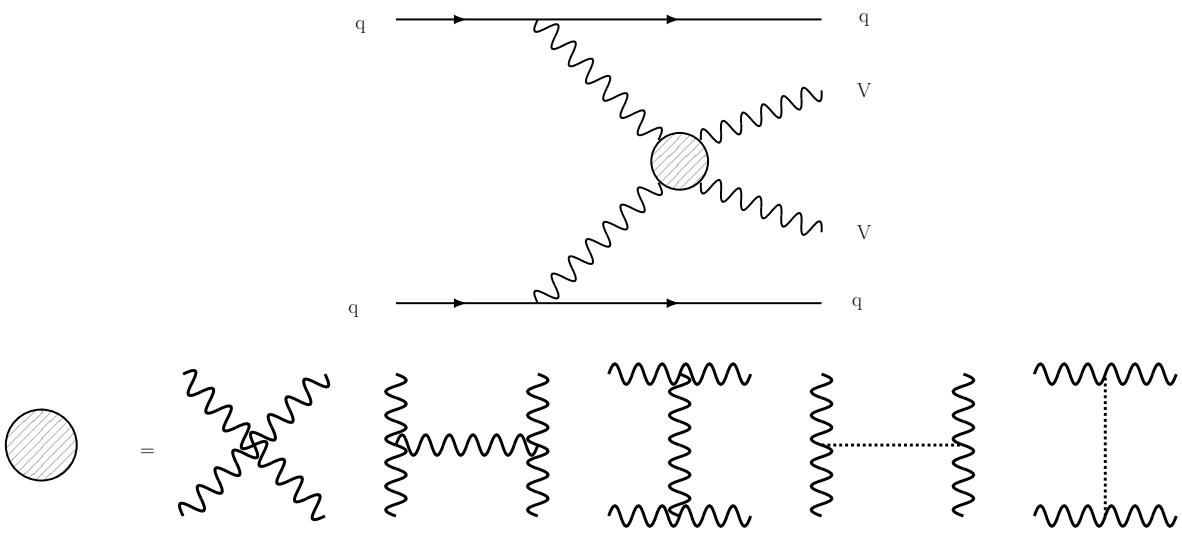

Figure 1.6: Feynman diagrams for Vector Boson Scattering processes.

VBS, and is commonly referred to as light-by-light scattering [47].

VBS processes are $\mathcal{O}(\alpha^4)$ processes. In the following, in cases where two heavy vector bosons are found in the final state, the process is described as $\mathcal{O}(\alpha^6)$, accounting for the boson decays. Additional diagrams produce identical final states, and are of the same order in α. These cannot be generated separately from the VBS diagrams without breaking the gauge-invariance. Therefore, the study of VBS processes is limited to the broader study of the electroweak production of the $VVjj$ final state ($VVjj$-EW), that includes the non-VBS diagrams, such as those presented in Figure 1.7.

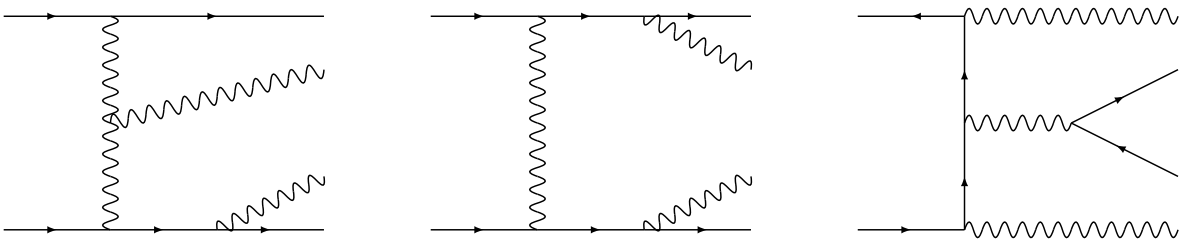

Figure 1.7: Representative $\mathcal{O}(\alpha^6)$ non-VBS diagrams contributing to the $VVjj$-EW production. The right-most diagram shows an example of VVV diagram, with one boson decaying into a $q\bar{q}$ pair.

Heavy vector bosons produced in pp collision have a very short lifetime, and are not directly detectable by the LHC experiment. Instead, their decay products are used to reconstruct

them. Both $W^{\pm}$ and Z bosons can decay either leptonically or hadronically. The latter is more frequent, representing about 70 % of the occurring decays. For W-bosons, the remaining fraction is split equally between the decays into the three lepton flavours (e, μ, τ), and their associated neutrino. In the case of Z-bosons, only a small fraction of about 10 % of the decays result in the production of a $\ell^+\ell^-$ ($\ell = e, \mu, \tau$), while the remaining 20 % decay into $\nu_\ell\bar{\nu}_\ell$. Although both the $Z \to \ell^+\ell^-$ and $Z \to \nu_\ell\bar{\nu}_\ell$ are technically both leptonic decay modes, this name is generally only used for the former, and the decays into a pair of neutrino is often referred to as "invisible decay", due to the large technical differences in the reconstruction methods employed. Despite the fact that hadronic and invisible decays are more common, the leptonic decay modes are the ones yielding the best sensitivity for measurement, due to their much higher reconstruction efficiencies and resolution. However, this is not true for bosons decaying to τ leptons, as these are also affected by a short life-time, and decay either hadronically or leptonically, rendering their reconstruction much more complex than that of electrons and muons. For that reason, the leptonic decay definition that will be employed for the rest of this document will only include the decays into the first two generations of leptons, e and μ.

1.4.1 Phenomenology and background contributions

Electroweak $VVjj$ events benefit from a very typical topology, as illustrated in Figure 1.8. It is mainly identifiable by the two tagging jets, that are emitted at large angle with respect to the transverse plane passing through the interaction point, and to which a large dijet invariant mass can be associated, and by the more central emission of the vector bosons, and by extension of their decay product. This latter point is often characterised with the so-called Zeppenfeld variable [48],

$$z^*_{VV} = \eta_{VV} - \frac{\eta_{j1} + \eta_{j2}}{2}, \tag{1.16}$$

or variations of it, where η_{VV}, η_{j1} and η_{j2} are the pseudorapidities of the diboson system VV, and of the first and second tagging jets respectively. The pseudorapidity is an angular quantity that can be defined with respect to the particles momentum as

$$\eta = \frac{1}{2}\ln\left(\frac{|p| + p_z}{|p| - p_z}\right), \tag{1.17}$$

and for which more details are given in Section 2.3.1.

The Zeppenfeld variable, also referred to as centrality, measures how centrally the boson system is emitted with respect to the two tagging jets. In the presented $WZjj$-EW analysis,

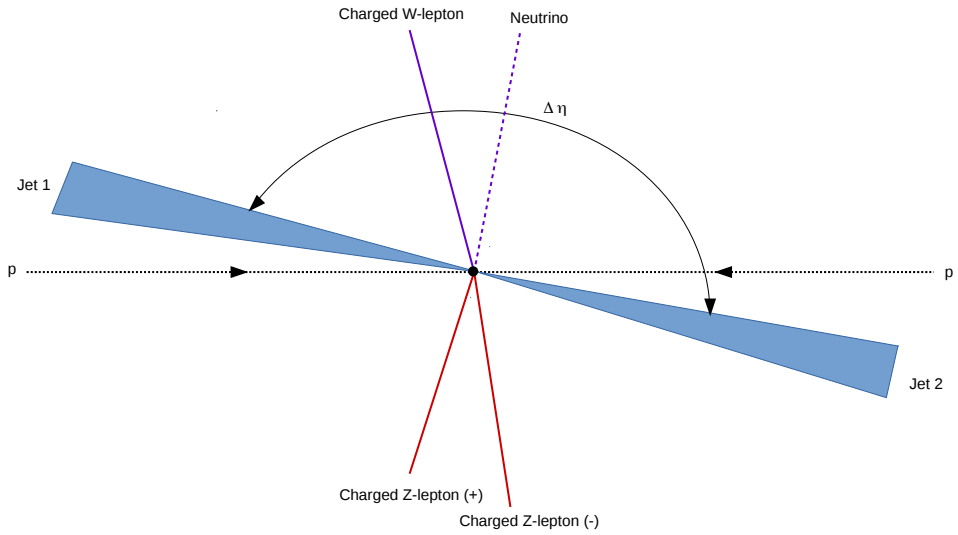

Figure 1.8: Schematic representation of a $WZjj$-EW event from a pp collision.

the lepton centrality ζ_ℓ is preferred as it does not depend on the neutrino kinematics, and is defined as

$$\zeta_\ell = \min(\Delta\eta_-, \Delta\eta_+), \tag{1.18}$$

with

$$\begin{aligned} \Delta\eta_- &= \min(\eta_\ell^W, \eta_{\ell 1}^Z, \eta_{\ell 2}^Z) - \min(\eta_{j1}, \eta_{j2}), \\ \Delta\eta_+ &= \max(\eta_{j1}, \eta_{j2}) - \max(\eta_\ell^W, \eta_{\ell 1}^Z, \eta_{\ell 2}^Z). \end{aligned} \tag{1.19}$$

The three most promising channels for VBS the studies are the leptonic same-sign $WWjj$-EW (ss$WWjj$-EW) , $WZjj$-EW, and $ZZjj$-EW. The cross sections for these processes are compared in Table 1.2, for the VBS-enriched phase-space [49], defined with the final state leptons satisfying $p_{\mathrm{T}} \geq 25$ GeV, $|\eta| < 2.5$, $\Delta R(\ell, \ell) \geq 0.3$ and $m_{\ell\ell} \geq 20$ GeV for the charged lepton pairs, and the two tagging jets having $p_{\mathrm{T}} \geq 30$ GeV, $|\eta| < 4.5$, $\Delta R(j, \ell) \geq 0.3$ and, most importantly, $m_{jj} \geq 500$ GeV and a rapidity difference of more than 2.4. The ss$WWjj$-EW production benefits from the highest overall cross-section, while that of the $ZZjj$-EW production is about four times smaller, and the $WZjj$-EW production cross section lies in between these first two.

Table 1.2: Cross sections for the electroweak production of the final states associated to the leptonic ss$WWjj$, $WZjj$ and $ZZjj$ decays, calculated with SHERPA for the VBS-enriched phase space defined in the text.[49]

Process	$W^{\pm}W^{\pm}jj \to \ell'^{\pm}\ell^{\pm}\nu_{\ell}\nu_{\ell'}$	$WZjj \to \ell^{+}\ell^{-}\ell'^{\pm}\nu_{\ell'}$	$ZZjj \to \ell^{+}\ell^{-}\ell'^{+}\ell'^{-}$
$\sigma(pp \to X)$ [fb]	3.97	2.34	0.098

The requirements made on the jet kinematics are highly contributing to the reduction of the contamination from important background processes. A first threshold around $m_{jj} > 150$ GeV, for instance, highly reduces the contribution of the triboson production (VVV), exemplified in Figure 1.9, that can yield the same final state, with four leptons and two hadronic jets in the event, if one of the boson decays hadronically.

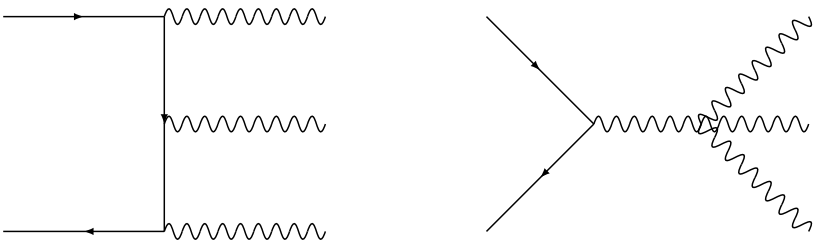

Figure 1.9: Representative $\mathcal{O}(\alpha^6)$ diagrams contributing to the VVV production.

The two jets originating from this boson would have an invariant mass close to the mass of the decaying boson, hence being suppressed by the m_{jj} criteria. More importantly, the higher threshold typically applied at $m_{jj} > 500$ GeV allows to remove a large part of the background processes producing the same final state but not through the purely-electroweak diagrams defining the signal.. Such processes, referred to as the $VVjj$-QCD backgrounds, are of order $\mathcal{O}(\alpha^4\alpha_s^2)$. Some of the corresponding diagrams are shown in Figure 1.10.

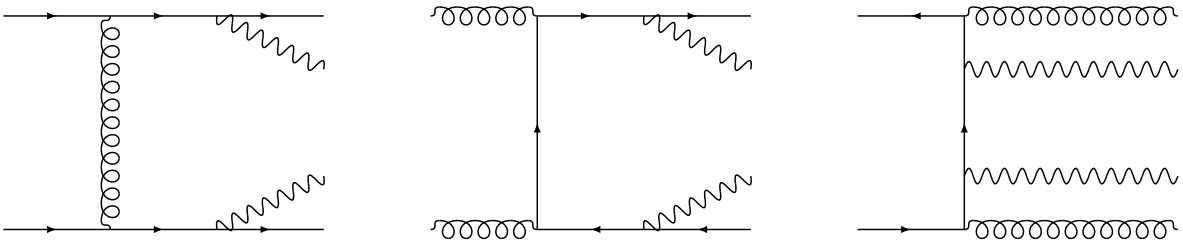

Figure 1.10: Representative $\mathcal{O}(\alpha^4\alpha_s^2)$ diagrams contributing to the $VVjj$-QCD production.

However, the contamination from the $VVjj$-QCD background is not showing equivalent impact for all processes. In the case of ss$WWjj$, the contribution from these QCD diagrams

is fairly low in the phase-space used in Table 1.2, with the ss$WWjj$-QCD cross-section about an order of magnitude lower than that of the ss$WWjj$-EW production.On the other hand, the $ZZjj$-QCD production cross section is expected to be about as large as the $ZZjj$-EW cross section, and the $WZjj$-QCD about twice as common as the $WZjj$-EW production in that same phase space.

Although the $VVjj$-EW and $VVjj$-QCD processes produce the same final state, certain differences of these processes can allow to separate them. Among these, as briefly discussed already, the most important one is the differing kinematics of the tagging jets system. Additionally, a distinctive feature of the $VVjj$-EW production is the absence of a color flow between the two final state quarks, that consequently suppresses the potential hadronic activity between the two tagging jets. The presence of such jets in an event would therefore tend to indicate that it is not produced through these $VVjj$-EW processes.

In addition to the $\mathcal{O}(\alpha^4\alpha_s^2)$ contribution to the $VVjj$ processes, one also has to consider the $\mathcal{O}(\alpha^5\alpha_s)$ interference terms that arise from the matrix element squaring,. The contribution from such terms is generally smaller than the $VVjj$-EW and $VVjj$-QCD contribution, but can be non-negligible.

1.4.2 Signal modelling

The main Monte Carlo generator used for both the $WZjj$-EW and $WZjj$-QCD processes modelling is Sherpa 2.2.2 [50], that handles all the steps of event generation, from the actual hard-scattering process, to the parton-shower and underlying event modelling. However, the event generation for the two processes is done independently. The $WZjj$-EW events are generated at LO, and include the contribution from all $\mathcal{O}(\alpha^6)$ diagrams with two jets initiated by the two matrix elements partons, three charged leptons and a neutrino. b-quark are not considered in the matrix element computation, in order not-to include $tZ + j$ events in the signal definition. $WZjj$-QCD events are generated from $\mathcal{O}(\alpha^4\alpha_s^2)$ diagrams. Events with up to one jet from the matrix element are generated at NLO, and up to three jets at LO, and do include diagrams involving b-quarks. The $\mathcal{O}(\alpha^5\alpha_s)$ interference between the two processes is also generated independently at LO using MadGraph5_aMC@NLO 2.3 [51]. These interferences are not used as a direct contributing process to the analysis selection, but instead to define an uncertainty on the signal shape in the measurement. The interference normalisation effect is found to represent about +10 % of the $WZjj$-EW event fraction, and is absorbed in its measurement. The impact on the shape is evaluated and considered as discussed in Section 5.2.4. All these processes generation use the same NNPDF3.0 PDF set, introduced in

Section 1.3.

A variety of Monte Carlo generators exist for the modelling of $VVjj$ events, and tend to give different predictions both for the cross sections and for the processes kinematics. Thorough comparisons between the most common ones for VBS studies have been performed in the scope of the ss$WWjj$-EW analysis [52], and some of the representative differences that were found are illustrated in Figure 1.11. The left figure compares the m_{jj} distribution shape predicted with SHERPA2.2.2, POWHEG [53], interfaced with PYTHIA8, and MADGRAPH+HERWIG7. Very different behaviour can be observed between the predictions. The figure on the right shows the distribution of the centrality of an eventual third jet, defined as

$$z_{j3} = \frac{y_{j3} - \frac{1}{2}(y_{j1} - y_{j2})}{|y_{j1} - y_{j2}|}, \tag{1.20}$$

where y is the particle rapidity, as defined in Section 2.3.1, and also showing non-negligible disagreement between the three generator predictions.

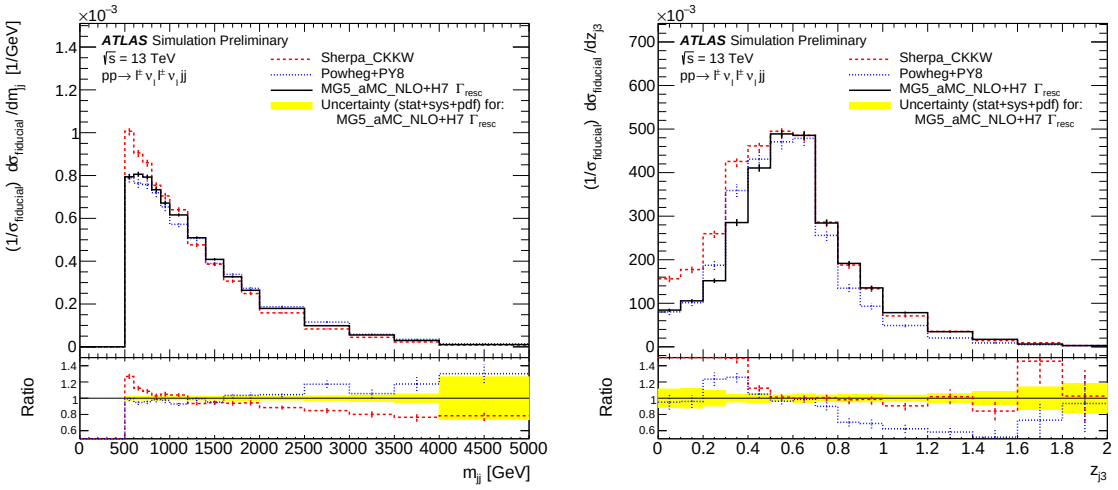

Figure 1.11: Normalized differential distributions for $pp \to \mu^+\nu_\mu e^+\nu_e jj$ process for m_{jj} and the third jet centrality z_{j3}, generated using SHERPA (dashed red), POWHEG+PYTHIA8 (dotted blue) and MADGRAPH+HERWIG7 (plain black). The ratios are computed with respect to the prediction from MADGRAPH+HERWIG7.[52]

These modelling discrepancies between generators are not specific to the ss$WWjj$ process. They are in large part coming from the description of the jet kinematics in $VVjj$ processes, and a special care has to be taken not to bias the measurements by relying too much on a potentially mismodelled prediction. In order to consider their impact in the $WZjj$-EW analysis, additional

Monte carlo samples are generated for both the $WZjj$-EW and $WZjj$-QCD production. The alternative $WZjj$-EW sample is generated at LO with MadGraph5_aMC@NLO 2.3. The same generator is used for the alternative $WZjj$-QCD sample, with up to two jets at LO, and the signal sample from the inclusive WZ analysis, generated with Powheg-Box v2 [53] is also used for validation, with the parton shower and hadronisation simulated with either Pythia8 or Herwig7. These generated samples all use the same NNPDF3.0 PDF set, introduced in Section 1.3.

1.4.3 NLO corrections

The computation complexity of NLO correction depends heavily on the number of initial and final state particles. In the case of a $2 \to 2$ process, with two initial state and two final state particles, corrections can be computed up to very high orders in perturbation theory. However, the $VVjj$ processes are $2 \to 6$ processes, rendering their higher-order correction computation highly non-trivial. Nevertheless, huge progress has been made in the past few years, and NLO corrections, both EW and QCD, are slowly becoming available for these processes [54, 55].

Including both the NLO-QCD and NLO-EW corrections to the $VVjj$ final state adds the higher order contributions presented in Figure 1.12. With these added terms, the purely-

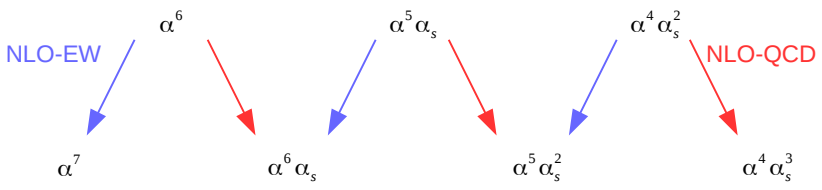

Figure 1.12: Correction orders, in terms of α and α_s for both the NLO-EW, and NLO-QCD corrections to the $VVjj$ processes involving two heavy gauge bosons $W^{\pm}$ or Z^0.

electroweak $VVjj$ production becomes ill-defined, and the NLO-corrected $VVjj$-EW predictions comparison to measurements is not trivial. In a comparison of measurement to LO prediction, one could, for instance, define the signal as containing only the purely electroweak diagrams, assuming a small impact from interferences. However, by adding the NLO correction, the purely-electroweak $VVjj$ production only exist in the NLO-EW terms, that cannot

be considered alone, and the NLO-QCD corrections, at $\mathcal{O}(\alpha^6\alpha_s)$ cannot be disentangled from the same-order terms arising from the NLO-EW corrections to the LO $\mathcal{O}(\alpha^5\alpha_s)$ interference. Following a similar logic, the separation between NLO-corrected interference and $VVjj$-QCD is also ill defined, and a study of the inclusive $VVjj$ production is required.

The effect from NLO QCD+EW corrections compared to LO predictions is similar in all the $VVjj$ processes that have been studied. It globally consists in a decrease of the cross-section of roughly 20 % for a typical VBS phase-space, and a non-negligible distortion of both the leptonic and hadronic final state particles kinematics. This is illustrated in Figure 1.13, showing the effect of the corrections for the $WZjj$ production with respect to the dijet invariant mass $M_{j_1j_2}$, and the transverse mass of the WZ system M_{T,W^+Z}. The effect of NLO-QCD corrections is dominant at low mass of the dijet system, but becomes negligible compared to the NLO-EW corrections for the higher mass regimes, in which the $VVjj$-EW contribution is expected to be larger. Concerning the WZ invariant mass, no large impact is seen from the NLO-QCD correction at high $m_{T,WZ}$, and the NLO-EW corrections are still very large, but mostly flat. Although these NLO corrections are now available, they were not all at the time

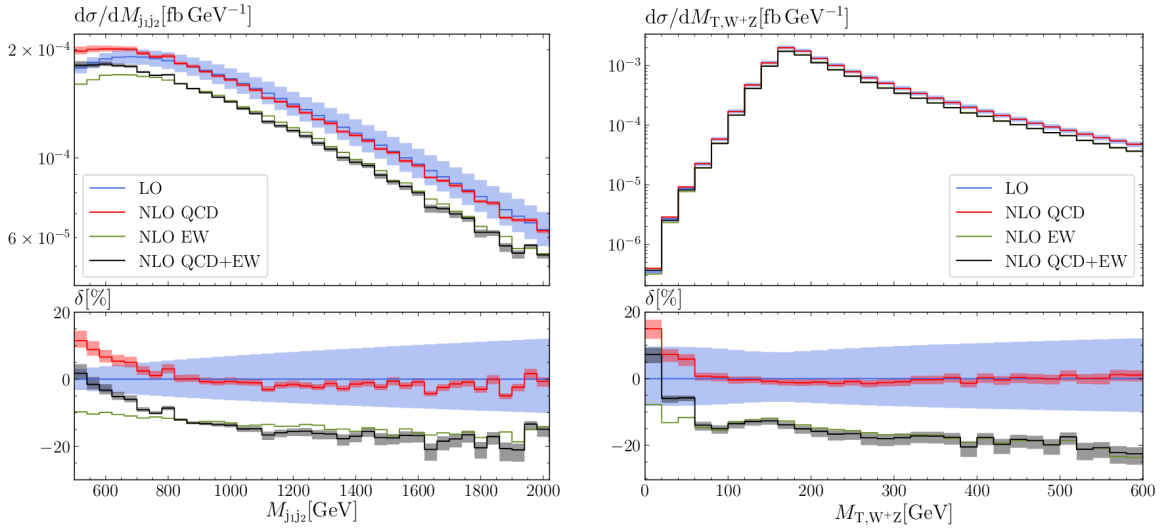

Figure 1.13: Differential distributions for $pp \to \mu^+\mu^-e^+\nu_e jj + X$ at the LHC with CM energy 13 TeV: (left) invariant mass of the two tagging jets, and (right) transverse mass of the four-leptons system. The upper panel shows the LO contribution of order $\mathcal{O}(\alpha^6)$, the two NLO predictions [including $\mathcal{O}(\alpha^7)$ (NLO EW) and $\mathcal{O}(\alpha_s\alpha^6)$ (NLO QCD)] as well as their sum. The lower panel shows the relative NLO corrections with respect to the LO in percent.[55]

at which the results presented in Chapter 5.3, but their impact should still be kept in mind, and it should be considered in future studies.

1.4.4 Experimental status of VBS searches

The first attempts to study experimentally VBS processes were performed with the pp collision data from the LHC Run 1, at a center-of-mass energy $\sqrt{s} = 8$ TeV. From these data, the ss$WWjj$-EW and $Z\gamma jj$-EW productions were studied by both the ATLAS [4, 56] and CMS experiment [3, 57]. In addition, ATLAS published a first study on the leptonic $WZjj$-EW production [58], as well as on the semi-leptonic $WVjj$-EW production [59], where a W-boson decays leptonically and the additional W- or Z-boson decays into a $q\bar{q}$ pair, and CMS a search for the $W\gamma jj$-EW production [60]. Due to the relatively low available statistics, none of these studies lead to an observation of the processes. Nevertheless, some very interesting results have been provided, with, most notably, all of the studies reporting limits on so-called anomalous quartic gauge couplings [61], under the form of constraints on the parameters of an extended SM Lagrangian, in the frame of effective field theory. These limits are typically extracted by looking for data-to-simulation discrepancies in the vector bosons kinematic distributions, as exemplified in Figure 1.14 for the $WZjj$-EW study. In this example, limits are set on the α_4 and α_5 of the added terms to the SM Lagrangian contributing to the quartic coupling, for the chosen parametrisation [62]. These limits are however largely statistically dominated, and yield very wide confidence intervals for the parameters values, motivating further the need to repeat such measurements with increased statistics.

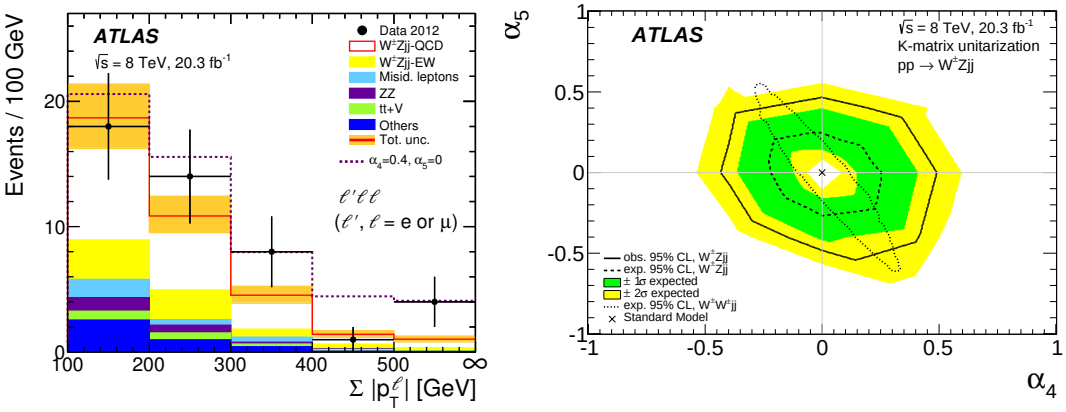

Figure 1.14: Left: Distribution of the scalar sum of the three final state lepton transverse momenta $\sum |p_T^\ell|$ for the $WZjj$-EW event selection used for the related Run 1 VBS study. The open red histogram shows the SM prediction, while the dashed purple line illustrate the impact of the added aQGC parameter $\alpha_4 = 0.4$. Right: Expected and observed 95 % C.L. contours on the two aQGC parameters α_4 and α_5 extracted from the measurement. The corresponding constraints from the ATLAS Run 1 same-sign $WWjj$-EW study [4] are shown for comparison.[58]

The Run 2 of the LHC raising the center of mass energy to $\sqrt{s} = 13$ TeV, and coming with increased data collection rate, allowed for the first observations of these processes. The first reported observation was made with the ss$WWjj$-EW analysis by CMS [6], based on the partial Run 2 dataset collected in 2015 and 2016, and reporting a 5.5 σ significance. This observation was later confirmed by the ATLAS experiment [63] also based on data from 2015-2016, with a 6.5 σ significance. These observations being the first to be made was expected, due to the process having both the highest production cross-section from all the VBS-related electroweak processes for a comparable phase space, as well as the lower overall contamination from the $VVjj$-QCD background, making it the "most promising candidate for discovery" [54].

The observation of the $WZjj$-EW production with 2015 and 2016 data [7], that is discussed in this thesis, was reported at a similar time to that of the ss$WWjj$-EW observation from ATLAS. Also at a similar time, the CMS collaboration published their result on the $WZjj$-EW production [64], where no observation is reported. These two results are found to achieve very different sensitivities, and a more detailed comparison is made in Section 5.3.2. The $WZjj$-EW production observation was finally reported by the CMS experiment with their study based on the Full Run 2 dataset [65], and a combined measurement of the $WZjj$-EW and ss$WWjj$-EW production cross-section, in which the $WZjj$-EW production mode is measured with a 6.8 σ significance.

Several additional studies have been performed since then. One can especially note the reported observation of two additional $VVjj$-EW production channels: the $Z\gamma jj$-EW and $ZZjj$-EW. Both have been studied with the partial Run 2 datasets from ATLAS and CMS. For the the $Z\gamma jj$-EW process, ATLAS and CMS reported strong evidence of the process with a 4.1 σ [66] and 3.9 σ [67] significance respectively. Concerning the $ZZjj$-EW production, CMS provided its first result with the partial Run 2 dataset [68]. Although this study did not lead to an observation of the process, it introduced for the first time the use of a multivariate discriminant for the separation of the electroweak signal and $VVjj$-QCD background in a VBS analysis, and proved the efficiency of this approach, that is slowly becoming the standard for such studies. The observation of this process was reported by the ATLAS collaboration based on the full Run 2 dataset, with a 5.5 σ significance [69], and more recently CMS reported a 4.0 σ evidence for it [70].

Chapter 2

The Large Hadron Collider and the ATLAS detector

This chapter describes the experimental setup used to record the data analysed in this thesis work. It is broken down in two parts: the accelerator complex and the particle detector. The accelerator complex in our case is mostly known for its main component, the Large Hadron Collider (LHC). The LHC is a circular accelerator and collider, located at CERN, on the French-Swiss border. Its 26.7 km circumference makes it the largest particle accelerator in the world. It has been providing proton-proton collisions at very high center-of-mass energy. The provided center-of-mass energy was limited to 8 TeV for the first data-taking run (Run 1), between 2010 and 2013. It was then pushed to 13 TeV for the second data-taking period (Run 2), between 2015 and 2018, and discussions are ongoing about reaching the design energy of 14 TeV for the upcoming Run 3. It hosts four large-scale experiments: the two largest, ATLAS (A Toroïdal Lhc ApparatuS) and CMS (Compact Muon Solenoid), are multi-purpose particle detectors designed to cover the largest spectrum of physics processes the LHC can potentially create. The two other experiments are ALICE (A Large Ion Collider Experiment), mostly focused on heavy ion physics, and LHCb (Large Hadron Collider beauty), that primarily aims at studying flavor physics. The work in this thesis uses data collected with the ATLAS detector, which will be described in more details in the following sections. Beforehand, in the first section, the accelerator complex will be described as well as how the LHC provides the proton collisions. In a second section, some more details about these particle collisions will be given.

2.1 The LHC acceleration complex

Before colliding in the center of the detectors mentioned above, protons have to go through a succession of linear and circular accelerators in order to achieve the required energy. The complete acceleration complex is shown schematically in Figure 2.1.

The proton acceleration process starts with hydrogen atoms that are extracted from a

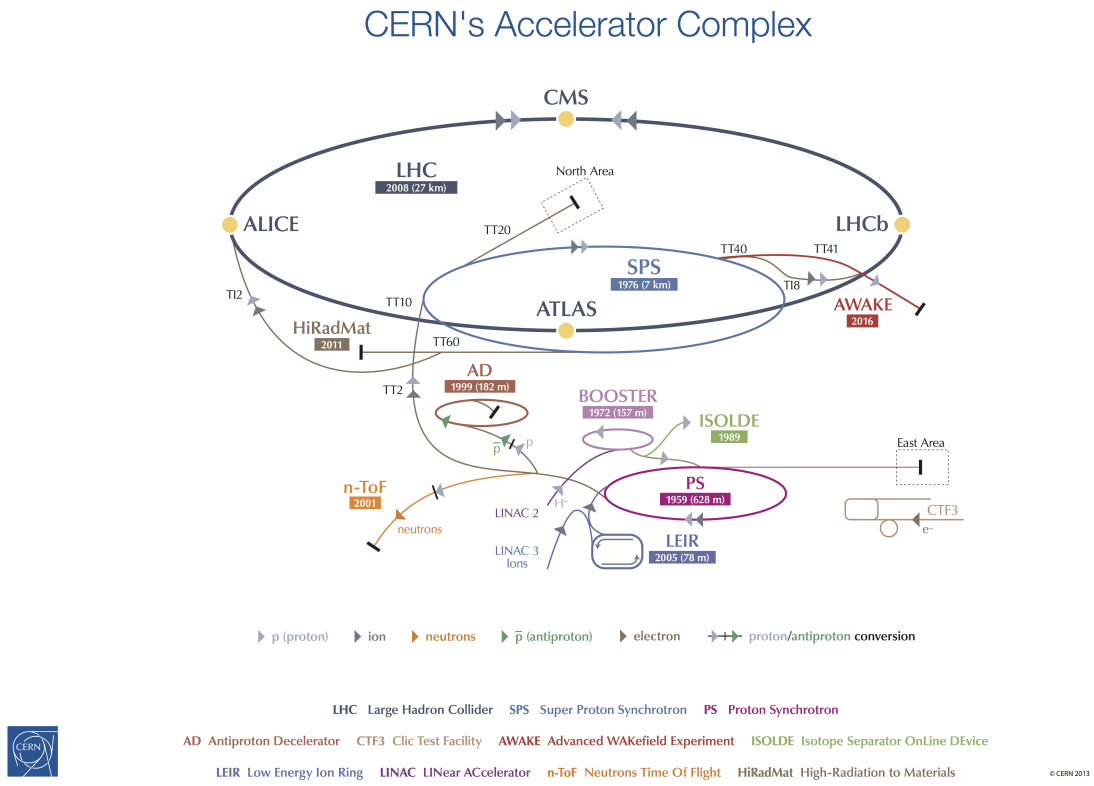

Figure 2.1: Schematic view of the LHC accelerator complex.[71]

simple hydrogen bottle. The hydrogen atoms are ionised by passing through an electric field before being directed to the first accelerator, the LINAC 2 (LINear ACcelerator 2), accelerating the protons to 50 MeV. Protons then pass through a first circular accelerator, the BOOSTER, that makes them reach the energy of 1.4 GeV. A second, the PS (Proton Synchrotron), then a third, the SPS (Super Proton Synchrotron), circular accelerators respectively allow the protons to reach the energy of 25 GeV, then 450 GeV. This is the energy at which protons are injected into the LHC, where they are split into two beams going in opposite directions, and then reach their 6.5 TeV collision energy thanks to radio-frequency cavitiesplaced along the beams path in a long straight segment of the accelerator. A series of superconducting dipoles, producing the 8 T magnetic field is used to keep the protons on the desired path, in addition to quadrupole magnets, which are used to properly collimate the beams. During a typical fill, the LHC is full with approximately a few thousands proton bunches, each containing 10^{11} protons, with 25 ns spacing between each other. This allows, once their collision energy is reached, to provide 13 TeV collisions for the various detectors, at a 40 MHz rate. Each of these fills lasts for a few hours, until the proton density gets below a certain threshold. At this point, the beams are dumped, and the injection process starts again for the following fill. The first collisions at the LHC took place in 2009, with center-of-mass energy of 900 MeV [72]. Data-taking runs continued in 2010 and 2011, with 7 TeV collision, and with 8 TeV collisions in 2012, collectively referred to as Run 1. A long shutdown (LS1) followed, and the operation started again in 2015 for Run 2 this time with $\sqrt{s} = 13$ TeV, and ended in 2018. This is the data-taking period on which the results presented in this thesis are based.

2.2 Particle collisions and luminosity

The quantity of collisions provided by the LHC is usually measured, and referred to, in terms of *luminosity*. The instantaneous luminosity L is related to the proton-proton interaction rate R, with $R = \frac{dN_{pp\to X}}{dt}$, for a given proton-proton inelastic interaction process with cross-section $\sigma_{pp\to X}$ by

$$R = L \times \sigma_{pp\to X}. \tag{2.1}$$

L can be expressed in terms of the beam parameters, as:

$$L = \frac{N_b^2 n_b f_{rev} \gamma}{4\pi\varepsilon_n \beta^*} F. \tag{2.2}$$

The terms N_b and n_b respectively represent the number of protons per bunch and the

number of bunches in a fill; f_{rev} is the revolution frequency of the LHC, of about 11kHz; ε_n is the transverse emittance that, together with the β^* parameter, account for the transverse width of the beam at the interaction point, and F is a correction factor, referred to as the geometric luminosity reduction factor, to account for the crossing angle between the two beams. The LHC was designed to provide an instantaneous luminosity of $L = 10^{34}$ cm^{-2}s^{-1}, and has been running often above its design performance as it can be seen in Figure 2.2.

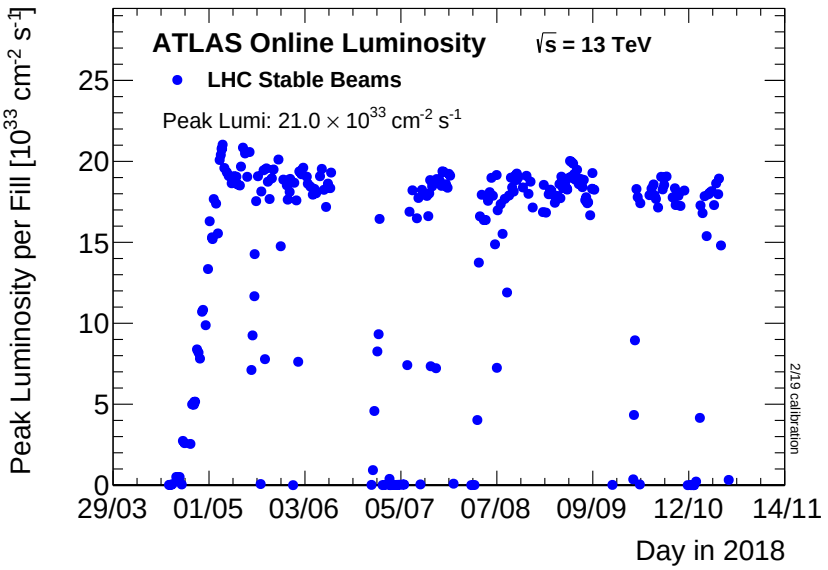

Figure 2.2: Peak instantaneous luminosity registered by ATLAS in 2018, at the start of LHC fills with stable beams.[73]

During the course of Run 2, this translates to an integrated luminosity L of 156 fb^{-1} delivered, allowing for $L = 139$ fb^{-1} of data usable for physics, after data-quality assessment, to be recorded by the ATLAS experiment, as shown by Figure 2.3.

Due to these very large collision frequency and beam density required to achieve such a luminosity, several collision typically occur for a single bunch crossing. This is commonly referred to as *pileup*. The average number of simultaneous interactions per bunch crossing for Run 2 is $\langle\mu\rangle = 33.7$, with a peak average of $\langle\mu\rangle = 37.8$ in 2017 as seen in Figure 2.4. On top of the usual *in-time* pileup, defined as the collision events occurring during the same bunch-crossing as the event of interest, one also has to consider *out-of-time* pileup, coming from remnants of informations found in some of the detector subsystems that end-up being attributed to the wrong bunch-crossing, and therefore to the wrong event typically from previous collisions.

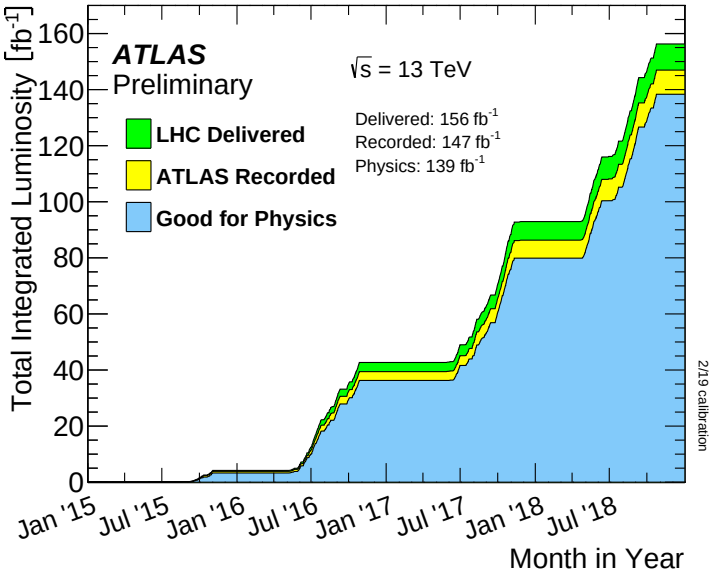

Figure 2.3: Cumulated integrated luminosity delivered by the LHC and recorded by ATLAS during Run 2.[73]

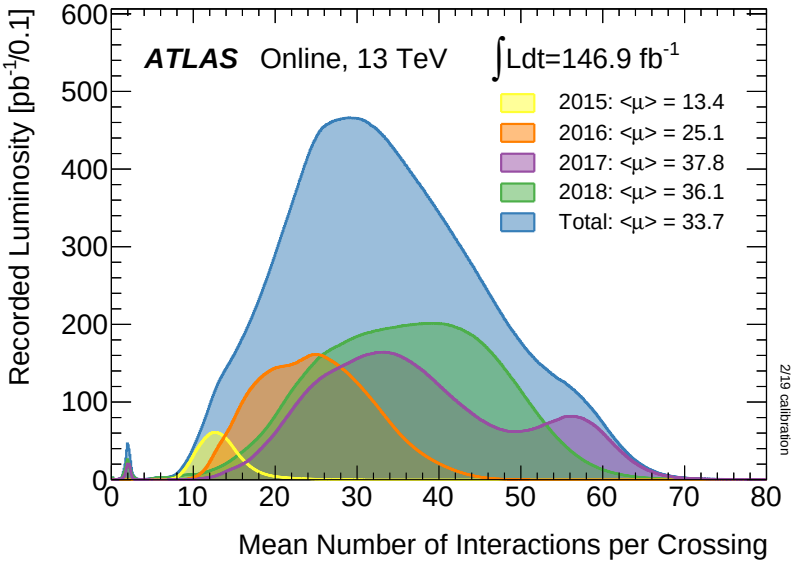

Figure 2.4: Mean number of interaction per bunch crossing in *pp* events recorded by the ATLAS experiment during Run 2.[73]

2.3 A Toroidal LHC ApparatuS

The ATLAS detector is the largest of the four large-scale experiments at the LHC, with a total diameter of 25 m and a 44 m length. It is a general purpose detector, with close to 4π solid

angle coverage. It has a layered structure with four specialised subsystems built on top of one another, and all centered around the interaction point with a complete cylindrical symmetry around the beam axis. These subsystems are shown in Figure 2.5.

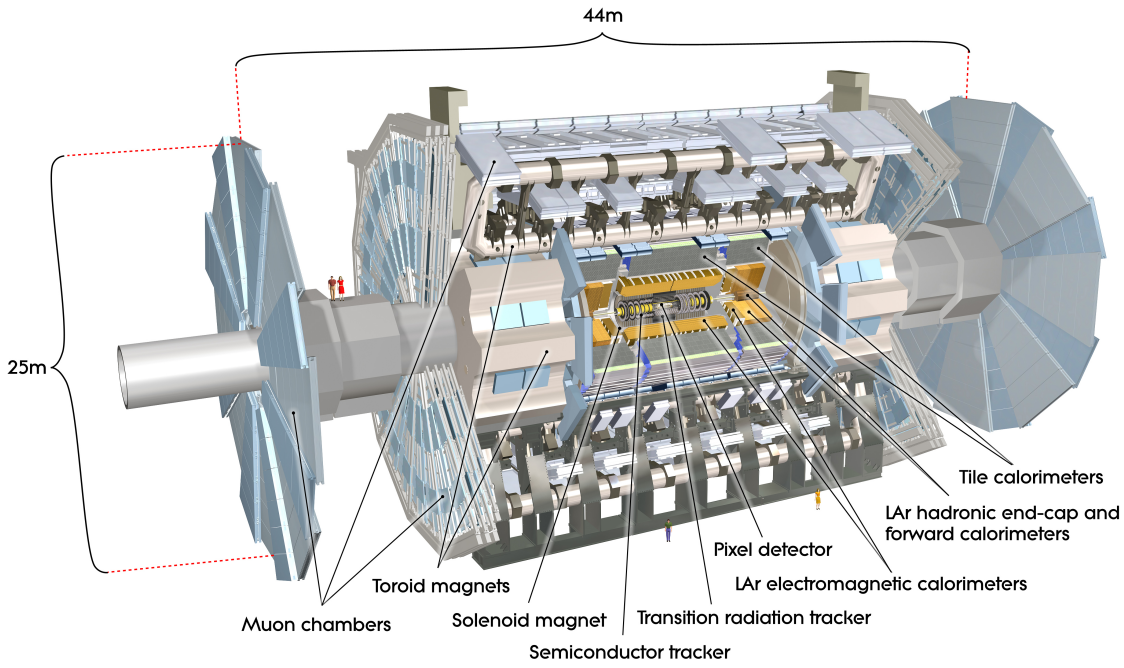

Figure 2.5: Schematic cut-away view of the ATLAS detector and its subsystems.[74]

The closest subsystem to the interaction point, referred to as the Inner Detector (ID), is described in section 2.3.2. It allows for the reconstruction and identification of charged particles tracks thanks to its fine granularity and with the help of the 2 T magnetic field provided by the solenoid surrounding it, that bends the charged particles trajectories. It is surrounded by the Electromagnetic Calorimeter (EMCal), described in section 2.3.3, in its turn enclosed in the Hadronic Calorimeter, described in section 2.3.4, in which most particles end their course and deposit their remaining energy. The fourth detection subsystem is the Muon Spectrometer (MS), described in section 2.3.5, that was specifically designed to measure muon's tracks and momentum, here again with the help of three powerful toroidal magnets surrounding it and bending muons tracks.

2.3.1 Coordinate system

The ATLAS coordinate system is centered at the nominal interaction point. The z-axis follows the beams direction. The x-axis is pointed towards the center of the LHC ring, and the y-axis is pointed upward. The two detector sides, referred to as side A and side C are used to define the z-axis sign. Detector's side A is defined to have positive z, and side C negative z. These choices allow for easy characterisation of the detector symmetries. ATLAS displays both a forward-backward symmetry with respect to the transverse plane, as well as an approximate rotational symmetry around the z-axis. For physics purposes, coordinates are usually expressed in terms of the the azimuthal angle ϕ, with respect to the z-axis, and the rapidity y as a replacement of the usual polar angle θ, and defined as

$$y = \frac{1}{2}\ln\left(\frac{E + p_z}{E - p_z}\right), \tag{2.3}$$

where E is the energy of the measured object, and p_z its momentum along z. The motivation for using y as an angular variable is that the rapidity difference Δy between two objects is a Lorentz-invariant for boosts along the beam axis. By assuming massless objects, the pseudo-rapidity η can be derived from y, and can be expressed as

$$\eta = \frac{1}{2}\ln\left(\frac{|p| + p_z}{|p| - p_z}\right) = -\frac{1}{2}\ln\tan\frac{\theta}{2}. \tag{2.4}$$

Although the pseudorapidity is technically not as accurately representing massive particles as the rapidity, and loses the invariance of the rapidity difference, it has the advantage of being very easily expressed with respect to the polar angle θ, and is in most cases the preferred variable used to express physics results. It is the variable that is typically used, among other things, to define the angular separation between two objects, written as

$$\Delta R = \sqrt{(\Delta\eta)^2 + (\Delta\phi)^2}. \tag{2.5}$$

2.3.2 The Inner Detector

The Inner Detector (ID) aims at providing precise tracking information for charged particles, and consequently allows for precise track-to-vertex association capability, thanks to pattern recognition algorithm able to efficiently reconstruct the tracks, after which their origin can be extrapolated back to the interaction point. This allows vertex identification for both primary vertices, from the pp interactions, and secondary vertices coming from decays of long-lived particles, such as b-hadrons or τ-leptons. The ID layout is illustrated in Figure 2.6.

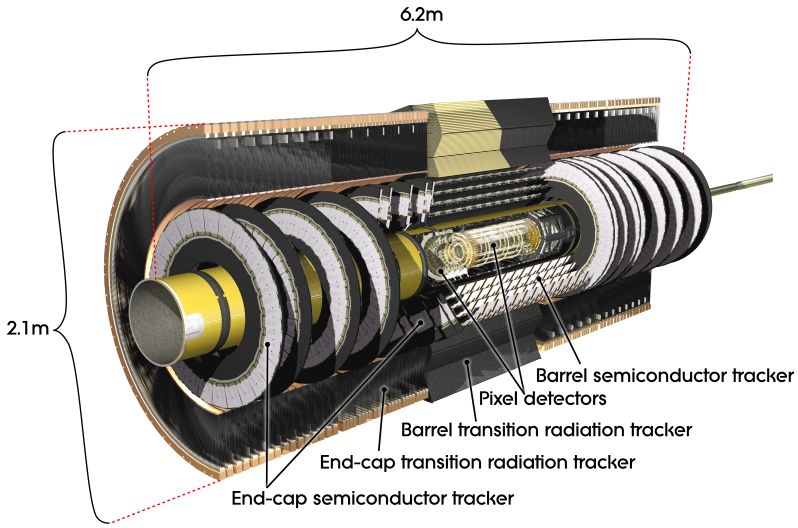

Figure 2.6: Schematic cut-away view of the ATLAS inner detector.

The ID is 6.2 m long and has a 1.08 m radius. It covers the pseudorapidity range $|\eta|<2.5$, and allows the measurement of tracks of down to $p_{\mathrm{T}} = 0.1$ GeV, with a $\frac{\sigma p_{\mathrm{T}}}{p_{\mathrm{T}}} = 5 \times 10^{-5}\ p_{\mathrm{T}}/\mathrm{GeV} \oplus 0.01$ resolution. With the generally large number of pileup interaction, the ID must ideally be able to resolve each individual vertex in order to identify the vertex of interest, often referred to as the hard-scatter (HS) vertex, which is usually defined as the one with the highest $\sum p_{\mathrm{T}}^{\mathrm{tracks}}$. The design resolution for the transverse (d_0) and longitudinal (z_0) impact parameters, are respectively $\sigma(d_0) = 11 \times (1 \oplus \frac{5.5}{p_{\mathrm{T}}/\mathrm{GeV}\sqrt{\sin\theta}})$ μm, and $\sigma(z_0) = 70 \times (1 \oplus \frac{1.4}{p_{\mathrm{T}}/\mathrm{GeV}\sqrt{\sin^3\theta}})$ μm. It is composed of three distinct subsystems operating independently. These are, going from the closest to the IP to the furthest away, the Pixel Detector, the SemiConductor tracker (SCT), and the Transition radiation tracker (TRT). These are directly surrounded by a superconducting solenoid, that provides a 2 T magnetic field, allowing for the measurement of the track momentum thanks to the added information of the track's bending radius, and of its charge, depending on the bending direction.

The Pixel Detector is composed of four silicon pixel layers wrapped around the z-axis in the barrel, spanning from 3.3 cm to 15 cm with respect to the beam, and 3 disk layers in both end-caps, yielding a total of about 80.4 million n^+/n silicon sensors, each covering a 400 $\times$ 50 μm surface, making the Pixel Detector the highest-granularity subsystem in ATLAS, which is required as its closeness to the IP makes it the detector part having to deal with the highest particle density. The three outermost layers, already installed for Run 1, allow the track reconstruction algorithm to reach an accuracy of 115 μm along the z direction, and up to

10 μm in the $R-\phi$ plane. The innermost layer, the Insertable B-layer (IBL) [75], was added before the start of Run 2. Notably thanks to its finer resolution of 8 μm in the $R-\phi$ plane and 40 μm in the z-direction, the IBL was found to improve the tracking capability, as well as the vertex reconstruction, especially concerning the secondary vertices used for b-jet identification.

The SCT surrounds the Pixel detector, in the range $R = 30 - 56$ cm. It is also structured similarly, with also 4 detection layers in the barrel, but 9 disks in both end-caps. Instead of silicon pixels, it uses a total of 6.3 millions 80 μm $\times$ 16 cm single-sided p/n silicon strips as a detecting medium. Each barrel layer is composed of two individual layers with a small 40 mrad angle between them to allow for a stereo-pairing, improving the resolution along z. This layout leads to a coarser resolution of 16 μm in the $R-\phi$ plane and 580 μm along z, which is adequate for the relatively lower particle density in its detection range.

The TRT is the final component of the ID. It is composed of about 350 thousands individual tubes. 72 layers of 144 cm long tubes, with a 4 mm diameter are laid parallel to the beam axis in the barrel, and 160 layers of smaller 36 cm-long tubes in the end-caps, oriented radially, helping to complete ATLAS tracking capability in the range $|\eta| < 2.0$. These tubes are filled with a Xe-CO_2-O_2 gas mixture acting as an interacting medium. A 31 μm-thick gold-coated tungsten wire is found at the center of each tube, acting as an anode, with the tube walls serving as a cathode. A 1.5 kV potential difference is applied between the anodes and cathodes, yielding a 2.5×10^4 gain that allows the detection of the very faint signals left by particles interacting with the gas mixture. These layers of straws are separated by radiating polypropylene tubes, creating transition-radiation photons from interacting electrons, which are of great importance for the identification of electrons and the separation between electrons and pions.

2.3.3 The Electromagnetic Calorimeter

The complete calorimetry system of ATLAS is shown in Figure 2.7.

It is split into two main subsystems: the Electromagnetic Calorimeter (EMCal), and the Hadronic Calorimeter (HCal).

The EMCal is the innermost of the two subsystems. Its main goal is the identification and energy measurement of electrons and photons. It can provide its energy measurement with a measured resolution of $\frac{\sigma_E}{E} = \frac{10\%}{\sqrt{E[\text{GeV}]}} \oplus 0.7\%$. It is a sampling calorimeter composed of an alternance of dense accordion-shaped steel-coated lead plates and thinner copper-coated kapton electrodes, that are immersed in liquid Argon (LAr) acting as an active material. The accordion geometry offers the advantages of a full azimuthal coverage, pairing well with the fine granularity of the system, while LAr was chosen for its radiation hardness property and relative cheapness, but relies on cryostats to be held in its liquid state, at 89 K. Electrons and photons

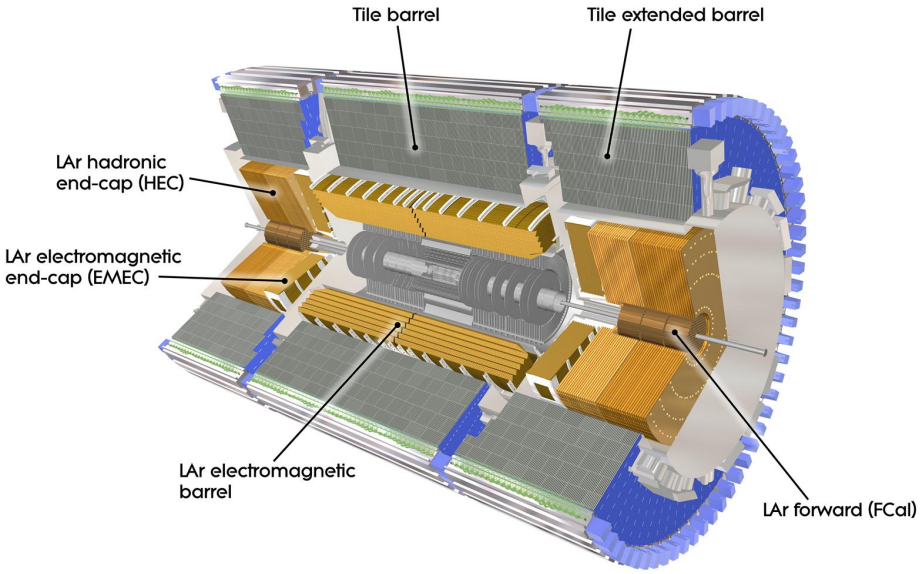

Figure 2.7: Schematic cut-away view of the ATLAS calorimeters.[74]

passing through the lead plates start a showering process through cascading bremstrahlung and e^+e^- pair production respectively, leaving most of their energy in the calorimeter, ionizing the LAr and liberating electrons that are then captured by the closest electrodes. A presampling layer is found before the cryostat and the first sampling layer of the EMCal, and is used to correct for energy lost in the calorimeter's dead material. It covers the pseudorapidity range $|\eta| < 1.8$. The EMCal is split into two identical half-barrels covering $|\eta| < 1.475$, and two end-caps covering $1.375 < |\eta| < 2.5$. All these parts are segmented further into 3 layers, with varying granularities. The innermost sampling layer, or strip sampling layer, is composed of $\Delta\eta \times \Delta\phi = 0.003 \times 0.1$ strips. This very fine granularity in η is useful for the distinction between pions (π^0 and $\pi^\pm$) and electromagnetic particles (γ and $e^\pm$) inside calorimeter showers. The middle sampling layer is composed of $\Delta\eta \times \Delta\phi = 0.025 \times 0.025$ cells, while the back layer has a coarser η granularity, with $\Delta\eta \times \Delta\phi = 0.05 \times 0.025$ cells.

The total depth of the barrel's EMCal varies with $|\eta|$, ranging from about 22 X_0 at $|\eta| = 0$ to about 33 X_0 at $|\eta| = 1.375$, where the radiation length, X_0, is the medium-dependent distance after which an electron loses 63% of its energy through bremstrahlung, allowing for close to complete containment of the electron and photon showers, and therefore accurate energy measurement. The end-cap components of the EMCal are both divided into two wheels centered on the z axis. The outer wheel covers the range $1.375 < |\eta| < 2.5$, and is split

into three sampling layers. The inner wheel covers $2.5 < |\eta| < 3.2$ and is split in only two layers. These sampling layers are all split in cells with η-dependent granularities as referenced in Table 2.1.

Table 2.1: Granularities of the various sampling layers of the EM calorimeter.

	Barrel ($\|\eta\| < 1.475$)	End-caps ($1.375 < \|\eta\| < 3.2$)	
	Granularity	Granularity	$\|\eta\|$ coverage
Presampler	0.025×0.1	0.025×0.1	$\|\eta\| < 1.8$
Strip sampling	0.003×0.1	0.025×0.1	$1.375 < \|\eta\| < 1.5$
		0.003×0.1	$1.5 < \|\eta\| < 1.8$
		0.004×0.1	$1.8 < \|\eta\| < 2.0$
		0.006×0.1	$2.0 < \|\eta\| < 2.5$
		0.1×0.1	$2.5 < \|\eta\| < 3.2$
Middle sampling	0.025×0.025	0.025×0.025	$1.375 < \|\eta\| < 2.5$
		0.1×0.1	$2.5 < \|\eta\| < 3.2$
Back sampling	0.025×0.025	0.025×0.025	$1.375 < \|\eta\| < 2.5$

2.3.4 The Hadronic Calorimeter

As indicated by its name, the HCal mainly aims at measuring the energy of hadronic particles. The general HCal layout is shown schematically in Figure 2.7. It is composed of different types of calorimetry systems. The barrel part, the Tile Calorimeter (TileCal), covers the range $|\eta| < 1.0$. It is completed on both sides by an extended barrel, covering $0.8 < |\eta| < 1.7$. Each of its modules is composed of three radial sampling layers, each of them made of $\Delta\eta \times \Delta\phi = 0.1 \times 0.1$ cells ($\Delta\eta \times \Delta\phi = 0.2 \times 0.1$ for the last layer), made of plastic scintillators and steel absorbers, and positioned perpendicular to the beam axis. The association of Tile and EM LAr calorimeter information allows to reach an energy resolution of $\frac{\sigma_E}{E} = \frac{53\%}{\sqrt{E[\text{GeV}]}} \oplus 3\%$ for isolated charged pions energy measurement. The Hadronic End-Caps (HEC) then cover the range $1.5 < |\eta| < 3.2$. These are another pair of LAr-based sampling calorimeters, placed in the continuity of the EMEC. They are composed of a succession of regularly-spaced copper plates, with 8.5 mm LAr-filled gaps in-between them. These are separated into two distinct layers with different width for the copper plates. The closest layer to the EMEC on each side is composed of 25-mm-thick copper plates, and the second layer's plates are 50 mm thick. The EMEC reaches a resolution of $\frac{\sigma_E}{E} = \frac{71\%}{\sqrt{E[\text{GeV}]}} \oplus 1.5\%$ The ATLAS calorimetry is finally completed in the very forward region ($3.1 < |\eta| < 4.9$) by the LAR-based Forward Calorimeters (FCal). It is composed of three modules, the first one using copper as absorbing medium, and acts as a forward complement to the EMCal. It is followed by two tungsten-based modules completing the HCal angular coverage, with an energy resolution of $\frac{\sigma_E}{E} = \frac{94\%}{\sqrt{E[\text{GeV}]}} \oplus 7.5\%$.

2.3.5 The Muon Spectrometer

The final, and outermost, detection subsystem of ATLAS is the Muon Spectrometer (MS). It is designed specifically to measure muons momentum, up to $|\eta| = 2.7$, as well as for fast triggering for muons up to $|\eta| = 2.4$. The MS, with the help of the large superconducting air-cored toroid magnets bending muons trajectories, allows for the detection and measurement of muons down to 5 GeV with an energy resolution of 3 % at 100 GeV.

The layout of the MS is shown in Figure 2.8. In the barrel region, the toroid is composed of eight coils placed radially and regularly spaced around the beam axis. The magnetic field created by these coils covers the range $|\eta| < 1.4$. In each end-cap, an additional smaller toroid covers the range $1.6 < |\eta| < 2.7$.

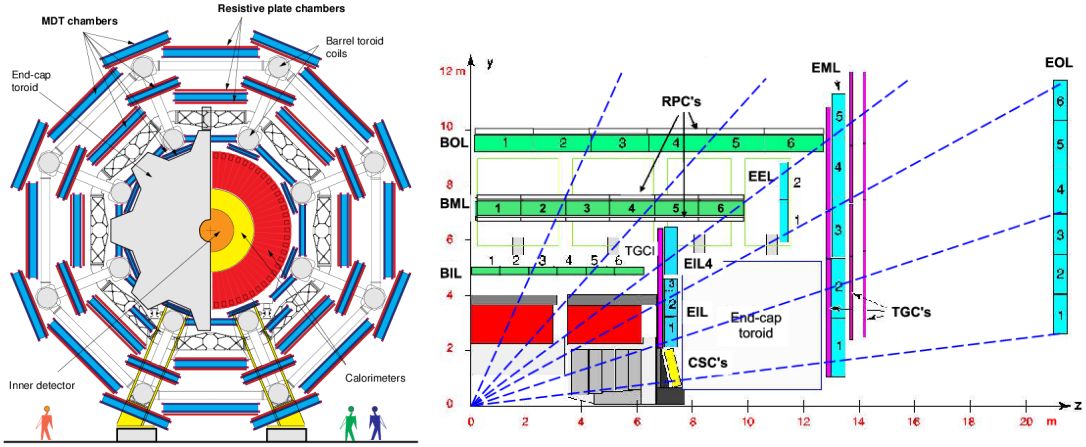

Figure 2.8: Schematic transverse cut (left), and longitudinal cut of a quadrant (right) of the ATLAS Muon Spectrometer.[74]

The MS is composed of four different sorts of detector technologies, all based on ionising current measurement in drift chambers. These are the Monitored Drift Tube chambers (MDTs) and Cathode-Strip Chambers (CSCs) for precision tracking, and the Resistive Plate Chambers (RPCs) and Thin Gap Chambers (TGCs) for trigger.

The MDTs are aluminum tubes filled with a mixture of Ar and CO_2 gas at a 3 bar pressure. Each tube contains a tungsten-rhenium wire operating at a 3 kV voltage acting as an anode. Each of the MDTs chamber is composed of two sections of three layers of these tubes in the barrel inner layer (BIL), and four of them in the middle (BML) and outer (BOL) layers. The MDTs are designed for precise tracking of muons and cover most of the MS pseudorapidity total coverage, with a single-hit resolution of about 35 μm per chamber.

For the larger pseudorapidities, in the range $2.0 < |\eta| < 2.7$, CSCs replace the MDTs in the innermost layer. The CSCs are multi-wire proportional chambers, also filled with a mixture of Ar and CO_2 gas, with strip-segmented cathodes orthogonal to the beam axis. The CSCs have better time resolution and rate capability than the MDTs, justifying their use in these more forward regions, only partially covered by the ID for tracking, and in which the particle flux is higher. The CSC chambers have a slightly lower resolution than the MDTs, with 40 μm in the tracks bending plane, and 5 mm in the transverse plane.

For trigger purpose, the RPCs are placed in the barrel, covering the range $|\eta| < 1.05$, while the end-caps are equiped with the TGCs up to $|\eta| = 2.4$. The RPCs are arranged into three concentric layers around the beam axis. Two of these layers are placed right before and after the MDT middle layer, and the third one right after the MDT outer layer. Each layer is composed of two parallel electrode plates, with a 2 mm gap between them filled with a $C_2H_2F_4$ gas mixture. A 9.8 kV potential difference is required between the two plates in order to reach the detector's excellent 2 ns time resolution.

The TGCs are multi-wire proportional chambers filled with a CO_2/n-C_5H_{12} mixture. A 1.4 mm distance separates each of the strip cathode from the wires, while wires are each spaced by 1.8 mm, allowing for a good time resolution of about 4 ns. They are arranged in four layers. The innermost layer is placed in front of the end-cap inner layer of the MDT. The second layer is placed in front of the second MDT wheel, while the two last layers are placed right behind it.

2.3.6 The Trigger system

The LHC provides a bunch crossing rate of 40 MHz. At such a rate, it is not possible to fully reconstruct every single event. The ATLAS trigger system was design to handle this problem, allowing to reduce the input rate to a manageable one, without sacrificing interesting data for physics analyses. This is done thanks to two separated trigger systems. The first one (L1) is a hardware-based trigger that uses measurements from the calorimeters and MS. The second system, the High-Level Trigger (HLT), is software-based. The L1 trigger alone reduces the input rate to 100 kHz, while the HLT pushed the reduction down to 1 kHz. L1 is optimised for fast decision making. It aims at identifying high-energy particles by combining calorimetric information with tracking information from the MS. Energy deposits in the EMCal are interpreted by L1 as electrons or photons. In the HCal, a sliding-window algorithm is used to trigger on potential jet candidates reconstructed from coarse calorimeter towers of fixed $\Delta\eta \times \Delta\phi = 0.2 \times 0.2$ size, for which the total transverse energy E_{T} is above a fixed threshold value. Muons are triggered based on coincident hits in the different layers of the RPC or TGC.

The HLT can be split in two, as the level 2 trigger (L2) and the event filter (EF). L2 uses similar measurements as L1, but with a finer granularity, and with the complement of ID information up to $|\eta| < 2.4$, while the EF uses offline information on the event, about both tracking and jet reconstruction. Both L1 and HLT triggers have a variety of conditions checked to know whether or not to keep an event. These are usually related to the type and energy of particles in the event, which are aimed at by physics analysis. Some special triggers conditions are also implemented for specific analyses or calibration studies. Among them, the so-called zerobias trigger condition for the work presented in Chapter 4.1. This trigger randomly selects event, without requirement on the actual kinematics, and is used among other thing to study the properties of pileup interactions. For the leptonic WZ production studies presented in Section 5.1.1, the trigger requirements used are all based on specific p_T thresholds for electrons and muons, with added requirements on the leptons isolation. They are detailed in Section 3.

Chapter 3

Particle reconstruction

The information provided by the ATLAS detector for each *pp* collision comes under the form of energy deposits registered by the detection sub-systems. In order to interpret this raw output in terms of the event particle content and kinematical properties, advanced particle reconstruction procedures have to be employed. These are described in this Chapter. Section 3.1 explains the reconstruction process for electrons and photons. Muon reconstruction is then described in Section 3.2, followed by the reconstruction of hadronic jets in Section 3.3, and finally that of the neutrinos from the missing transverse energy in Section 3.4.

3.1 Reconstruction of Electrons

Both electrons and photons can be reconstructed within $|\eta| < 2.47$, excluding the $1.37 < |\eta| < 1.52$ barrel-to-end-cap transition region, thanks to their energy deposits in the EMCal. On top of that, as electrons are charged particles, their reconstruction process highly benefits from tracking information from the ID. Figure 3.1 shows the typical trajectory of an electron coming from a *pp* collision. The electron reconstruction process starts with the interpretation of EMCal information. Electrons and photons passing through the EMCal dense medium start a showering process through cascading bremstrahlung and e^+e^- pair production respectively, leaving most of their energy in the calorimeter, ionizing the LAr and liberating electrons that are then captured by the closest electrodes. These wide particle showers are split between many of the calorimeter layers and cells. Each of these cells will provide a distinct electrical signal directly proportional to the shower's energy deposited in it. For reconstruction purpose, these cells are swept using a sliding-window algorithm, in order to identify 3×5 cells fixed-size clusters. The $\Delta\eta \times \Delta\phi = 0.025 \times 0.025$ cell size used in the algorithm is chosen to match the middle sampling layer granularity. These clusters contain all cells from three sampling layers that are inside the window. The algorithm tries to determine the window maximising the measured energy, and if this energy is above a 2.5 GeV threshold, the corresponding cluster is marked as a seed cluster.

Clusters are then matched with ID tracks. The tracks used for the matching are constructed

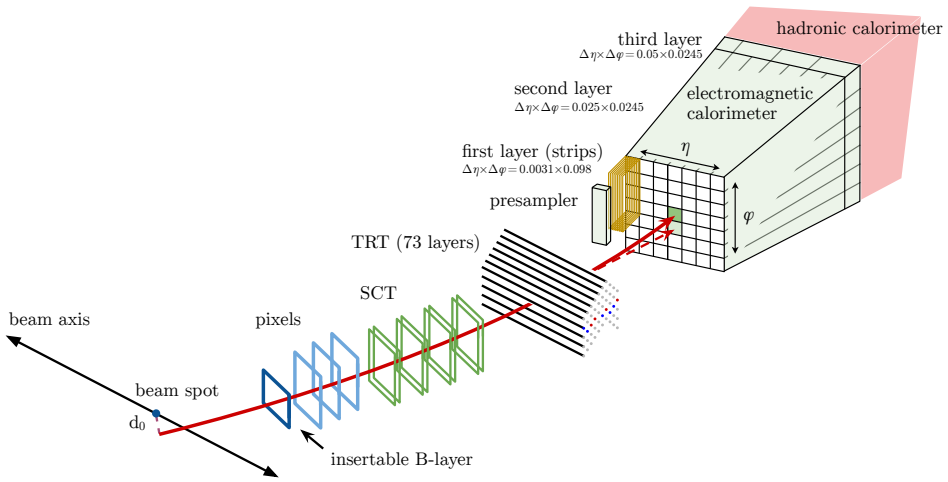

Figure 3.1: Schematic view of a typical electron path through the ATLAS detector subsystems.[76]

from hits in the various layers of the ID. A total of 12 hits, shared between the IBL, pixel and silicon strip layers, typically constitute the electron track candidates.If a cluster can't be matched to any tracks, it is identified as an unconverted photon. In case the reconstructed seed cluster can be matched with at least one track from the ID coming from the hard-scatter vertex, it can be tagged in two ways. The vertex of origin of the track is identified. In case this vertex is the HS vertex, then the cluster is tagged as an electron cluster. If several tracks can be matched to the cluster, a single one is kept, based on the number of silicon hits, and on its closeness in ΔR to the cluster. If the track cannot be matched to the HS vertex, the cluster is tagged as a converted photon. Photon conversion can be a large background source for electron-targetting analysis. In order to reduce its impact, the tracks are required to satisfy $|d_0/\sigma_{d_0}| < 5$ and $|z_0 \sin(\theta)| < 0.5$ mm, to strengthen the reliability of the association to the HS vertex, where d_0 (z_0) is the transverse (longitudinal) impact parameter, defined as the distance between the track and the beam line in the transverse (longitudinal) plane, and θ is the track's polar angle.

This process allows for a very high cluster reconstruction efficiency, as shown in Figure 3.2. Reconstructed electrons are then passed through some identification requirements, with varying strictness (tightness) for different use-cases, in order to further differenciate signal electrons (prompt) from other charged particles with similar signature, like pions or converted photons. A representative identification criteria is the likelihood-based (LH) identification, as other identification methods rely on subsets of the variables used to define the LH discriminant. The variable built here is based on a likelihood combination of quantities related to the recon-

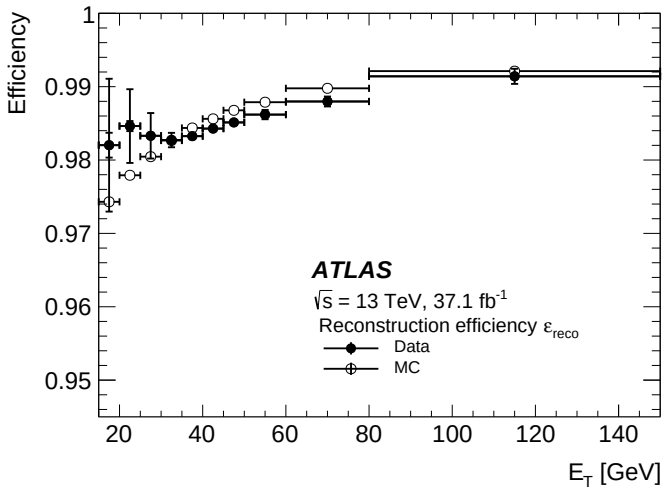

Figure 3.2: Efficiency of the electron reconstruction procedure for simulated $Z \to ee$ events (empty dots), and actual data events (full dots).[76]

struction quality. The complete list of variables used to build the LH discriminant is given in [76]. These include, among other things, variables related to the cluster isolation, built as energy ratios of differently-sized clusters in either the η or ϕ direction, broader energy measurements comparing the cluster energy to the total measured energy in the LAr calorimeter for a given event, ID hit quality variables, d_0 and d_0/σ_{d_0}, and variables related to the track-cluster matching quality, such as the E/p ratio between the cluster energy and corresponding track momentum. Three working points are defined as cuts on the LH discriminant. These are typically referred to as *LooseLH*, *MediumLH*, and *TightLH* working points. These are defined to match electron identification efficiencies going from 95% for the LooseLH working point, down to 80% for the TightLH working point. The loss in electron identification efficiency that comes with the use of a tighter working point is compensated by an improved background rejection, which is typically desired for analyses where non-prompt electron backgrounds are important.

A final quality-requirement step is applied to the electrons regarding their isolation, in order to suppress the background even further. These are requirement on the track isolation, $p_{\mathrm{T}}^{\mathrm{varcone0.2}}$, defined as the sum of transverse momenta of tracks within a $\Delta R = \min(0.2, 10\ \mathrm{GeV}/E_{\mathrm{T}})$ around the electron track, and on the cluster isolation, $E_{\mathrm{T}}^{\mathrm{cone0.2}}$, defined as the summed energy of all clusters within $\Delta R < 0.2$ of the electron cluster. These two variables are also used to define three working points: *Loose*, *Tight* and *Gradient*. The first two correspond to fixed-efficiency cuts on the two variables, while the *Gradient* working point corresponds to a p_{T}-dependent cut with varying efficiency, from 90% at $p_{\mathrm{T}} = 25$ GeV up to 99% at $p_{\mathrm{T}} = 60$ GeV.

3.2 Reconstruction of Muons

Muons are the only kind of particles that typically leave information in all the ATLAS detection layers (ID, calorimeters and MS), and can be reconstructed through the combination of information of these three systems, depending on their respective acceptance. Nevertheless, the calorimeter-related information is often limited, and tracking information, from either the MS alone, or both the ID and MS is used for their reconstruction.

ID tracks are reconstructed similarly to what is described in Section 3.1, and considered as muon track candidates. Independently, in each of the MS layers, information from muon chambers is combined in order to identify track segments through a linear fit, and are required to loosely point toward the IP in order to reduce non-collision backgrounds, such as cosmic muons, and random hit association. These segments are then associated between layers to form additional muon track candidates. This is done through a track-finding algorithm that attempts to match segments together into a single trajectory mainly based on angular information, and accounting for the track bending from the magnetic field. At least two compatible segments are typically required to reconstruct a muon track, except in the barrel-endcap transition region where a single one is required, with tightened quality constraints. It is a fairly common occurrence for a segment to be associated to several reconstructed tracks. This can be sign of a bad track, but it can also be due to close-by muons that can't be resolved in that specific layer. In order to remove bad tracks while not reducing the reconstruction efficiency by getting rid of overlapping good muons, an overlap removal algorithm is applied at a later stage, to either assign the segment to a single track, or when that seem more relevant, share its information between tracks. Once the muon track candidate is built, a χ^2 fit is performed, comparing the track to the hits associated to it. Only tracks satisfying a certain fit quality are kept. For these, the contribution of each hit to the fit is evaluated, and those yielding large contributions are removed, before repeating the fit. This gradually corrects the measured trajectory of the muon candidate, and can lead to additional hits getting close to it. When that is the case, these hits are incorporated in the algorithm, and treated as mentioned above.

At this stage, information from the different subsystems can be combined. Four different combination processes are used, corresponding to four muon types: Combined muons (CB), Segment-tagged muons (ST), Calorimeter-tagged muons (CT) and Extrapolated muons (ME). CB muons are reconstructed by combining the ID and MS muon track candidates through a global refit of the hits in both subsystems, adding or removing MS hits when needed to improve the fit quality. ST muons are also reconstructed using a combination of ID and MS muon track candidates, but this time only requiring the ID track to be associated to at least one of the

MS track segments, which is particularly useful in region of limited MS coverage such as the barrel-endcap transition, where information may be missing to reconstruct complete MS tracks. CT muons, combine ID and calorimeter information, requiring an ID muon track candidate to match an energy deposit in the calorimeter compatible with a minimum-ionizing particle. This is the reconstruction method yielding the lowest purity, but is useful in regions without MS coverage, such as the very central $|\eta| < 0.1$ region, for which the process is optimised. Finally, ME muons are solely based on MS information and on a loose IP-matching requirement, and are typically used in regions with MS coverage but without ID, in the range $2.5 < |\eta| < 2.7$. In case of overlap between different muon types, during the reconstruction, if a same ID track is shared between the two muons, priority is given following the type priority CB, then ST, then CT. For overlaps with ME muons, the track kept is chosen based on the fit quality and total number of hits.

Reconstructed muons then have to pass the identification process, mainly aiming at reducing background contributions arising primarily from pion and kaon decays. This process assesses the identification quality based on three variables. These include the q/p significance, which is the absolute difference of the charge-energy ratios as measured in the ID and MS, and divided by the quadratic sum of their respective uncertainties, and $\rho' = \frac{|p_{\mathrm{T}}^{\mathrm{ID}} - p_{\mathrm{T}}^{\mathrm{MS}}|}{p_{\mathrm{T}}^{\mathrm{track}}}$, assessing the compatibility between both the charge and the energy of the muon measured from the ID and MS, and the normalised χ^2 of the combined hits-to-track fit.

Similarly to what is done for electrons, three working points, *Loose, Medium* and *Tight*, are defined, corresponding to cuts on the identification variables with different efficiencies. The *Loose* working point selects all types of muons, only restricting the CT and ST muon selection to the $|\eta| < 0.1$ region. *Medium* muons are a subset of it, where only CB, and ME in the $2.5 < |\eta| < 2.7$ range, muon tracks are selected if they satisfy some loose requirements on two of the three identification variables mentioned above, excluding the normalized χ^2. *Tight* muons are the subset of *Medium* CB muons that, on top of the *Medium* selection criteria, present a normalized χ^2 value below a certain threshold. A tightened requirement on q/p and ρ' is required, under the form of a two dimensional p_{T}-dependent cut.

Additional isolation criteria can then be applied. These are also defined similarly to the electron isolation criteria, with a track-based variable, corresponding to the sum of the transverse momentum of all objects, and a calorimeter-based variable using transverse energy instead, in a cone around the muon In the present case, $p_{\mathrm{T}}^{\mathrm{varcone30}}$ and $E_{\mathrm{T}}^{\mathrm{topocone20}}$ are used, using cone radii of $\Delta R = \min(10\ \mathrm{GeV}/p_{\mathrm{T}}, 0.3)$ and $\Delta R = 0.2$ respectively.

The muon reconstruction, identification and isolation selections are very efficient at miti-

gating background contamination, while conserving a high signal efficiency. This can be seen in Figure 3.3, where the efficiency p_{T} dependence is shown for the *Medium* identification working point and an isolation working point referred to as *FixedCutLoose*, corresponding to $p_{\mathrm{T}}^{\mathrm{varcone30}}/p_{\mathrm{T}}^{\mu} < 0.15$ and $E_{\mathrm{T}}^{\mathrm{topocone20}}/p_{\mathrm{T}}^{\mu} < 0.3$, that are chosen here for illustrative purposes. A more complete overview of the global muon reconstruction process can be found in Ref. [77].

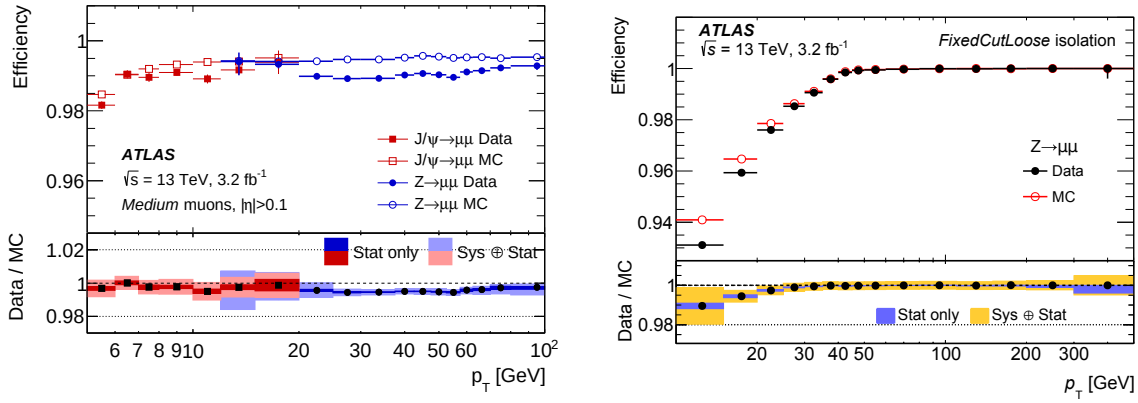

Figure 3.3: Muon identification (left) and isolation (right) efficiencies. The *Medium* identification working point, and *FixedCutLoose* isolation working points are used.[77]

3.3 Reconstruction of Jets

Jets are, by nature, composite objects. They are made of a large number of partons coming from the initial quark or gluon hadronisation, appearing in the detector as a collimated shower, composed of both charged particles, that leave energy deposits in the calorimeters and ID tracks, and neutral particles only interacting with the calorimeters.

Although many jet reconstruction algorithms exist, adapted for different use-cases, two approaches are of interest for the work presented here. A first approach is based exclusively on calorimetric information to build EM topological clusters, that are then used as base components to reconstruct the so-called EMTopo jets. The second approach uses both tracking and calorimetric information through a Particle Flow algorithm to build PFlow jets.

An important component of these approaches is their common clustering algorithm used to handle calorimetric information, referred to as the "4-2-0" algorithm, that acts as follows:

- Single calorimeter cells are identified as cluster seeds if their measured energy statisfies $|E_{\mathrm{cell}}| > 4\sigma_{\mathrm{noise}}$, where σ_{noise} is the expected noise standard deviation for that given cell.

- Direct neighbours of the cluster with $|E_{\text{cell}}| > 2\sigma_{\text{noise}}$ are added to it recursively until no more cells with such energy are found.
- All remaining non-clustered neighbouring cells from the same detection layer, or from adjacent layers overlapping in (η,ϕ) with the clustered cells, are added to the clusters, without any requirement on their energy
- If two or more local energy maxima exist in the resulting cluster, corresponding to a cell energy excess of at least 500 MeV with respect to its direct neighbours, the cluster is split in two with cells being associated to each maxima according to their relative ΔR distance to it.

These clusters are referred to as topological clusters. They are all attributed a 4-vector, measured at the electromagnetic energy scale (EM scale), tuned for a good reconstruction of electrons and photons, and are considered massless. For the purpose of building EMTopo jets, these EM-scale topoclusters are then directly combined using the Anti-k_T algorithm [78]. With this algorithm, the most energetic cluster is identified, and neighbouring clusters are recursively merged to it in descending transverse momentum order if they satisfy

$$\min\left(k_{T,i}^{-2}, k_{T,j}^{-2}\right)\frac{\Delta R_{ij}}{R^2} < k_{T,i}^{-2}, \tag{3.1}$$

where $k_{T,i,j}$ are the transverse momentum of cluster i and j respectively, with $k_{T,i} > k_{T,j}$, ΔR_{ij} is the relative distance between the clusters, and R is the jet radius, that is fixed to $R = 0.4$ for all the jets used in the various part of this thesis. This jet algorithm has the benefit over other jet algorithms of reconstructing circular jets, as seen in Figure 3.4, making their calibration easier, while still being colinear safe, meaning that it is independent of the particle multiplicity within the hadronic shower, and infrared-safe, or in other words, independent of the initial parton's soft radiations.

Alternatively, the PFlow algorithm combines the topoclusters to ID tracking information in order to reconstruct the jets prior to the application of the jet algorithm. This approach improves the energy resolution at low jet p_T and makes the jet reconstruction more pile-up robust.

As a first step, each single topocluster is matched, when possible, to the ID track yielding the smaller $\Delta R'$ value, defined as

$$\Delta R' = \sqrt{\left(\frac{\Delta\phi}{\sigma_\phi}\right)^2 + \left(\frac{\Delta\eta}{\sigma_\eta}\right)^2}, \tag{3.2}$$

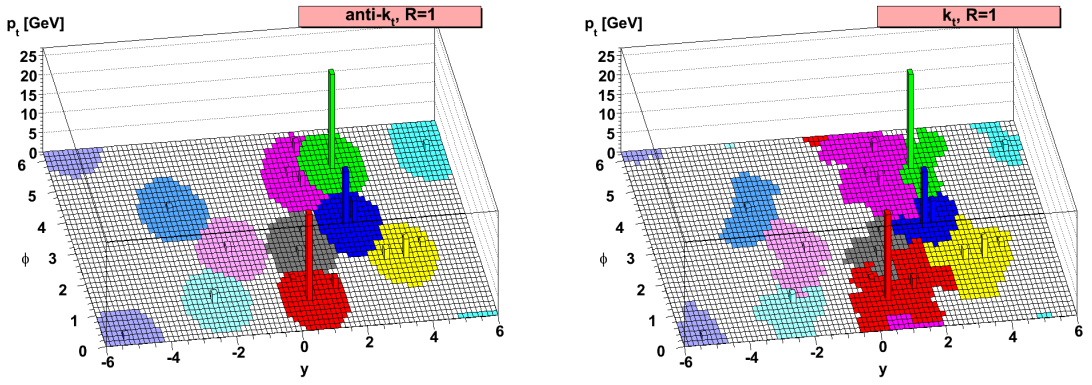

Figure 3.4: Anti-k_T jets (left) and k_T jets [79] (right) with a radius parameter R=1, for a same high jet multiplicity event. The k_T algorithm follows the same principle as the Anti-k_T, but with an ascending transverse momentum ordering.[80]

where $\Delta\phi$ and $\Delta\eta$ are the angular separations between the track and the topocluster barycenter, and σ_ϕ and σ_η represent the cluster's energy distribution gaussian width in the corresponding directions, around its barycenter. Clusters that can't be directly matched to any track are referred to as unmodified neutral clusters later on, and are expected to originate from neutral particles. For each pair of track and cluster, that ideally correspond to measurements coming from a single particle, the expected energy deposit in the calorimeter is evaluated based on both the track momentum and the cluster position, and conveniently expressed as an E/p ratio, where E and p respectively represent the cluster's energy and track's momentum. If the cluster's measured energy is too low to match this estimated value, it is likely that the track's energy is shared between several topoclusters. When that is the case, more clusters can be included in the matching.

Once the matching is done, the expected energy in the calorimeter is subtracted cell-by-cell from the topoclusters until all cells were covered, or all the energy has been subtracted. In case the remaining energy in the topoclusters is consistent with shower fluctuations of a single particle, this excess energy is removed, so that the full particle kinematics are now encoded in its corresponding track. If they are not consistent, a modified cluster with no tracks associated to it is then formed, and is assumed to have been initiated by another neutral particle. The set of tracks, unmodified neutral clusters and modified clusters resulting from this procedure is commonly referred to as Particle Flow Objects (PFO). PFOs whose track can be associated to any vertex that is not the primary vertex of interest, commonly referred to as PU vertices, are removed at this stage, and the remaining PFOs are finally associated into jets following the same Anti-k_T procedure as for EMTopo jets.

Both EMTopo and PFlow jets are then calibrated in a similar fashion. The first calibration step consists in a correction applied to account for pileup contamination. This correction factor is estimated as

$$p_{\mathrm{T}}^{\mathrm{corr}} = p_{\mathrm{T}}^{\mathrm{reco}} - \rho A - \alpha(N_{\mathrm{PV}} - 1) - \beta\mu, \tag{3.3}$$

where ρ is the median transverse energy density measured from topoclusters only in the case of EMTopo jets, and from both charged and neutral PFOs for PFlow jets, A is the jet area. The quantities N_{PV} and μ are respectively the number of reconstructed primary vertices in the event and the number of pp interactions in the event. It has been observed that the jet response evolves linearly with respect to these two variables. In this regard, the coefficients α and β represents the respective fitted slopes of these dependences.

The jet energy is then corrected to the Jet Energy Scale (JES) through a Monte Carlo based procedure, referred to as the MC numerical inversion. In this process, the response $\mathcal{R} = \frac{E_{\mathrm{reco}}}{E_{\mathrm{truth}}}$, where E_{reco} and E_{truth} are respectively the reconstructed and generated jet energy, is evaluated in simulation. The so-called truth-particle jets from which E_{truth} is evaluated are seeded from generator-level stable particles originating from the hard-scatter vertex, and are matched to the detector-level jet through a process called jet ghost association [81], if the energy of the truth-particle jet components associated to the detector-level jet represents more than 50 % of the truth-particle jet energy. The response $\mathcal{R}$ is then fitted in $(E_{\mathrm{truth}}, \eta)$ bins, in each of which a correction factor is extracted, expressed as the inverted mean of the fitted Gaussian function.

The next calibration step, referred to as the Global Sequential Correction, aims at correcting for effects due to intrinsic properties of the jets not properly taken into account, such as the initial parton's flavour, and the hadron composition yielded by the fragmentation process.

Another correction concerns the Jet Energy Resolution (JER), which can differ between data and Monte Carlo simulations, due, for instance, to some mismodelled detector effects, or to the relative contributions of HS and PU vertices information contribution to the event. The JER correction is evaluated by comparing the jet p_{T} to that of well-measured reference objects from Z+jets, γ+jets and dijet events.

Some of the uncertainties related to the various jet calibration steps mentioned above play a critical role in the sensitivity of the $WZjj$ analysis. The details specific to this analysis are given in section 5.2.4. Generally speaking, both JES and JER corrections heavily depend on the jet p_{T}, as illustrated by Figure 3.5. Lower p_{T} jets are typically much more sensitive to them. This is especially true for EMTopo jets, where the JES correction factors get larger than

for PFlow jets in these regimes. However, the opposite is seen for higher-p_{T} jets, above about 100 GeV, as the tracking resolution increases, therefore becomes worse, with the increasing p_{T}. For PFlow jets, while the same overall p_{T} dependence is observed, the uncertainties at low p_{T} are smaller, also due to the better momentum resolution of the ID compared to the calorimeters in this regime. In addition, although the JER-related are of the same order for EMTopo and PFlow jets, the better energy resolution at low p_{T} for the latter implies a reduction of the potential migrations that can be caused by cuts on the jets p_{T}, meaning that lower event-wide JER uncertainties can be expected with PFlow jets.

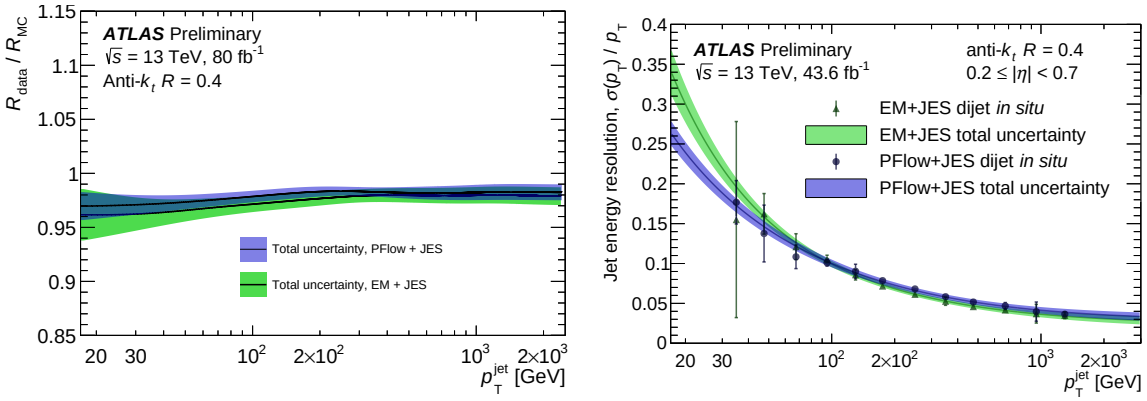

Figure 3.5: Jet p_{T} response ratio between data and Monte Carlo for JES calibration (left), and Jet energy resolution with respect to the jet p_{T} (right), compared between EMTopo and PFlow jets.[82]

3.4 Neutrinos and the Missing Transverse Energy

Some particles interact only extremely weakly with matter, making them hard to detect. For what concerns Standard Model particles, this is true for neutrinos. Although they cannot be observed directly as hadrons, electrons or muons, based on some energy trails left in the ATLAS subsystems, their presence can still be checked for, and their kinematics evaluated, at least partly, thanks to the momentum conservation principle. As it is not possible to know exactly what fraction of the initial pp interaction can be attributed to the initial-state partons in our collision data, the momentum conservation principle doesn't help much in the longitudinal direction. Nevertheless, the total transverse momentum is guaranteed to be zero. When neutrinos are produced, the measured total transverse momentum of the vectorial sum of all final-state particles can be imbalanced. This momentum imbalance is referred to as missing-E_{T} ($E_{\mathrm{T}}^{\mathrm{miss}}$).

In a more detailed form, it is computed as

$$E_{x(y)}^{\text{miss}} = E_{x,y}^{\text{miss},\gamma} + E_{x,y}^{\text{miss},e} + E_{x,y}^{\text{miss},\mu} + E_{x,y}^{\text{miss},\tau} + E_{x,y}^{\text{miss,jets}} + E_{x,y}^{\text{miss,soft}}, \tag{3.4}$$

where each term correspond to the signed x- or y-axis projection of the momentum sum of all hard final state objects, in addition to a term accounting for soft objects that accounts for tracks not associated to any physical particles, but still contributing to the total event momentum. It can then be easily expressed as

$$E_{\text{T}}^{\text{miss}} = \sqrt{(E_x^{\text{miss}})^2 + (E_y^{\text{miss}})^2}. \tag{3.5}$$

The choice of objects that enter the $E_{\text{T}}^{\text{miss}}$ computation relies on quality requirements, similar to those mentioned in Sections 3.1-3.3. The $E_{\text{T}}^{\text{miss}}$ resolution sensitivity especially comes from the jet term. More specifically, jets are the physical objects the most sensitive to pile-up contamination, especially for jets with $|\eta| > 2.5$, that have limited, if not zero, tracking information. In that regard, pileup-robust $E_{\text{T}}^{\text{miss}}$ calibrations are made available, which include different strictness-levels of cuts on the Pile-up jet taggers that are described in Chapter 4.1.

Chapter 4

Identification and suppression of pile-up jets

It is a fairly common occurence that jets originating from PU vertices survive the jet reconstruction and calibration steps described in Section 3.3. These PU jets can have a disastrous impact on physics analysis, by faking the actual jets of interest and therefore biasing the event selection. For the object reconstruction, it is of critical importance to remove pileup jets, in order to be able to properly estimate the E_T^{miss}. Pileup jets can be reconstructed for different objects, and for various reasons, that are briefly introduced in Section 4.1.

A variety of algorithms exist to identify and remove PU jets, and those commonly used in ATLAS are described in this section. Within the ID acceptance, the track-based *Jet-Vertex-Tagger* (JVT) algorithm is used. It is described in Section 4.2. In the forward region, where no tracking information is available, it is completed by the event-topology-based *forward Jet-Vertex-Tagger* (fJVT), that is described in Section 4.3.

The following sections describe personal contributions. The *Multivariate fJVT* (MVfJVT), an improved definition of the fJVT developed as part of this thesis work, is presented in Section 4.4.

The calibration process for the forward pileup taggers, the fJVT and MVfJVT, also performed as part of the preparation of this thesis, is then detailed in Section 4.5.

4.1 Pileup jets definitions

PU jets are typically categorized into two distinct categories. The first, and most frequent type of PU jet is referred to as QCD-PU. These jets are actual hadronic jets originating from a hard-scatter interaction from one of the event's primary vertices that is not the vertex from which the process of interest is arising. The second category is referred to as stochastic PU, and gather all the jet objects reconstructed from random bits of information registered in the detector, but not related to a common initial interaction. These bits of information can be either in-time or out-of-time, following the distinction explained in Section 2.2.

As jets are composite objects, reconstructed from close-by clusters of energy, any HS or PU jet can be partially constructed from energy deposits that do not actually come from the initial state hadron decay, making the categorization into HS, QCD-PU, and stochastic PU jets somewhat ambiguous. Nevertheless, such classification is necessary in order to study PU-jet suppression techniques, and their definition is set using the available generator-level information, also referred to as truth information in the following. Any jet that can be matched to a truth HS jet with $p_{\mathrm{T}} > 10$ GeV within a $\Delta R < 0.3$ cone is classified as a HS jet. The remaining jets are classified as PU jets if no truth hard-scatter jet with $p_{\mathrm{T}} > 4$ GeV is found within $\Delta R < 0.6$. This definition implies that some jets remain unclassified, but it improves the purity of the classification. Unclassified jets are not considered further. The PU jet category can be divided further into QCD-PU jets and stochastic PU jets, on condition that particle-level information is available for them, which is typically not the case for simulated data used in ATLAS physics analyses. The latter category can as well potentially include out-of-time QCD pileup jets in addition to the actual stochastic PU jets, as those do not typically have associated particle-level information. QCD-PU jets are defined as any jet matched with a truth PU jet with $p_{\mathrm{T}} > 10$ GeV within $\Delta R < 0.3$, and stochastic PU as jets with no such truth PU jet within $\Delta R < 0.6$.

4.2 The Jet-Vertex-Tagger algorithm

Within the ID acceptance, with $|\eta| < 2.5$, tracking information can be used to match a jet to the vertex it originates from. The general idea of this matching is to compare the jet energy measured in the calorimeters, to that of the tracks within the jet radius that can be associated to the vertex of interest. This type of information has been the main means of identification and discrimination of PU jets in ATLAS since Run 1 [83]. The Jet-Vertex Tagger (JVT) [84] has been developed in order to take the most advantage out of it.

The JVT discriminant is defined as a likelihood combination of the two track-based variables:

$$\mathrm{corrJVF} = \frac{\sum_k p_{\mathrm{T}}^{\mathrm{track}_k}(\mathrm{PV}_0)}{\sum_l p_{\mathrm{T}}^{\mathrm{track}_l}(\mathrm{PV}_0) + \frac{p_{\mathrm{T}}^{\mathrm{PU}}}{k.n_{\mathrm{tracks}}^{\mathrm{PU}}}}, \tag{4.1}$$

and

$$R_{p_{\mathrm{T}}} = \frac{\sum_k p_T^{\mathrm{track}_k}(\mathrm{PV}_0)}{p_{\mathrm{T}}^{jet}}. \tag{4.2}$$

The $\sum_k p_{\mathrm{T}}^{\mathrm{track}_k}(\mathrm{PV}_0)$ term, appearing in both formulas, represents the scalar sum of tracks

p_{T}, considering all tracks originating from the HS vertex. corrJVF also uses a similar term for PU vertices, $p_{\mathrm{T}}^{\mathrm{PU}} = \sum_{n\geq 1} \sum_{l} p_{\mathrm{T}}^{\mathrm{track}_l}(\mathrm{PV}_n)$, where PU vertices are noted as PV_n. The correction factor $\frac{1}{k.n_{\mathrm{tracks}}^{\mathrm{PU}}}$, with $k = 0.01$, is applied to account for the linear dependence of $p_{\mathrm{T}}^{\mathrm{PU}}$ on the primary vertex multiplicity $\mathrm{N_{PV}}$.

These two variables are, by themselves, excellent PU-jet discriminants, and allow for an even better separation of HS and PU jets when considered together, as illustrated in Figure 4.1. Their combination is performed using a k-nearest-neighbour algorithm, as implemented in

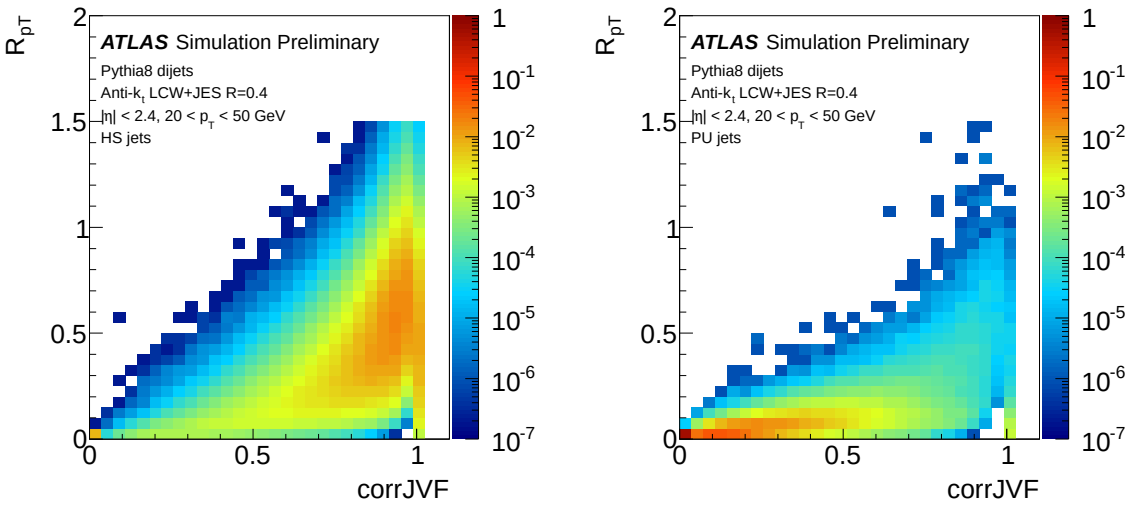

Figure 4.1: Comparison of two-dimensional distributions, normalised to unity, of corrJVF and $R_{p_{\mathrm{T}}}$ for truth-matched HS(left) and PU (right) EMTopo jets in simulated $\sqrt{s} = 8$ TeV dijet events.[84]

TMVA [85], with $k = 100$, resulting in the definition of an excellent discriminant, the JVT, shown in Figure 4.2, constructed so that jets with JVT values close to one are likely HS jets, while smaller JVT values indicating that the jet is likely a PU jet.

The JVT discriminant is built similarly for EMTopo and PFlow jets, although, its impact for PFlow jets is reduced, due to the built-in pileup jet suppression present in the PFlow reconstruction algorithm described in Section 3.3. For that reason, dedicated working points are defined differently for the two types of jets. For EMTopo jets, three working points are commonly used, *Loose*, *Medium* and *Tight*, corresponding to the cuts JVT > 0.11, JVT > 0.59 and JVT > 0.91, and defined to reach HS efficiencies of 97%, 92% and 85% respectively. For PFlow jets, only two working points are used, *Medium* and *Tight*, with the looser JVT > 0.2 and JVT > 0.5 cuts, still yielding high HS efficiencies of 97% and 96% respectively.

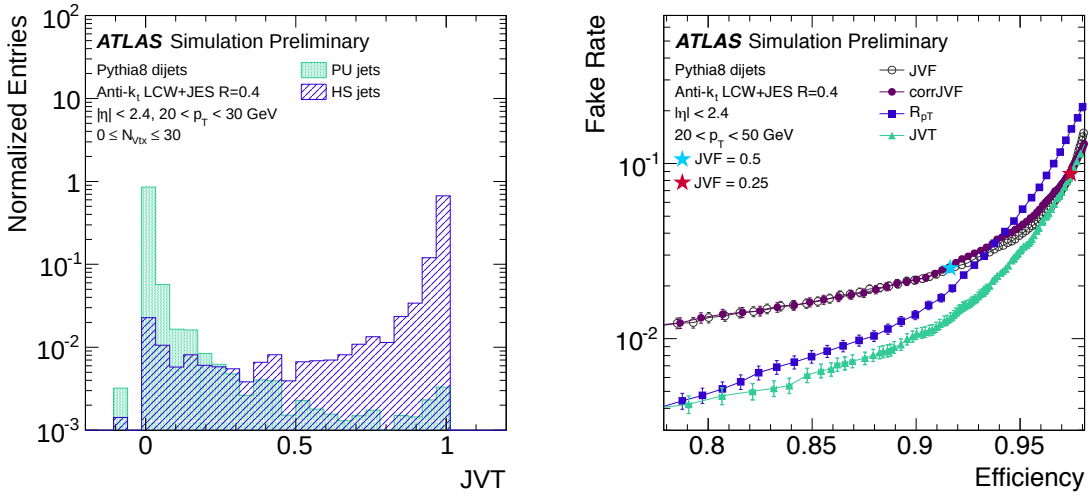

Figure 4.2: (left) Comparative distribution, scaled to unity, of JVT for truth-matched HS and PU EMTopo jets in simulated $\sqrt{s} = 8$ TeV dijet events. (Right) PU-jet fake rate as a function of the HS-jet efficiency for cuts on the JVT discriminant and JVT input variables. The performance is compared to that of the JVT inputs, corrJVF and $R_{p_{\mathrm{T}}}$, as well as that of the formerly-used PU-jet tagging variable, the JVF.[84]

4.3 The Forward Jet-Vertex-Tagger algorithm

For jets with $|\eta| > 2.5$, the JVT algorithm cannot be used due to the absence of tracking information. In order to still be able to suppress PU jets, the forward-JVT [86] (fJVT) is used instead. This algorithm attempts to match forward jets to vertices by looking at the complete event topology, and associates the information from centrally produced particles to that of the forward jets to better characterise it.

The fJVT discriminant is built in several steps, and with slight differences between EMTopo and PFlow jets. As a first step for EMTopo jets, the central PU jets are identified and matched to PU vertices. This identification is done by requiring jets with $|\eta| < 2.5$ that satisfy JVT < 0.11, to remove as much of the HS jets as possible, while keeping a large majority of the PU jets. In order to reduce the contribution from stochastic pileup jets, these jets are also required to be relatively energetic, with a minimum $p_{\mathrm{T}} < 35$ GeV threshold. In addition, a $R^i_{p_{\mathrm{T}}}$ value, is computed for each PU vertex i, similarly to Eq. 4.2. For each jet, the two vertices yielding the largest $R^i_{p_{\mathrm{T}}}$ values are identified, and the difference between these two values, $\Delta R_{p_{\mathrm{T}}}$, is required to satisfy $\Delta R_{p_{\mathrm{T}}} > 0.2$.

Jets passing this selection can then be associated to the vertex i in which the ratio between the vertex-associated tracks and jet energies $R^i_{p_{\mathrm{T}}}$, defined as in Section 4.2, is the largest.

The missing transverse momentum associated to each vertex i, excluding the HS vertex, is computed, as

$$-p_{\mathrm{T},i}^{\mathrm{miss}} = \frac{1}{2}\left(k \sum_{\mathrm{tracks}\in\mathrm{PV}_i} p_{\mathrm{T}}^{\mathrm{track}} + \sum_{\mathrm{jets}\in\mathrm{PV}_i} p_{\mathrm{T}}^{\mathrm{jet}}\right), \tag{4.3}$$

where the average of calorimeter jets, and tracks p_{T} is considered, with the factor $k = 2.5$ implemented to account for the contribution of neutral particles not leaving ID tracks, but contributing to the measured energy in the calorimeter.

The PFlow approach requires some additional preliminary steps, as jets associated to PU vertices are removed with the PFlow algorithm. As they are required for the fJVT computation, these central PU jets are retrieved by applying the PFlow reconstruction method, and the JES calibration steps described in Section 3.3 for each PU vertex. In a similar way as for EMTopo jets, QCD PU jets are identified through the application of slightly modified $p_{\mathrm{T}} > 20$ GeV, JVT < 0.2, and $R^{i}_{p_{\mathrm{T}}} > 0.1$ requirements, optimised for the full Run 2 conditions as presented in [87], and the PU vertices missing transverse momentum computation is optimised with respect to Eq. 4.3, in order to take advantage of the better energy resolution provided by the tracking systems at low p_{T}, and is evaluated as

$$-p_{\mathrm{T},i}^{\mathrm{miss}} = \left(\sum_{\text{jets, } p_{\mathrm{T}}^{\mathrm{jet}}>20 \text{ GeV}} p_{\mathrm{T}}^{\mathrm{jet}} + \sum_{\text{tracks, } p_{\mathrm{T}}^{\mathrm{jet}}<20 \text{ GeV}} p_{\mathrm{T}}^{\mathrm{track}} + \sum_{\text{tracks, } R_{p\mathrm{T}}^{\mathrm{jet}}<0.1} p_{T}^{\mathrm{track}}\right)_{\text{jets, tracks}\in\mathrm{PV}_i}. \tag{4.4}$$

The following steps are identical for EMTopo and PFlow jets, and is shown schematically in Figure 4.3.

The vertices $p_{\mathrm{T},i}^{\mathrm{miss}}$ is projected for each PU vertex i, onto the forward jet's p_{T}, to estimate an fJVT_i as

$$\mathrm{fJVT}_i = \frac{-p_{\mathrm{T},i}^{\mathrm{miss}}.p_{\mathrm{T}}^{\mathrm{jet}}}{p_{\mathrm{T}}^{\mathrm{jet}}.p_{\mathrm{T}}^{\mathrm{jet}}}. \tag{4.5}$$

The final fJVT discriminant can then be defined as $\mathrm{fJVT} = \max_i(\mathrm{fJVT}_i)$. High values of the discriminant indicate that the forward jet matches well one of the PU vertices, and is likely to be a QCD PU jet. A lower value tends to indicate that the jet is a HS jet, as it cannot be used to properly fill the missing information from any of the PU vertices.

It is important to note that the fJVT discriminant is only clearly defined for QCD pileup jets, as opposed to stochastic pileup jets. Stochastic pileup jets are, by definition, not associable

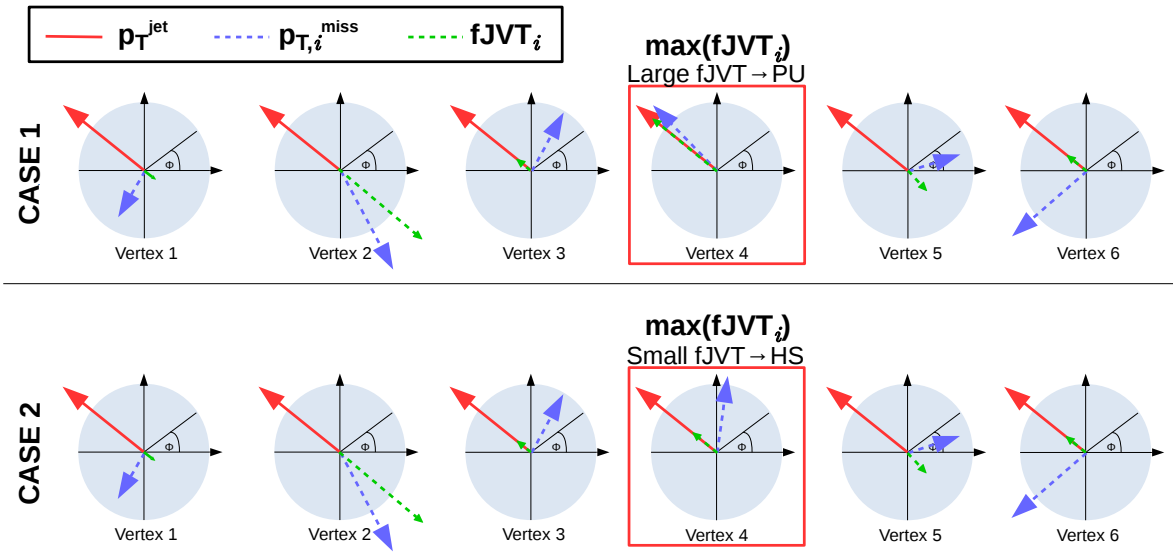

Figure 4.3: Schematic representation of the fJVT jet-tagging process, for a six-vertices event. Top row illustrates the case of a PU-like forward jet, while bottom row illustrates the HS-like forward jet case.

to a given vertex, and the fJVT definition does not hold meaningful information for those objects. As an effort to remove stochastic pileup jets, requirements applied at analysis level on the fJVT value, are accompanied with an additional requirement on the jet timing. This quantity is evaluated from calorimetric information. The cell peaking time, t_{cell} is defined with respect to the bunch crossing clock. By considering this quantity for all the cells in a cluster, the cluster timing, t_{clus} can be defined, as

$$t_{\text{clus}} = \frac{\sum E_{\text{cell}}^2 t_{\text{cell}}}{\sum E_{\text{cell}}^2}, \tag{4.6}$$

and the jet timing t, in a similar way, as

$$t = \frac{\sum E_{\text{clus}}^2 t_{\text{clus}}}{\sum E_{\text{clus}}^2}. \tag{4.7}$$

The fJVT and timing distributions are illustrated in Figure 4.4 for EMTopo jets. Similar distribution is seen for PFlow jets.

Two working points are defined for the fJVT, the loosest one corresponding to the requirement fJVT<0.5, and a slightly tighter one to fJVT<0.4. An additional, much tighter, working point is also considered in the study, corresponding to a fJVT<0.2 cut. All three working points have the same timing cut applied, with $|t| < 10$ ns.

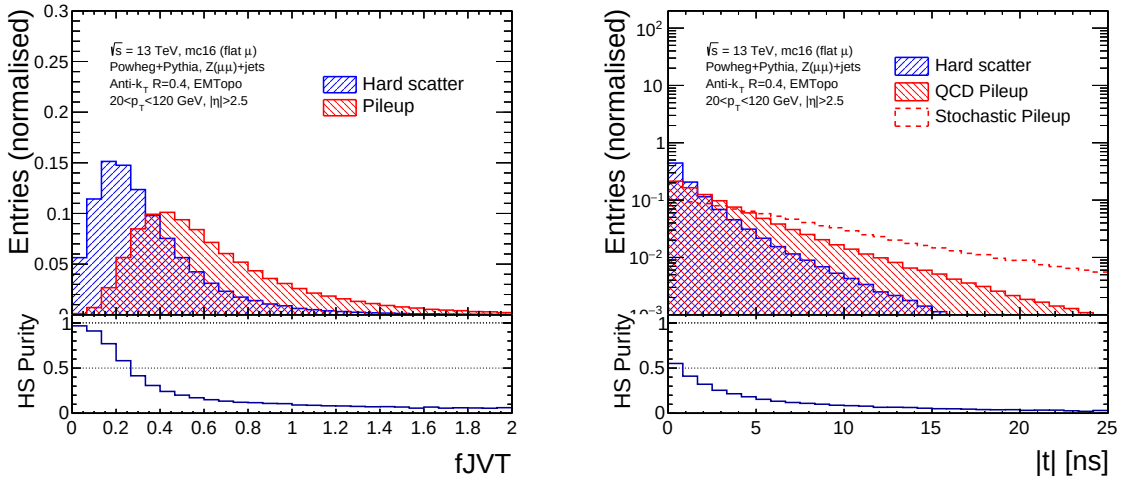

Figure 4.4: Comparative distribution, scaled to unity, of (left) fJVT for truth-matched HS and QCD-PU jets, and (right) jet timing for truth-matched HS, QCD-PU and stochastic PU jets in simulated $\sqrt{s} = 13$ TeV Z+jets events.

4.4 Improving the fJVT using jet shapes and kinematics

As previously mentioned, fJVT does not effectively reject stochastic pileup jets. In this regard, an extension of the fJVT is developed in this thesis scope, in an attempt to both improve the overall forward pileup-jet rejection, and to specifically deal with stochastic pileup. Stochastic pileup jets can be distinguished from HS and QCD-pileup jets with the help of information on their shape. They are generally expected to be wider and sparser than typical QCD jets. This information can be combined with the fJVT and timing information through the use of machine learning techniques.

Several multivariate methods were compared, including Boosted Decision Trees (BDT) and Deep Neural Networks (DNN) [88], that showed close to no differences in their classification performance, as shown in Figure 4.5. The three methods are defined and trained with a similar degree of optimisation, which is discussed in Section 4.4.1 for the selected method, the gradient-boosted BDT [85], that is found to give slightly better performance than the two other candidates, and the validation of its performance is discussed in Section 4.4.2.

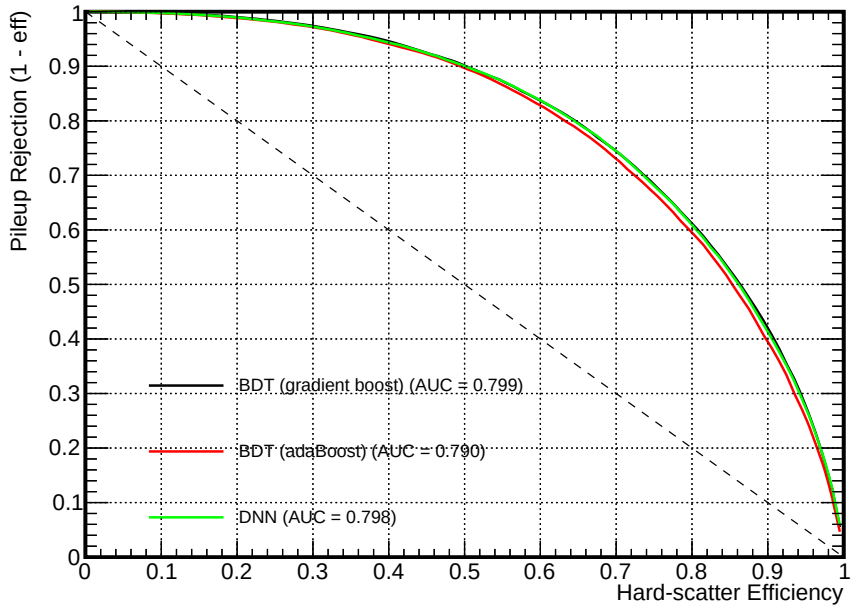

Figure 4.5: Comparison of the PU-jet rejection rate as a function of HS-jet selection efficiency for three multivariate discriminant, built using gradient-boosted (black) and adaBoost decision trees (red), anda simple feedforward DNN (green), trained on the same input set and events. The Areas Under the Curves (AUC) are shown, and can be used as a metric for comparison.

4.4.1 MVfJVT development and training

The dataset used for training is composed of calibrated jets from simulated $Z(\rightarrow \mu\mu)$+jets events, generated using the POWHEG [53] MC generator, showered with PYTHIA8 [34], Pileup interactions are overlaid on the actual generated events, with a flattened μ distribution with a mean $\langle\mu\rangle = 50$. This is not meant to reproduce the actual run conditions, but instead to be able to study physics behaviour in high pileup conditions, which is extremely useful for the studies presented later in this thesis. Events in the dataset are required to pass a very loose event selection. Exactly two muons are required in the event, that must satisfy the loose identification and isolation criteria. These muons are associated to form a Z boson candidate, that must satisfy $|M_Z^{\mathrm{PDG}} - M_{\mu\mu}| < 10$ GeV, as well as $p_{\mathrm{T}}^Z > 30$ GeV. All the jets from the events passing this selection are considered, if they satisfy $20 < p_{\mathrm{T}} \leq 120$ GeV and $|\eta| > 2.5$, with the upper p_{T} threshold justified by the relative softness that is generally expected for PU jets.

After the application of the event selection, a total 18.2 million jets are kept for training, of which 16.4 million categorized. Among the categorized jets, about 1.5 million are identified as

HS jets, 8.3 million as QCD-PU jets and 6.6 as stochastic PU jets. For the classifier training, the PU-jet category splitting into QCD-PU and stochastic PU is not used, preferring instead the more general PU category.

The pileup jet contamination heavily depends on several variables of interest for physics analysis, on which the tagger ideally shouldn't rely in order to avoid introducing biases in the performance toward the more contaminated regions. The main focus for these are the jet p_{T}, and the number of interaction per bunch crossing μ. For the former, pileup jets are in majority low-p_{T} jets, but pileup jets can also be seen, to a lower extent, in high-p_{T} regimes, and such high-p_{T} pileup jets should ideally be removed just as well as low-p_{T} pileup jets. For what concerns μ, the HS jet rate is expected to be constant with respect to this variable, while the QCD-PU jet rate is expected to increase roughly linearly, and the stochastic pileup rate faster than linearly.

Additionally, the performance boost arising from the addition of jet shape information can depend on the detector's granularity. Focusing on the forward region only, a clear change in resolution appears when passing $|\eta| = 3.2$, going from the end-cap calorimeter systems to the lower-granularity FCal. Comparisons of these three variables for HS, QCD-PU and stochastic PU jets are shown in Figure 4.6.

For the reasons mentioned above, the choice is made to split the training in bins of p_{T}, $|\eta|$ and μ. The p_{T} binning is defined taking into consideration the limited statistics available for the classifier training, especially for the higher p_T regime. Four p_{T} bins are used, with $20 < p_{\mathrm{T}} \leq 30$ GeV, $30 < p_{\mathrm{T}} \leq 40$ GeV, $40 < p_{\mathrm{T}} \leq 50$ GeV and $p_{\mathrm{T}} > 50$ GeV. Two bins in η are used, $2.5 < |\eta| \leq 3.2$ and $3.2 < |\eta| \leq 4.5$ as an attempt to improve performance in the less granular FCal. For what concerns μ, two bins are also used, $0 < \mu \leq 50$ and $\mu > 50$. This binning allows to get a roughly equivalent yield of HS jets in both bins, thanks to the specific μ profile of the training sample. The imbalance of the HS and PU yields, enhanced by the overall differences of their kinematics, is mitigated by applying a down-sampling procedure, aiming at obtaining comparable number of jets in each of the training bins. Jets are randomly discarded in order to obtain in each bins the same number of HS and PU jets. For the lower p_{T} ranges, PU jets are discarded, while above $p_{\mathrm{T}}^{\mathrm{jet}} = 50$ GeV, the HS jet contribution becomes dominant, and these are down-sampled.

An alternative approach to reduce the dependence on p_{T}, $|\eta|$, and μ was also considered, consisting in a 3-dimensional reweighting of the HS and PU events to the same spectrum, but was found to create very large weights, and correspondingly large statistical fluctuations, in the distribution tails, leading to instabilities in the training.

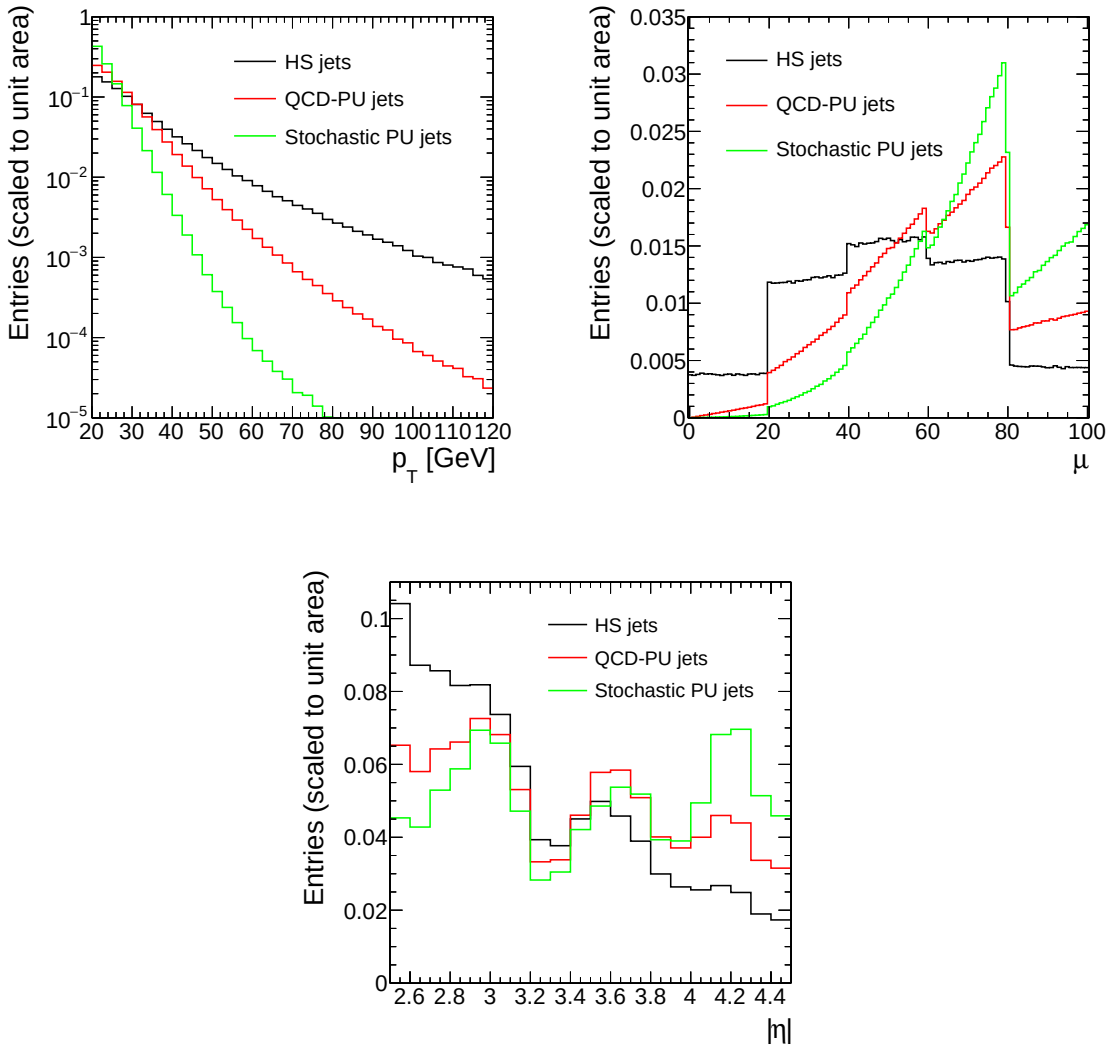

Figure 4.6: Comparative distributions, scaled to unit area, of p_{T} (top-left), μ (top-right) and $|\eta|$ (bottom) for truth-matched HS, QCD-PU and stochastic PU jets in the simulated Z+jets events used for the MVfJVT training.

The set of input variables is optimised through an iterative process, in which a classifier is first trained with a large set of input variables. The relative importance of each input variable i is then evaluated by training a new classifier with the variable removed from the input set, and computing the relative impact δ_i as

$$\delta_i = \frac{AUC_{\text{tot.}} - AUC_i}{\sum_i AUC_i}, \tag{4.8}$$

where $\text{AUC}_{\text{tot.}}$ and AUC_i are the area under the HS efficiency vs PU rejection curve (ROC curve) for the classifier trained with the full set of variables, and with the full set minus variable i respectively. Input variables are ranked according to their δ_i. The input variables yielding a negative δ_i in all of the training bins are removed, before starting a new iteration of the ranking.

A wide collection of jet kinematics and shape variables was tested, as well as quality variables used for other object reconstruction and calibration purposes. Among these variables, although most are precomputed and used for physics or calibration purposes, a fairly large fraction are specifically designed for the forward pileup tagging improvement.

A final selection of eight variables is used. This selection is common to all the training ranges in order to simplify the tagger definition and implementation. It was verified that no variable induces any significant loss of performance in any of the training ranges.These variables are listed and described in Table 4.1. The variable indexed "lead" are computed from the cluster with the highest energy among the jet components. The variable indexed "sum" are all energy-weighted sum of clusters in an enlarged radius of $R = 0.6$ with respect to the jet axis. This definition is chosen in order to account for the environment in which the jet is measured.

The distributions of the three most discriminative among them are shown in Figure 4.7. These are the jet timing $|t|$, width w, and the isolation moment ISO_{sum}. One can note that all these variables behave differently between HS and QCD-PU jets, not only for stochastic jets, although the latter category is overall more easily identifiable.

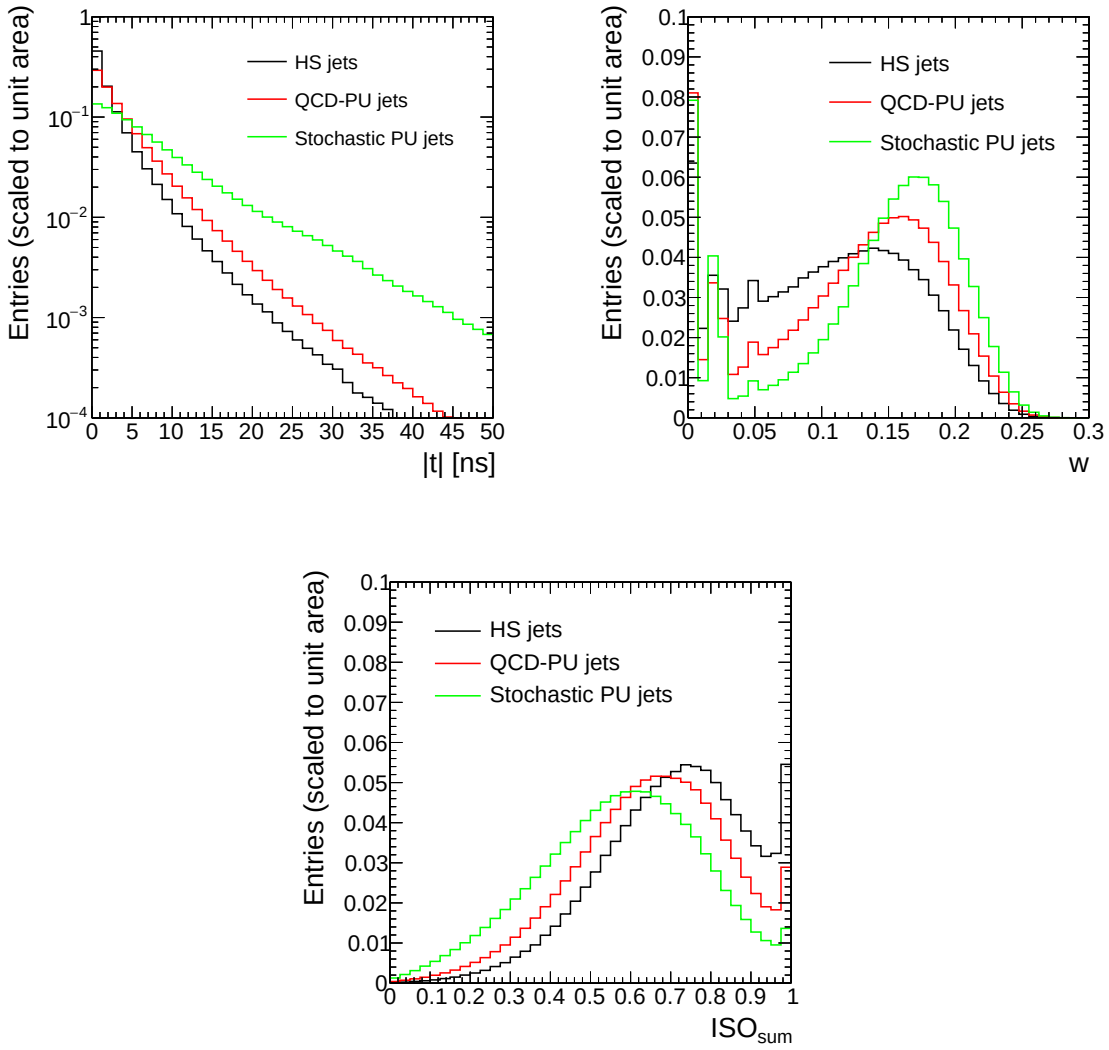

Figure 4.7: Comparative distributions, scaled to unity, of representative variables used as inputs to the MVfJVT training. The distributions shown are the jet timing (top-left), jet width (top-right), and isolation moment (bottom).

Table 4.1: List and description of the inputs to the MVfJVT training.

Variable	Description
fJVT	See Section 4.3.
$\|t\|$	Jet timing, see Section 4.3.
w	Jet calorimeter width, defined as $w = \frac{\sum \Delta R(\text{jet,constit.}) p_{\text{T}}^{\text{constit.}}}{\sum p_{\text{T}}^{\text{constit.}}}$
$\langle\lambda^2\rangle_{\text{lead}}$	$\langle\lambda^2\rangle = \frac{1}{E_{\text{cluster}}} \sum_{\text{cell}\in\text{cluster}} E_{\text{cell}}\lambda_{\text{cell}}^2$, where λ is the distance of the cell to the shower center along the shower axis.
$\sigma_\eta^{\text{lead}}$	$\sigma_\eta^{\text{lead}} = \cosh(\eta_{\text{lead}})\text{atan}(\frac{\sqrt{\langle r^2\rangle}}{\lvert\vec{c}\rvert})$, where and $\vec{c}$ and r are respectively the shower center and the cell relative distance to the shower center
$\text{P(EM)}_{\text{sum}}$	Energy-weighted sum of the cluster probabilities to originate from an EM shower.
ISO_{sum}	Energy weighted sum of the cluster isolation moment, defined as the energy fraction of non-clustered cells within the cluster radius.
E_{sum}	Sum of cluster energies

4.4.2 Performance validation

In order to assess the performance of a trained discriminant, the first step is to evaluate them using independent data, fully statistically decorrelated from the training sample. These curves compare the HS efficiency to the PU rejection for a pseudo-continuous scan of cuts on the discriminants. The MC sample used to validate the performance is also composed of simulated EMTopo jets from Powheg+Pythia Z+jets events, this time considering Z decays into e^+e^- pairs as well, and overlayed with a pileup distribution that tries to reproduce accurately the Run 2 conditions. To get a performance estimate closer to real analysis conditions, an additional requirement of $\Delta\phi(j, Z) > 2.8$ is applied on top of those already used to define the training sample. This is done in order to enhance the HS jet purity, as jets from these events are typically expected to be recoiling against the Z boson, while PU jets distribution is expected to be flat with respect to this variable. This cut effectively removes 90 % of the pileup jets in the selection, while conserving a relatively high HS jet efficiency of about 63 %. The selection it defines is later on referred to as the HS Control Region (HS-CR).

The performance is estimated in the HS-CR by comparing the ROC curves obtained from the MVfJVT distribution and those obtained with the fJVT and fJVT+$|t|$ as originally used for the forward PU mitigation. These are shown in Figure 4.8 for two representative training

ranges, chosen here to illustrate the largest and lowest gain in performance over the currently recommended fJVT + $|t|$ cuts. The training range that shows the most improvement from the use of MVfJVT contains jets with $30 < p_{\mathrm{T}} \leq 40$ GeV, $2.5 < |\eta| \leq 3.2$, for events with $\mu > 50$, and shows a 16 % improvement in terms of the area under the ROC curve (AUC). Jets with $50 < p_{\mathrm{T}} \leq 120$ GeV, $2.5 < |\eta| < 3.2$ and for $\mu < 50$, shows a more modest, but still non-negligible improvement of about 2 % in the AUC. The relatively lower improvement is simply explained by the very low PU contamination in this regime, as PU jets tend to be low p_{T} jets, and are by definition less present in lower μ regimes. Significant improvement of the performance over fJVT+$|t|$ is found in each of the training ranges. One may note that the peak improvement is not reached for the lowest p_{T} regime. This is only true for the AUC value. When comparing the best range from Figure 4.8 to the $20 < p_{\mathrm{T}} \leq 30$ GeV range with same $|\eta|$ and μ requirements in terms of fixed-cut improvements, it is seen that for a PU rejection equivalent to that of the Tight fJVT working point, a better HS jet efficiency improvement is observed in the lower p_{T} range (37 %) than in the $30 < p_{\mathrm{T}} \leq 40$ GeV range.

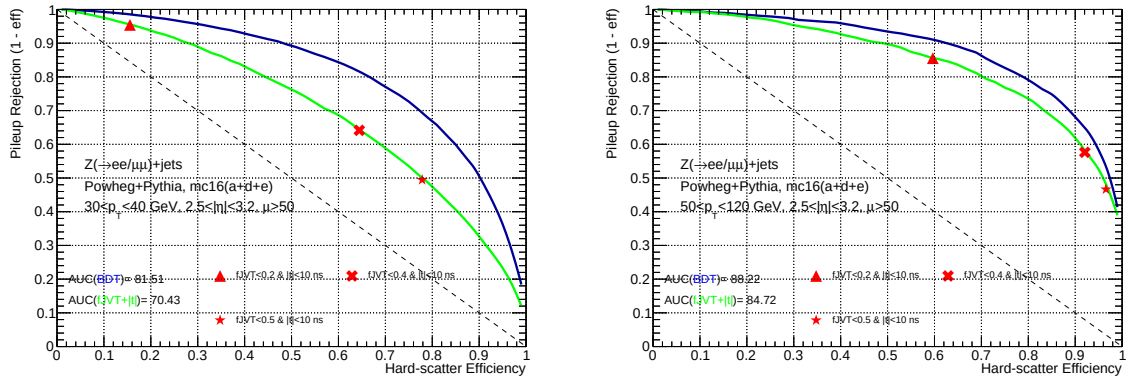

Figure 4.8: ROC curves for the MVfJVT in the training ranges in which the most (left) and least (right) improvement is achieved compared to the EMTopo fJVT. The loose (star) and tight (cross) fJVT working points are shown, as well as a tighter working point (triangle) that is under consideration. The Areas Under the Curves (AUC) are given in percent.

For a clear comparison of MVfJVT to fJVT, three working points are defined for the MVfJVT. These are defined to obtain the same pileup rejection, as seen in simulation, as the one obtained with fJVT. To account for the composite nature of the MVfJVT discriminant, the cuts are defined individually for each of the training bins. The performance of the MVfJVT is compared to those of the fJVT, in Section 4.5.3.

4.5 Calibration studies for the forward taggers

MC generators are generally not modelling processes with a perfect accuracy, and pileup, especially, is known to be poorly modelled. On top of that, mismodelling can occur due to imperfect simulation of the detector response, which can affect, for instance, the jet shape variables used in the MVfJVT definition. For this reason, the tagging efficiencies of the pileup taggers that are seen in MC are not to be trusted entirely, and one should look directly at the actual data in order to evaluate them.

When discrepancies are seen between the performance estimates in data and MC, it is desirable to correct the prediction to have it match data more closely. Although the possible data-MC discrepancies can be influenced by some analyses-specific behaviour, the calibration is typically done centrally by comparing data and MC for some representative processes, in order to extract generic correction factors, and evaluate the related uncertainties, that each individual analysis can then simply apply as needed.

4.5.1 Calibration methodology

In the case of forward pileup taggers, the calibration compares data to the Z+jets events from the validation samples, and for a fair comparison, both data and MC are passed through the same event and jet selection process described in Section 4.4. Such calibration also requires to identify the HS and PU jet contributions in data. Two methods are used for this purpose, both aiming at estimating the HS-jet efficiency of the tagger's working points in the HS-CR. One of these methods uses dedicated zerobias data and minimum-bias MC events to estimate the PU jet yield in the HS-CR. For the second method, the PU jet yield is constrained in a PU-pure control region, referred to as the PU-CR later on, and extrapolated to the HS-CR. The need for two distinct methods is justified by the specificities in the technical implementation of the fJVT for EMTopo jets and PFlow jets.

The first method is used for the EMTopo taggers calibration, both fJVT and MVfJVT. Due to the random nature of the zerobias trigger, the zerobias events are almost exclusively multijet events, as the inelastic scattering cross-section ($\mathcal{O}(100$ mb$)$) is several order of magnitude larger than the most common electroweak processes (e.g. $\mathcal{O}(100$ nb$)$ for the inclusive W boson production) at the LHC center-of-mass energy. The jets from these events can be used to evaluate the kinematic behaviour of PU jets. To emulate this approach in simulations, minimum bias (minbias) MC are used. These are the simulated events that are used to simulate pileup, which are generated similarly to those overlayed to the Powheg+Pythia8 Z+jets validation samples.

The event selection described in Section 4.4 cannot be applied to zerobias and minbias events, as these typically do not contain leptons. In order to obtain representative distributions of PU jets, both in yield and kinematic behaviour, these datasets are scaled down to match the yield of data (MC for minbias) events passing the Z+jets event selection. The same $20 < p_{\mathrm{T}}^{\mathrm{jet}} \leq 120$ GeV and $2.5 < |\eta^{\mathrm{jet}}| < 4.5$ criteria are then applied to select jets from the zerobias and minbias samples. The $\Delta\phi(j, Z) > 2.8$ that defines the HS-CR selection can't be applied either due to the absence of a Z boson. An additional scale factor of $1 - \frac{2.8}{\pi}$ is therefore applied in order to simulate it, safely assuming that the PU distribution with respect to $\Delta\phi(j, Z)$ is constant, which is verified in the Z+jets MC, as shown in Figure 4.9.

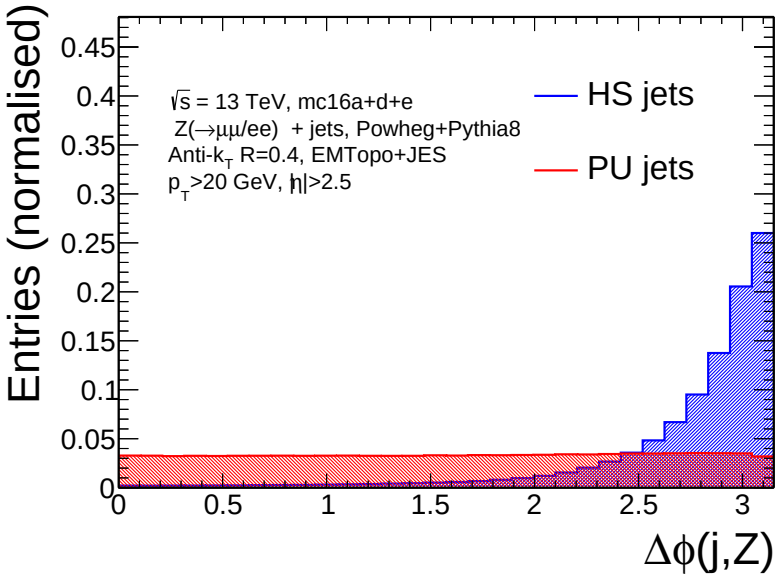

Figure 4.9: Comparative distribution of $\Delta\phi(j, Z)$ for PU jets (blue) and HS jets (red), from simulated Z+jets events.

The fJVT computation differs slightly for the zerobias and minbias samples. As these are supposed to be pure pileup samples, there is no need to define and remove the HS vertex, as it is done in the default fJVT computation.

The modelling of the input variables could not be checked directly with the training sample due to its flat μ profile. It can however be looked at with the samples used for the taggers calibration, as shown in Figure 4.10, for jets with $30 < p_{\mathrm{T}} \leq 40$ GeV and $2.5 < |\eta| \leq 3.2$.. This figure includes both a comparison of data and MC, generated using Powheg+Pythia8, and a comparison of minbias MC and zerobias data, that illustrates the modelling of the contribution from pileup jets. Non-negligible differences are observed between the data and MC predictions for the three variables shown, and appear to be the largest in regions where both the pileup

contribution and the discrepancy between minbias MC and zerobias data are the largest.

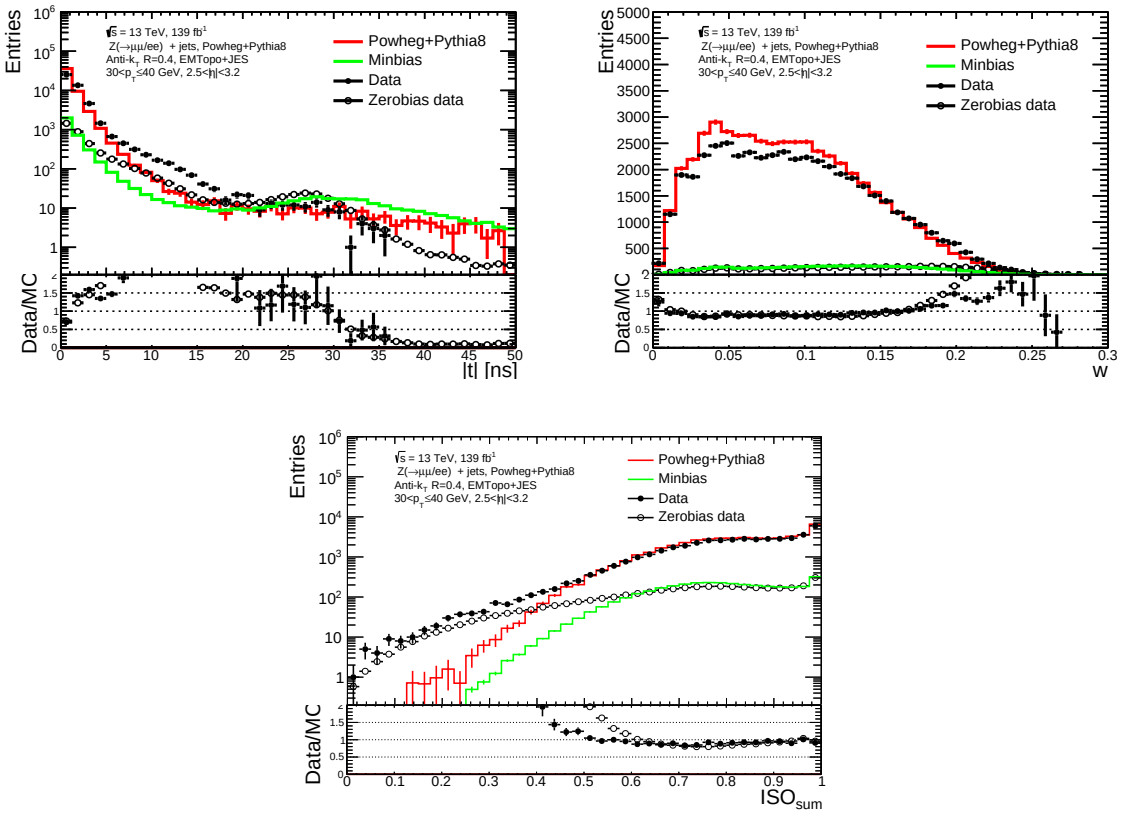

Figure 4.10: Distribution of the jet timing $|t|$ (top-left), jet width w (top-right) and isolation moment $\mathrm{ISO}_{\mathrm{sum}}$ (bottom). The full (empty) points shows the data (zerobias) distribution, while the red (green) histogram shows the MC (minbias) distribution. Bottom plots are displaying the ratios Data/MC (full dots), and Zerobias/minbias (empty dots). In the ratio panels, points with a ratio value larger than two are not represented.

A similar observation can be made from the data-to-MC comparison for the fJVT and MVfJVT shown in Figure 4.11. These differences are especially important for the fJVT, as the high-PU-contamination region also corresponds to jets surviving the tagging cut, potentially enhancing the uncertainty on the HS and PU efficiencies estimation.

For PFlow jets, the fJVT computation is done at an early stage of the data processing, and, due to software technicalities, does not allow to easily estimate the variable for zerobias data and minbias MC. For these jets, the PU-CR is defined is defined by applying the same requirements as for the HS-CR definition, but with a different requirement on the azimuthal angle between the Z boson and the jet, of $\Delta\phi(j, Z) < 1.2$. This cuts removes a large majority of HS-jets, peaked at $\Delta\phi(j, Z) = \pi$, while conserving about 38% of PU jets. To account for

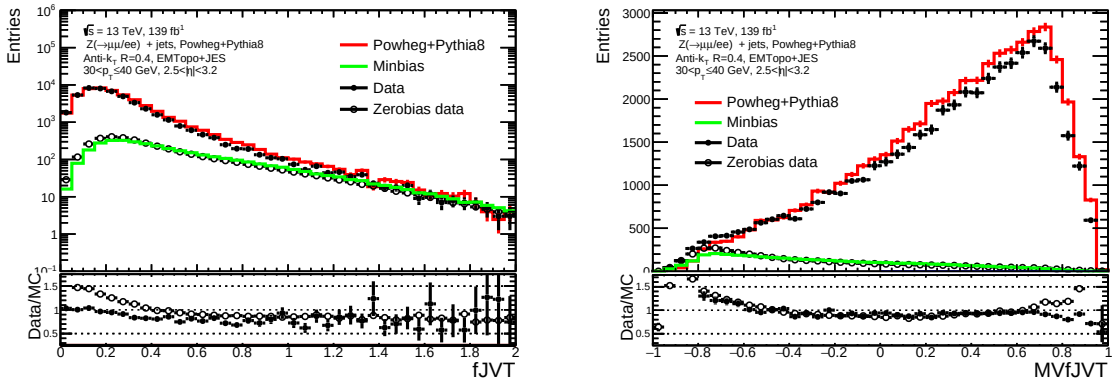

Figure 4.11: Distribution of fJVT (left) and MVfJVT (right). The full (empty) points shows the data (zerobias) distribution, while the red (green) histogram shows the MC (minbias) distribution. Bottom plots are displaying the ratios Data/MC (full dots), and Zerobias/minbias (empty dots). In the ratio panels, points with a ratio value larger than two are not represented.

the residual HS contamination, the yield of HS jets in this region is estimated using MC. The fraction of MC events with jets matched to HS jets at generator level is used to estimate the HS contamination, that is subtracted from data.The PU jet yield evaluated in the PU-CR can then be extrapolated to the $\Delta\phi(j,2) > 2.8$ HS-CR in order to perform the calibration as

$$\mathrm{N}_{\mathrm{PU}}^{(\Delta\phi>2.8)} = \frac{\pi - 2.8}{1.2}\left(\mathrm{N}^{(\Delta\phi<1.2)} - \mathrm{N}_{\mathrm{HS}}^{(\Delta\phi<1.2)}\right). \tag{4.9}$$

This method has the disadvantage of not being completely data-driven, and therefore a bit more sensitive to the MC mismodelling. Nevertheless, it was verified that it yields results comparable to those of the first method.

Once the PU contributions are estimated, HS efficiencies are derived similarly for both methods, and both taggers, as

$$\varepsilon_{\mathrm{HS}} = \frac{\mathrm{N}_{\mathrm{data}}^{\mathrm{pass}} - \mathrm{N}_{\mathrm{PU}}^{\mathrm{pass}}}{\mathrm{N}_{\mathrm{data}} - \mathrm{N}_{\mathrm{PU}}}, \tag{4.10}$$

where the "pass" index indicates that only jets passing a given fJVT or MVfJVT working point, mentioned in Section 4.3-4.4, are considered in the yield computation. In a similar way, PU efficiencies are also extracted for control purpose. They are expressed as

$$\varepsilon_{\mathrm{PU}} = \frac{\mathrm{N}_{\mathrm{PU}}^{\mathrm{pass}}}{\mathrm{N}_{\mathrm{PU}}}. \tag{4.11}$$

These efficiencies are evaluated for both data and MC. The HS efficiencies are then used

to extract efficiency scale factors to correct the MC prediction, computed as

$$\mathrm{SF} = \frac{\varepsilon_{\mathrm{HS}}^{\mathrm{data}}}{\varepsilon_{\mathrm{HS}}^{\mathrm{MC}}}. \tag{4.12}$$

In order to validate the choice of using two distinct methods, both the CR and zerobias PU estimation methods are compared in the evaluation of the EMTopo fJVT HS-jet selection efficiency, as exemplified in Figure 4.12, in which very similar results are seen for both methods.

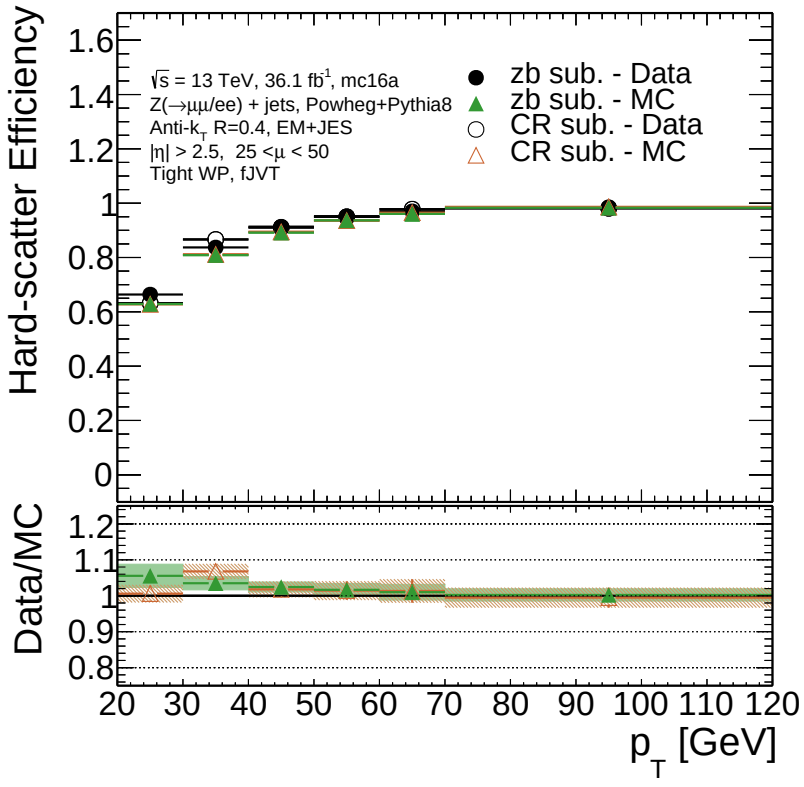

Figure 4.12: Comparison of the EMTopo HS-jet efficiencies of the fJVT using the zerobias (zb sub, full dots) or CR-based (CR sub, empty dots) PU estimation and subtraction method for 2015 and 2016 data and corresponding simulated Z+jets events. Black points show the efficiency in data, while the green and orange points are the efficiencies in MC for the MVfJVT and fJVT respectively. The ratio plot shows the corresponding scale factor values, following the same colour scheme, and with the bands showing the related total uncertainty.

4.5.2 Estimation of systematic uncertainties

The validity of the efficiency scale factors that are derived cannot be ensured with a perfect precision. It is necessary to evaluate the impact of all the potential sources of uncertainties, that can influence their determination.

Five different sources of uncertainties are considered for the evaluation of the fJVT and MVfJVT efficiencies.

The first, and most obvious one, is the potential impact of statistical fluctuations, arising from the limited event statistics. This is typically negligible in the lower p_{T} regimes, but becomes one of the largest uncertainties at high p_T. Both data and MC statistical uncertainties are considered. For data, it is simply computed as $\sqrt{\mathrm{N}}$, where N is the number of events in a given bin of the calibration, assuming a Gaussian behaviour of data. For MC, the same assumption is made, and $\sqrt{\sum w^2}$ is used as the uncertainty in each bin, accounting for the varying event weights w. These are computed separately for events passing and failing the working point cuts, in order to be properly propagated up to the scale factor computation, accounting for all correlations correctly.

The second source of uncertainty concerns the MC modelling dependence, as most use-cases are applying the fJVT tagger to events originating from other processes than Z+jets and can use different MC event generators than Powheg, or different algorithms from Pythia for the parton shower modelling. To get an idea of how the tagging performance changes depending on the modelling, the calibration procedure is performed using Z+jets events generated with an alternative MC generator. The choice is made to use Sherpa 2.2.1 for this purpose. Despite its very large statistics, the Sherpa 2.2.1 sample is constituted of events with very large event weights, creating large fluctuations in most of the distributions of interest for the study. In order not to account for them, which would mean counting twice the impact of MC statistics, the fluctuating distributions are smoothed following the procedure described in Ref. [89]. For the fJVT, no significant differences are seen between the scale factors estimation using Powheg+Pythia and Sherpa 2.2.1. For the MVfJVT, though, the discrepancy between these two generators is not negligible, and the difference between their respective scale factor values is used as an uncertainty band.

The third uncertainty source regards the PU estimation. For the zerobias and minbias PU estimate, some bias can appear in the fJVT performance, coming from the fact that the JVT is not applied to jets entering the fJVT computation, and due to the absence of an HS vertex. This actual bias entering here is hard to evaluate properly. In order to account for it, a $\pm 10\%$ uncertainty band on the evaluated PU contribution is defined, by comparing the minbias

PU estimate to the truth-matched PU estimate from Powheg+Pythia. For the alternative PU estimation method, such bias is not present, but the uncertainty is kept to cover the PU mismodelling.

Two additional contributions are considered in order to account for the consequences of the choice made to extract the scale factors in bins of p_T and μ only, in an effort to reduce the impact of statistical variations. Some slight differences in performance are known to appear when comparing the scale factors obtained for jets reconstructed in the end-cap and FCal. To account for these differences, an η-dependence uncertainty band is defined conservatively, as the symmetrised envelope of the difference between the nominal scale factor, and the scale factor evaluated in the two distinct $|\eta|$ regimes.

The last effect considered accounts for the different beam conditions that occurred during Run2. This is already partially accounted for by the μ binning of the scale factors, but some residual, non-negligible, differences are seen when comparing the performance for different periods. This is especially true when comparing performance evaluated with 2015 and 2016 data, to those evaluated in 2017 and 2018 for $\mu < 50$. Similarly to the η-dependence, the envelope of the scale factor difference between the nominal scale factor value and the values from each distinct year is used as the corresponding uncertainty band. This year-dependence is found to be negligible between 2017 and 2018 in the $\mu > 50$ regime, and the uncertainty is therefore only defined for $\mu < 50$.

The uncertainties are shown for the PFlow fJVT in Figure 4.13, and Figure 4.14 shows the relative impact of the uncertainties mentioned above on the EMTopo fJVT and MVfJVT scale factors in the $25 < \mu < 50$ range, for the three studied working points.

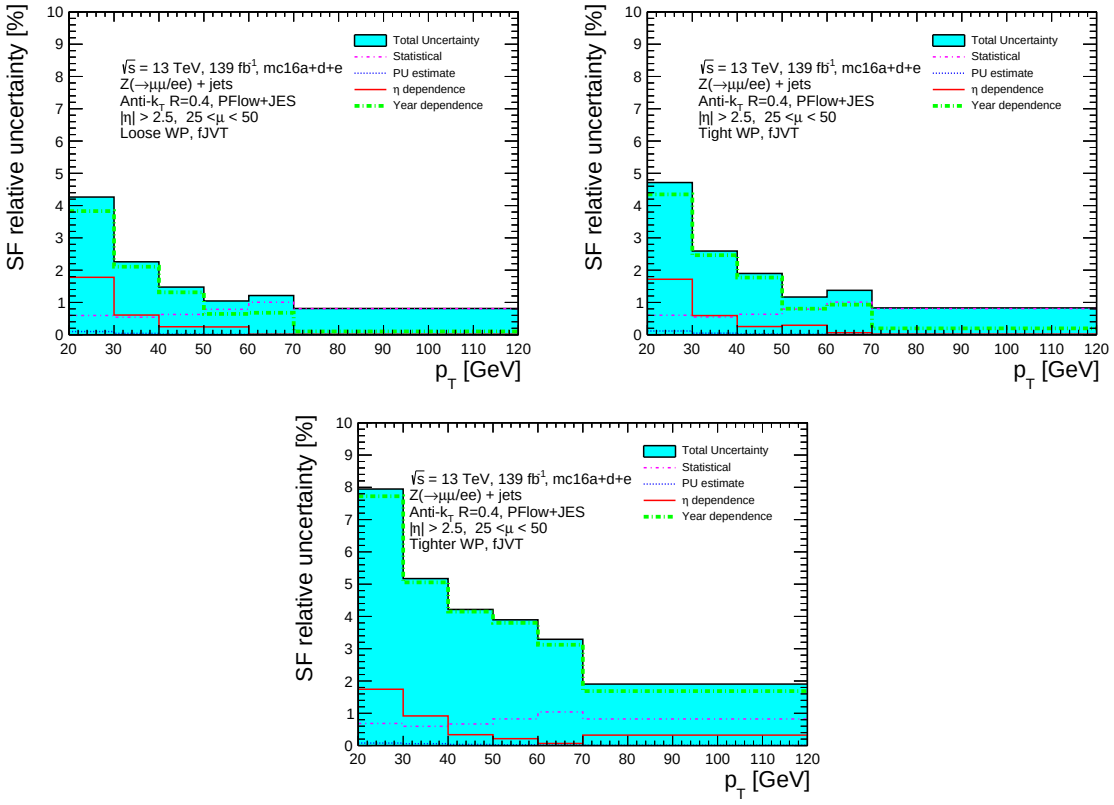

Figure 4.13: Relative uncertainties on the PFlow fJVT scale factors, with respect to the jet p_{T} for the loose (top-left), tight (top-right) and tighter (bottom) working points. The colored dashed and dotted lines shows each individual uncertainties, while the full black line shows their sum in quadrature.

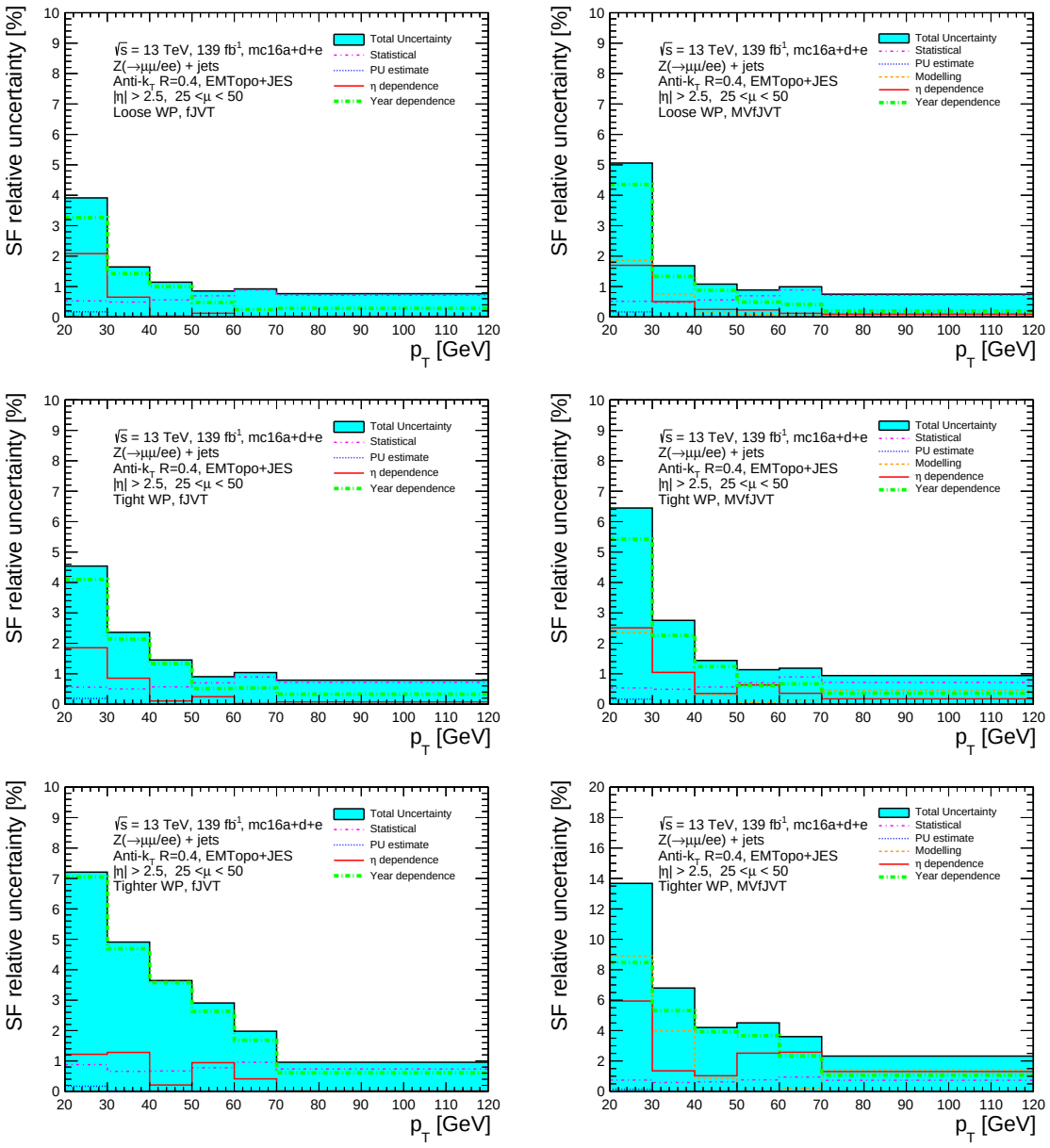

Figure 4.14: Relative uncertainties on the EMTopo fJVT (left) and MVfJVT (right) scale factors, with respect to the jet p_{T} for the loose (top), tight(middle) and tighter (bottom) working points. The colored dashed and dotted lines shows each individual uncertainties, while the full black line shows their sum in quadrature.

4.5.3 Calibration results

Scale factors have been extracted for both the fJVT and MVfJVT in the case of EMTopo jets. As mentioned in Section 4.5.2, the choice is made to define the scale factors in bins of p_{T} and μ. The p_{T} binning uses 10 GeV-wide bins from $p_{\mathrm{T}} = 20$ GeV to $p_{\mathrm{T}} = 70$ GeV, and a wider bin in the range $70 < p_{\mathrm{T}} < 120$ GeV, and was defined in order to get a low impact from the statistical uncertainty, while limiting the scale factor variation within each bin. The μ binning partly reproduces the binning used for the MVfJVT training, with an additional separation at $\mu = 25$, effectively providing scale factors in three distinct pileup regimes, with $\mu \leq 25$, $25 < \mu \leq 50$ and $\mu > 50$.

The fJVT and MVfJVT are compared in all these ranges, for the three working points defined previously. This comparison is illustrated in Figure 4.15, showing the HS efficiencies and scale factor comparisons in the $25 < \mu \leq 50$ regime. One can see that the MVfJVT yields overall better HS-jet efficiencies than the fJVT for similar PU-jet rejection rates, while the scale factors are overall consistent. This improvement comes with overall larger uncertainty, which is especially true for the tighter working point. This is due to the inclusion of the uncertainty on the MC modelling, which gets larger the tighter the cut applied on the MVfJVT is.

In Figure 4.16, the PU-jet efficiency is shown for the same μ regime. In this case, larger differences appear between data and MC, as it can be seen in the ratio plots. Although the MVfJVT working points have been defined to yield an equivalent PU efficiency as the fJVT, in reality the PU efficiency for the fJVT appears to be slightly better. This is due to the fact that the working point definition is not made while reproducing the PU-jet contamination estimation strategy used for the taggers calibration, but is based instead on the yield of truth-matched pileup jets, which is impacted by the ambiguity in the truth definition of HS and PU jets. Nevertheless, the effect is small overall, and is covered by the uncertainty on PU estimation.

The HS jet efficiency of the fJVT is finally compared between the EMTopo and PFlow jet collections in Figure 4.17. One can note here the very similar behaviour of the agreement between data and MC, and the corresponding uncertainties.

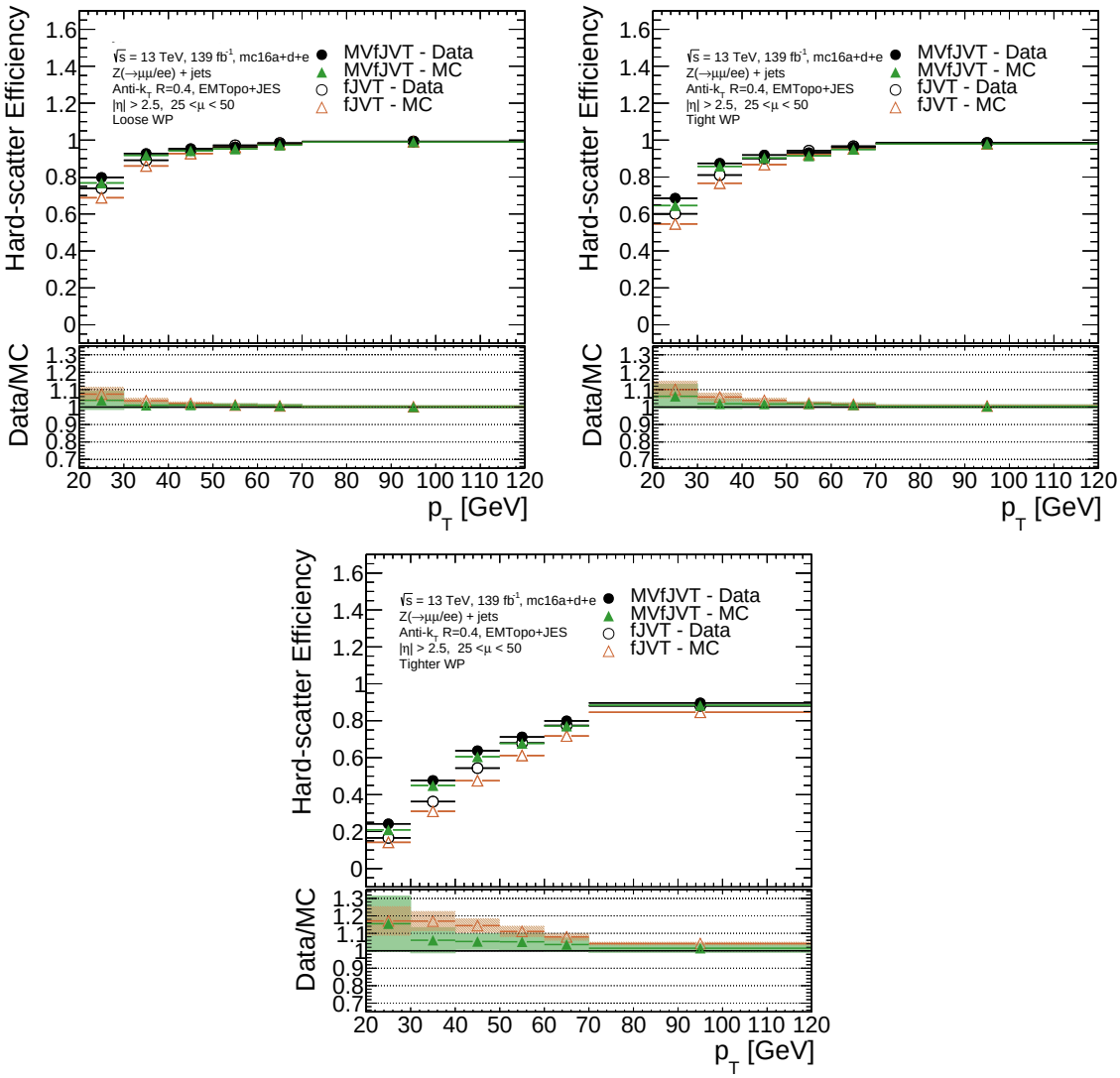

Figure 4.15: Comparison of the EMTopo HS-jet efficiencies of the MVfJVT (full markers) and fJVT (shallow markers), for the Loose (top-left), Tight (top-right), and Tighter (bottom) working points. Black points show the efficiency in data, while the green and orange points are the efficiencies in MC for the MVfJVT and fJVT respectively. The ratio plot shows the corresponding scale factor values, following the same color scheme, and with the bands showing the related total uncertainty.

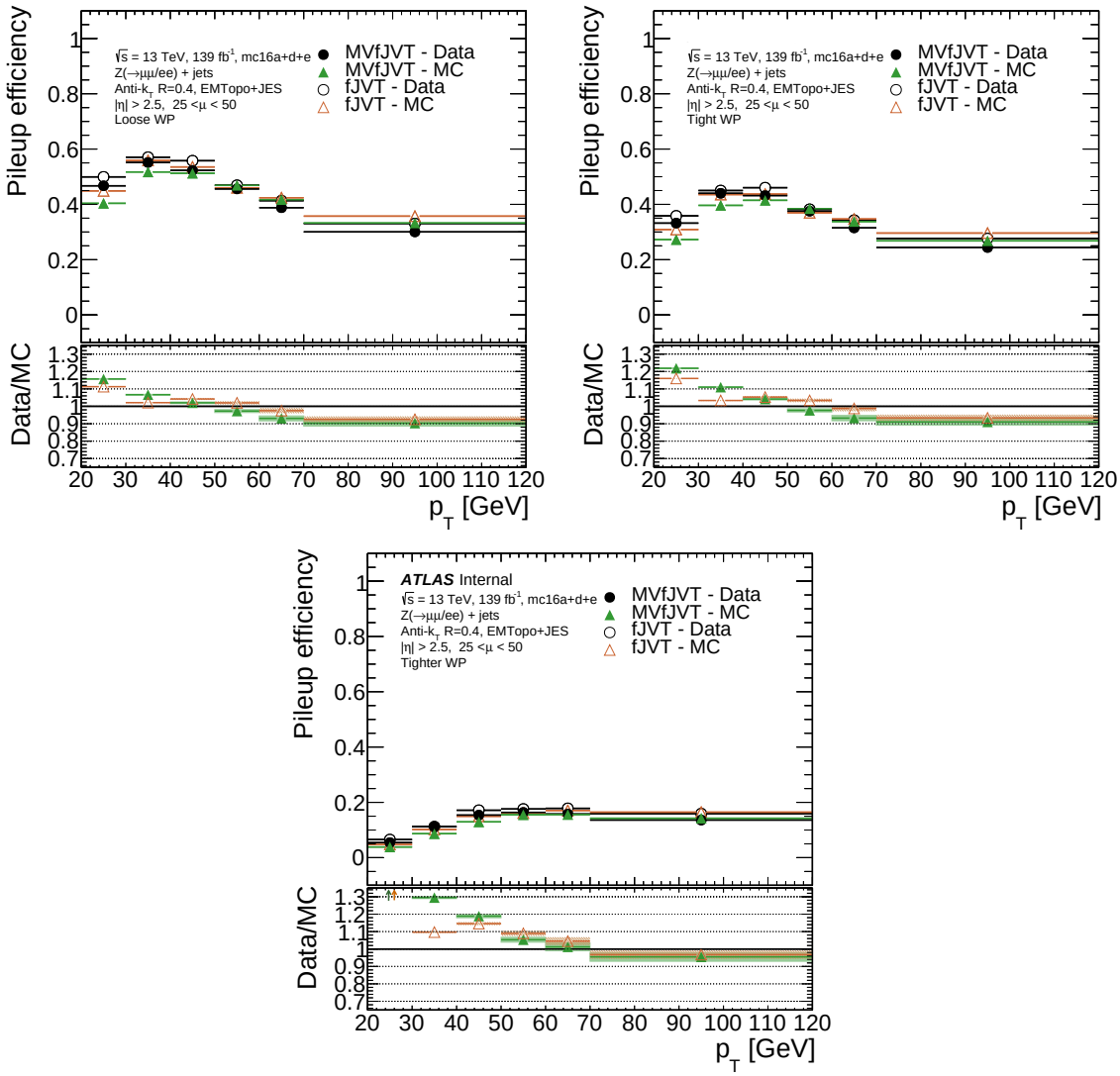

Figure 4.16: Comparison of the EMTopo PU-jet efficiencies of the MVfJVT (full markers) and fJVT (shallow markers), for the Loose (top-left), Tight (top-right), and Tighter (bottom) working points. Black points show the efficiency in data, while the green and orange points are the efficiencies in MC for the MVfJVT and fJVT respectively. The ratio plot shows the corresponding scale factor values, following the same color scheme, and with the bands showing the related statistical uncertainty.

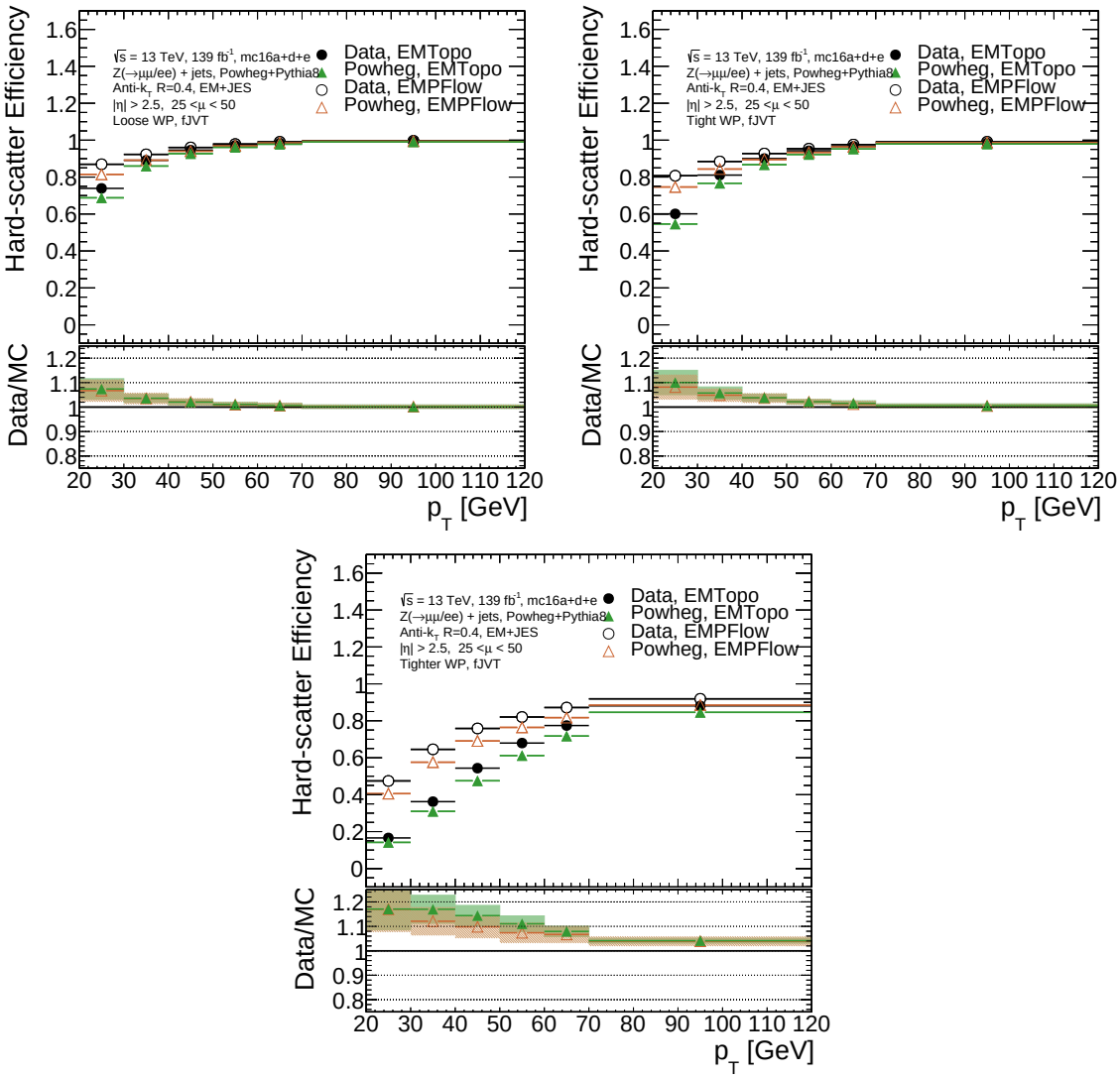

Figure 4.17: Comparison of the EMTopo (full markers) and PFlow (empty markers) HS-jet efficiencies of the fJVT, for the Loose (top-left), Tight (top-right), and Tighter (bottom) working points. Black points show the efficiency in data, while the green and orange points are the efficiencies in MC for EMTopo and PFlow jets respectively. The ratio plot shows the corresponding scale factor values, following the same colour scheme, and with the bands showing the related total uncertainty.

4.5.4 Quark/gluon dependence of the MVfJVT

The calibration of the MVfJVT is presented in Section 4.5.3. However, it is still considered as preliminary, as an important point of concern is still under investigation, regarding the dependence of the tagger on the quark-gluon composition of the data samples used for the training and the estimation of the performance.

The effect is already evaluated in simulations. Detector-level jets from the simulated $Z+jets$ events used for training and validation can be split into quark-initiated and gluon-initiated jets by matching them to particle-level jets with the initial parton well-identified, allowing to compare the MVfJVT distribution and tagging performance between the two categories, as shown in Figure 4.18. This figure shows that a better separation is expected for HS quark-jets than for HS gluon-jets with the MVfJVT, which is not the case with the fJVT. The effect is caused by the inclusion of jet-shape information into the MVfJVT, as gluon jets tend to be broader than quark jets [90, 91].

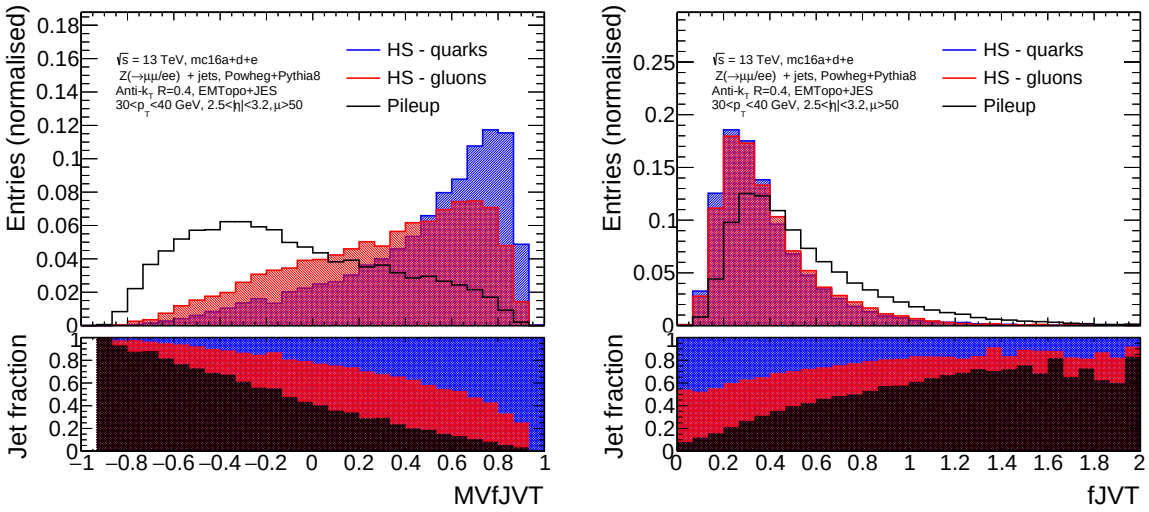

Figure 4.18: Comparison of the HS quark-jets and gluon-jets to the PU jets distributions of the forward pileup jet taggers MVfJVT (left) and fJVT (right). Th ratio plots show the relative fraction of each categories.

Although the effect is clearly identified in simulation, the relevant impact for the calibration is that on the agreement of data and simulation in terms of the HS efficiency. This cannot be evaluated through the current calibration procedure, as the quark-gluon composition in data is not known a priori. This could be studied in the future by evaluating the performance for different probe processes, with different representative quark-gluon fractions.

4.6 Summary and discussion

A new forward pileup-jet tagger has been developed. It combines the original forward pileup-jet tagging tool to shape and structure information about jets into a powerful multivariate discriminant, that allows the identification and suppression of stochastic pileup jets above $|\eta| = 2.5$. This new tagger is found to improve the overall tagging performance by up to 25 % in the kinematic regions in which the pileup-jet contamination is found to be the largest. The calibration of this new tagger for EMTopo jets, and that of the fJVT for both EMTopo and PFlow jets has been performed. The MVfJVT is found to yield a better overall agreement between its performance in data and simulation, hence requiring overall smaller corrections to its efficiency. Both forward-pileup-jet taggers are now implemented in the ATLAS software, and available, although preliminarily for the MVfJVT, for all the analyses of ATLAS data.

The forward PU-jet tagger performance is evaluated using Run 2 data, in which the mean number of pileup interactions is still relatively low, at $\langle\mu\rangle = 33.7$. The MVfJVT performance demonstrates the potential of multivariate methods for such purpose in this context. However, the suppression of pileup-jets is expected to become challenging in future LHC Runs, and especially with the $\langle\mu\rangle = 200$ pileup interactions expected at the HL-LHC. The impact from such conditions will be highly reduced, notably thanks to the many hardware developments foreseen for the phase-2, such as the extending tracking coverage up to $|\eta| = 4.0$ and tracking performance improvements from the ITk [92], or the potential addition of precise timing information with the HGTD [93]. In addition, potential improvements could arise from improving the tagger definition, by taking advantage of lower-level information, such as tracks, calorimeter cells, cell clusters or tower energies and positions, and of more advanced classifier definitions to develop more complex and better performing algorithms, as already studied, for instance, in the scope of flavour tagging and quark-gluon tagging [94, 95].

The main remaining study concerning the MVfJVT is its quark-gluon fraction dependence, discussed in Section 4.5.4. Although this feature appears as potential source of uncertainty on the pileup-tagging performance, it also indicates that similar information to that used in the MVfJVT definition could potentially be used to extend the quark-gluon tagging capability outside its current tracking-limited acceptance [96], and the development of a similarly-defined tool specialised in the quark-gluon separation could be foreseen.

Chapter 5

Observation of Electroweak $WZjj$ production and related studies

This chapter focuses on the various studies performed regarding the observation of the fully leptonic electroweak $WZjj$ production ($WZjj$-EW), performed with 36 fb^{-1} of data collected in 2015 and 2016. The analysis is described, and the main challenges in studying the process, and the solutions proposed to handle them, are discussed, most notably the mitigation of the large background contamination arising from the $WZjj$-QCD production. Section 5.1 lays the basis of the analysis, by describing the details of the analysis object reconstruction and event selection. The details of the event selection and object reconstruction are presented Section 5.1.3. The methodology and tools used to extract the WZjj-EW signal from the data are explained in Section 5.2. The results leading to the observation of the WZjj electroweak production are presented and discussed in Section 5.3. Most of Section 5.2 corresponds to developments performed by the WZ analysis group of ATLAS, from which the optimisation of the selection of jets was performed as part of this thesis work. All developments presented in Sections 5.2 and 5.3 represents personal contributions to this published measurement.

5.1 Event selection

The event selection of the $WZjj$-EW analysis discussed in this section is in large part based on the selection performed for the inclusive WZ analyses. This analysis studied a final state with the same leptonic activity as $WZjj$-EW, and was continuously updated and optimised from the first publication based on Run 1 data [58] to the more recent results using 36 fb^{-1} of data [46]. The lepton selection used there, and vector boson reconstruction strategies were optimised to obtain excellent suppression of the non-WZ background, typically entering the selection due to misidentification of the final state leptons, and are therefore well adapted to the studies presented in the following sections.

These lepton selections and boson reconstruction methods are respectively discussed in Section 5.1.1 and Section 5.1.2. These are followed, in Section 5.1.3, by a description of the jet

selection, which is specific to the $WZjj$-EW analysis, and has a large impact on the sensitivity to the processes of interest.

5.1.1 Lepton selection

The W and Z bosons decays that are targeted are exclusively the leptonic ones, excluding τ leptons due to their poor reconstruction accuracy. The final state therefore has to be composed of two same-flavour (e or μ), opposite-charge leptons, corresponding to the decayed Z boson, in addition to a third lepton and a neutrino originating from the W boson decay. For this reason, lepton triggers are used for the analyses. These events are then considered as potential WZ event candidates if they satisfy the requirements of at least one of the following single-lepton triggers[1]:

- At least one muon with $p_T \geq 50$ GeV
- At least one loosely isolated muon with $p_T \geq 26$ GeV
- At least one electron with $p_T \geq 140$ GeV and passing loose identification criteria
- At least one electron with $p_T \geq 60$ GeV and passing medium identification criteria
- At least one electron with $p_T \geq 26$ GeV passing tight identification criteria, and loose isolation criteria

Events collected during data-taking periods that do not belong to the so-called Good-Run List (GRL) are discarded. This list compiles all the data-taking periods for which no technical issues occurred, such as unstable beam conditions or important detector defects. This ensure that all events are measured in periods of good detector and accelerator activity, and benefit from the full subsystem array for their reconstruction. Reconstructed leptons from these events, calibrated as described in Section 3.1 and Section 3.2, are passed through a three-level selection process, with each level presenting various degrees of tightness. These are referred to as, in increasing order of tightness, baseline lepton selection, Z-lepton selection, and W-lepton selection. These are defined so that for a lepton to pass the Z-lepton selection it has to already pass the baseline selection, and equivalently any boson passing the W-lepton selection already passed the Z-lepton selection.

The selection criteria are adapted to whether the lepton is an electron or a muon, and are summarized in Table 5.1 for electrons, and Table 5.2 for muons.

[1] The trigger mentioned here are those used for 2016-2018 data. 2015 triggers are defined similarly, but with slightly looser p_T requirements.

Table 5.1: Three levels of electron object selection used in the analysis.

Electron object selection			
Selection	Baseline selection	Z selection	W selection
$p_{\mathrm{T}} > 5$ GeV	✓	✓	✓
Electron object quality	✓	✓	✓
$\lvert\eta^{\mathrm{cluster}}\rvert < 2.47$, $\lvert\eta\rvert < 2.5$	✓	✓	✓
Loose identification	✓	✓	✓
$\lvert d_0/\sigma(d_0)\rvert < 5$	✓	✓	✓
$\lvert\Delta z_0 \sin\theta\rvert < 0.5$ mm	✓	✓	✓
Loose isolation	✓	✓	✓
e-to-μ and e-to-e overlap removal	✓	✓	✓
e-to-jets overlap removal		✓	✓
$p_{\mathrm{T}} > 15$ GeV		✓	✓
Exclude $1.37 < \lvert\eta^{\mathrm{cluster}}\rvert < 1.52$		✓	✓
Medium identification		✓	✓
Gradient isolation		✓	✓
$p_{\mathrm{T}} > 20$ GeV			✓
Tight identification			✓
Unambiguous author			✓

Table 5.2: Three levels of muon object selection used in the analysis.

Muon object selection			
Selection	Baseline selection	Z selection	W selection
$p_{\mathrm{T}} > 5$ GeV	✓	✓	✓
$\lvert\eta\rvert < 2.7$	✓	✓	✓
Loose quality	✓	✓	✓
$\lvert d_0/\sigma(d_0)\rvert < 3$ *(for $\lvert\eta\rvert < 2.5$ only)*	✓	✓	✓
$\lvert\Delta z_0 \sin\theta\rvert < 0.5$ mm *(for $\lvert\eta\rvert < 2.5$ only)*	✓	✓	✓
Loose isolation	✓	✓	✓
μ-jet Overlap Removal		✓	✓
$p_{\mathrm{T}} > 15$ GeV		✓	✓
$\lvert\eta\rvert < 2.5$		✓	✓
Medium quality		✓	✓
$p_{\mathrm{T}} > 20$ GeV			✓
Tight quality			✓
Tight isolation			✓

The baseline selection requires both electrons and muons to satisfy $p_{\mathrm{T}} > 5$ GeV. Only muons within $|\eta| < 2.7$, and electrons within $|\eta| < 2.5$ are considered. Additionally, the calorimeter clusters from electron candidates must satisfy $|\eta^{\mathrm{cluster}}| < 2.47$. Both electron and muon candidates are also required to pass loose identification and isolation criteria, and in the case of muons, track-to-vertex matching criteria on the d_0-significance, $|d_0/\sigma(d_0)| < 3$, and on the longitudinal parameter, $|\Delta z_0 \sin\theta| < 0.5$ mm, are also applied. Similar track-to-vertex matching criteria are also applied to electrons at reconstruction level, as explained in Section 3.1. In order to avoid any double-counting of the leptons, an overlap-removal is finally performed. If an electron is found to share a track with a muon, the electron is removed, and if two electrons overlap, only the leading-p_{T} electron is kept.

Z-leptons are defined as baseline leptons passing tightened requirements. These are required to satisfy $p_{\mathrm{T}} > 15$ GeV. The $|\eta|$ requirement for muons is pushed down to $|\eta| < 2.5$, and electrons whose cluster are found in the crack-region, $1.37 < |\eta^{\mathrm{cluster}}| < 1.52$, are discarded. The identification criteria are tightened, as well as the isolation criteria in the case of electrons, and a lepton-to-jet overlap removal is performed, where electrons within $0.2 < \Delta R < 0.4$, and muons within $\Delta R < 0.4$, of a jet are removed. The μ-jet overlap-removal is only applied if the jet in concern has at least three tracks.

From the Z-leptons, the W-lepton collection can finally be built by tightening once again the requirements, this time requiring $p_{\mathrm{T}} > 20$ GeV and having them pass the tighter identification and isolation working point available. For electrons, only those that are unambiguously identified as prompt electrons are considered, reducing the contamination from photon-conversion background.

5.1.2 W and Z boson reconstruction

As mentioned in Section 5.1.1, the final states of interest contain three leptons and a neutrino, coming from the decay of a W and a Z boson. For this reason, only events with exactly three leptons passing the Z-lepton selection are considered. The leading-p_{T} lepton is required to have $p_{\mathrm{T}} > 25(27)$ GeV for 2015 (2016-2018) events, in order to insure it was the lepton the event was triggered with.

Two same-flavour, opposite-charge leptons are then associated to form the Z-boson candidate. In case more than one such pair can be formed, the one with the invariant mass $m_{\ell\ell}$ closest to the pole Z-boson mass, $m_Z = 91.1875$ GeV [97], is chosen. Finally, the Z-boson candidate is required to satisfy $|m_{\ell\ell} - m_Z| < 10$ GeV.

The W boson reconstruction starts from the remaining lepton, which is required to pass the

W-lepton selection. The associated neutrino is reconstructed from the event's $E_{\mathrm{T}}^{\mathrm{miss}}$, assuming that all of it can be associated to the W-boson decay. As the neutrino longitudinal energy component cannot be directly measured, it is estimated by assuming that the reconstructed W-boson mass is equal to its pole mass $m_W = 80.4$ GeV. From this assumption, the W invariant mass $m_W = \sqrt{E_W^2 - \vec{p}_W \cdot \vec{p}_W}$ can be rewritten as a quadratic equation with the neutrino longitudinal momentum p_l^ν as the only unknown:

$$C_2\ p_l^{\nu\,2} + C_1\ p_l^\nu + C_0 = 0, \tag{5.1}$$

with

$$\begin{aligned} C_0 &= -(p_x^{\ell_W} p_x^\nu + p_y^{\ell_W} p_y^\nu + \frac{m_W}{2}) + E_{\ell_W}^2 p_{\mathrm{T}}^{\nu\,2}, \\ C_1 &= -2p_z^{\ell_W}(p_x^{\ell_W} p_x^\nu + p_y^{\ell_W} p_y^\nu + \frac{m_W}{2}), \\ C_2 &= p_{\mathrm{T}}^{\ell_W}. \end{aligned} \tag{5.2}$$

Solving this equation generally does not directly yield a single, well defined value for p_l^ν. Two ambiguous cases appear. In case there are two real solutions, the choice is made to select the lower p_l^ν, and in case there are two complex solutions, their common real part is used as the p_l^ν estimate. These choices are arbitrary, as there is no proper way to solve the ambiguity. Alternative methods were tested, with no clear improvement seen on neither p_l^ν, nor on m_W resolutions.

The W-lepton and neutrino are associated to form the W boson candidate. Due to the ambiguity regarding the longitudinal energy component of the W, it makes no sense to apply a W pole mass window cut, as done for the Z boson reconstruction. Instead, the W boson is required to have a transverse mass $m_{\mathrm{T}}^W > 30$ GeV, which is defined as

$$m_{\mathrm{T}}^W = \sqrt{2p_{\mathrm{T}}^\ell E_{\mathrm{T}}^{\mathrm{miss}}(1 - \cos\Delta\phi)}, \tag{5.3}$$

where $\Delta\phi$ is the azimuthal angle between the lepton momentum and $E_{\mathrm{T}}^{\mathrm{miss}}$ directions.

5.1.3 Targeting VBS topology through jet selection

The VBS processes, and more generally the $WZjj$-EW production, is in large part identifiable thanks to the kinematic properties of the two jets in the event, making the selection of these objects of critical importance for the analysis sensitivity. They are the main tools to separate the EW and QCD production of the targeted final state, as the two jets from $WZjj$-EW events are expected to be produced back-to-back, at larger rapidities, and to be more energetic.

The analysis uses EMTopo jets. In order to enhance the $WZjj$-EW purity in the event selection, as a first step, only events with at least two reconstructed jets are considered. Jets from these events are required to have $p_{\mathrm{T}} > 25$ GeV, and $|\eta| < 4.5$. For the 36 fb^{-1} analysis, jets within $|\eta| < 2.4$, and with $p_{\mathrm{T}} < 60$ GeV are required to pass the Medium JVT working point, as defined in Section 4.2. The full Run 2 analysis also requires the Medium JVT working point for PFlow jets to be passed, in the extended range of $|\eta| < 2.5$ and $p_T < 120$ GeV.

The leading-p_{T} jet is then identified as the first tagging jet, and is required to satisfy $p_{\mathrm{T}}^{j1} > 40$ GeV. The second tagging jet $j2$ can be selected as the highest-p_T jet, that satisfies $\eta_{j1} \cdot \eta_{j2} < 0$ and $p_{\mathrm{T}}^{j2} > 40$ GeV. The p_{T} requirement is optimised in order to get the best trade-off between the $WZjj$-EW signal selection purity and significance, considering also the impact of jet-related systematics uncertainties on the latter quantity. The optimisation process is illustrated in Figure 5.1. The top plot shows an estimate of the statistical significance that can be obtained, comparing the $WZjj$-EW signal to the backgrounds described later-on in Section 5.2.1, as the cut on the p_{T} of the second tagging jet is varied. One can see that the maximum significance is indeed obtained when selecting jets with $p_{\mathrm{T}}^{j2} > 40$ GeV. On the lower plot, the relative impact of the main jet-related systematic uncertainties is measured, for a similar range of possible cuts. While the $p_{\mathrm{T}}^{j2} > 40$ GeV cut does not provide the maximal reduction of these systematics, it still provides a non-negligible reduction with respect to the $p_{\mathrm{T}}^{j2} > 25$ GeV cut applied in the previous steps of the jet selection, and further cut on the jet p_{T} would lead to a lowered overall sensitivity.

A cut is finally applied on the invariant mass of the two tagging jets, $m_{jj} > 150$ GeV, which can be defined as

$$\begin{aligned} m_{jj} &= \sqrt{(E_{j1} + E_{j2})^2 - (\vec{p}_{j1} + \vec{p}_{j2})^2} \\ &= \sqrt{2p_{\mathrm{T}}^{j1} p_{\mathrm{T}}^{j1} (\cosh\Delta\eta(j1, j2) - \cos\Delta\phi(j1, j2))}, \end{aligned} \tag{5.4}$$

assuming massless jets. This requirement is performed in order to reduce the contamination from triboson (VVV) events where one of the boson decays hadronically, with a dijet invariant mass close to the W or Z peak, as discussed in Section 1.4.1.

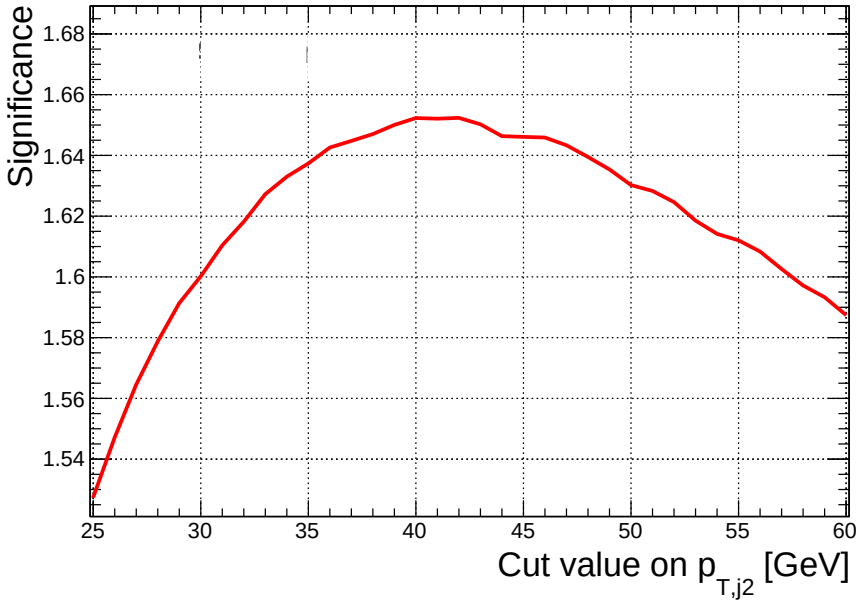

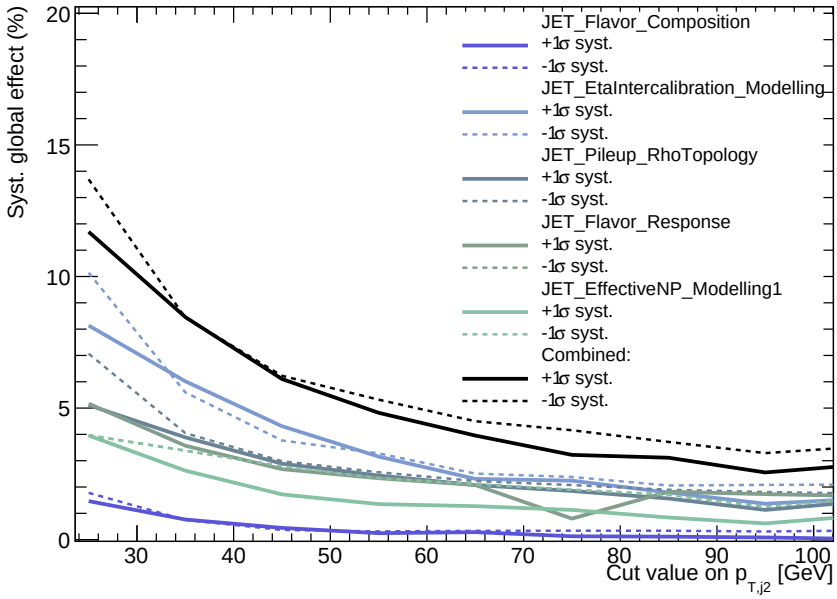

Figure 5.1: Top: $\frac{S}{\sqrt{S+B}}$ for the $WZjj$-EW signal as a function of the second tagging jet selection cut on p_{T}. Bottom: Relative impact of the main jet-related uncertainties as a function of the second tagging jet selection cut on p_{T}. The JET_Flavor_Composition and JET_Flavor_Response correspond to uncertainties on the quark/gluon nature of the jet, and their impact on the JES and energy response. The JET_EtaIntercalibration_Modelling translates the model dependance of the uncertainties extrapolation to large-η jets, and the JET_Pileup_RhoTopology represents the impact of the underlying event uncertainties on the calibration. Finally, the JET_EffectiveNP_Modelling1 is the principal component of the combined modelling-related uncertainties on the JES, following the combination scheme described in Ref. [98].

5.2 Analysis methodology

5.2.1 Background estimation

The main background to the $WZjj$-EW analysis is, as previously mentioned, the $WZjj$-QCD production. Nevertheless, some other processes can, to a lesser extent, contaminate the event selection. These can be split into two categories. The first category is the irreducible background processes. These are processes that produce a similar final state to $WZjj$-EW, with correctly identified leptons and jets, and only differ from it kinematically. Such background processes include:

- the $WZjj$-QCD production
- the tZj production, where the top quark decays into a W boson and a b-jet
- the $ZZjj$ production, where one of the final state leptons does not pass the full reconstruction process and kinematic selection
- the $t\bar{t}+V$ $(V = W, Z)$ production
- the VVV production, where one of the bosons decays hadronically

These background contributions are estimated using MC events. The list and main characteristics of the MC generators used to simulate them is found in Table 5.2.1. The largest irreducible backgrounds are $WZjj$-QCD, $t\bar{t}+V$ and ZZ.

These are constrained with data in dedicated control regions simultaneously to the $WZjj$-EW cross-section extraction fits described in Section 5.2.3.

The ZZ control region (ZZ-CR) is defined by mimicking the VBS selection, but requiring exactly four leptons passing the baseline lepton selection instead of three, in addition to the two tagging jets requirement. The VBS selection is divided into two control regions and a signal region, as shown schematically in Figure 5.2. In order to define the control region for $t\bar{t}+V$ (b-CR), jets in the events are tagged as either b-jets or light-jets using the standard flavour tagging tool, MV2C10 [99]: a BDT-based multivariate discriminant optimised to identify jet flavours, using the characteristic properties of b-hadron decays. The choice is made to use the b-jet identification working point corresponding to a 70% identification efficiency, corresponding to rejection rates of about 99.6 % for light-flavour jets and about 90 % for c-jets. This working point is chosen as a trade-off between a good identification of b-jets, and correspondingly $t\bar{t}+V$ events, and a low rate of mis-tagged jets from actual $WZjj$-EW signal events. Events containing at least one b-tagged jet are used to define the b-CR.

Table 5.3: List of MC generators used to simulate the processes of interest for the $WZjj$-EW analysis. For each process, the ME and hadronisation MC generators, and PDF set are given, as well as the computation order used.

Process	Generator (PDF)	Order (α_s)
$WZjj$-EW	SHERPA2.2.2 (NNPDF3.0nnlo)	LO
	MADGRAPH5+PYTHIA8 (NNPDF3.0nlo)	LO
$WZjj$-QCD	SHERPA2.2.1 (NNPDF3.0nnlo)	(0,1)jNLO + (2,3)jLO
	SHERPA2.2.2 (NNPDF3.0nnlo)	(0,1)jNLO + (2,3)jLO
	SHERPA2.1 (NNPDF3.0nnlo)	(0,1)jNLO + (2,3)jLO
	MADGRAPH5+PYTHIA8 (NNPDF3.0nlo)	(0,1,2)jLO
tZj	MADGRAPH5+PYTHIA8 (NNPDF3.0nlo)	LO
$ZZjj$-QCD	SHERPA2.2.2 (NNPDF3.0nnlo)	(0,1)jNLO + (2,3)jLO
$ZZjj$-EW	SHERPA2.2.2 (NNPDF3.0nnlo)	LO
$t\bar{t}+V$	MADGRAPH5+PYTHIA8 (NNPDF3.0nlo)	NLO
VVV	SHERPA2.2.1 (CT10)	LO
Z+jets	POWHEG+PYTHIA8 (NNPDF3.0nnlo)	NLO
$t\bar{t}$	POWHEG+PYTHIA8 (NNPDF3.0nlo)	NLO
$Z\gamma$	SHERPA2.2.2 (NNPDF3.0nnlo)	NLO

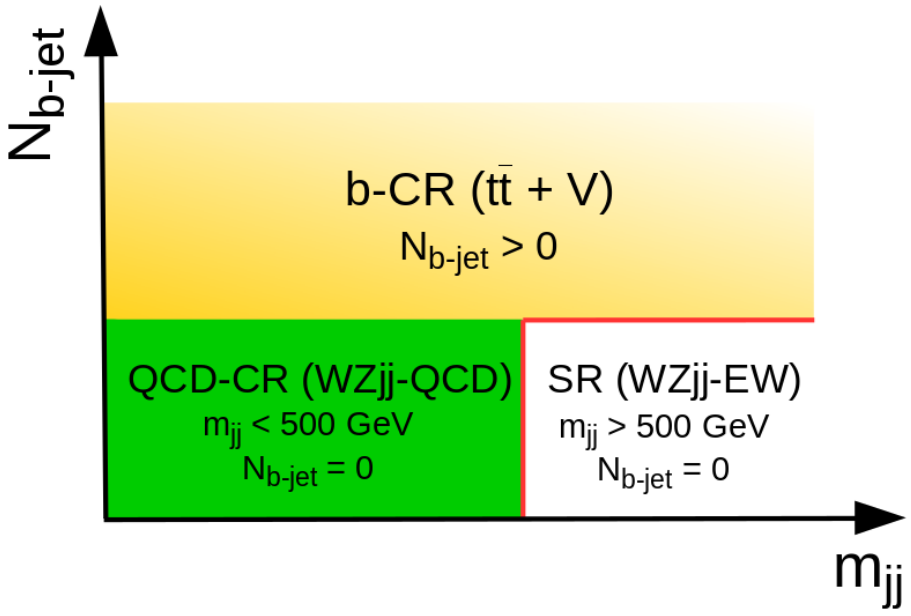

Figure 5.2: Schematic view of the signal and control regions definition inside of the VBS selection.

Lastly, events with no b-jets passing the $WZjj$ event selection are split into two categories according to the invariant mass of the tagging jet pair. The lower mass region, defined with $150 < m_{jj} < 500$ GeV, is used to constrain the $WZjj$-QCD background, and is referred to as QCD-CR, while the high-mass region, with $m_{jj} \geq 500$ GeV, defines the signal region (SR) in which the $WZjj - EW$ cross-section is measured.

Data is used in the different control regions in order to verify the modelling of the main background processes by the MC simulations used. However, the SR was kept blind during the whole optimisation process of the analysis. The analysis strategy was defined only based on MC expectation in the SR, and was not changed after the unblinding of data in the SR.

The second category is that of the reducible backgrounds, entering the selection due to misidentified (fake) leptons. These are mostly composed of Z+jets, where a jet is misidentified as an electron; $Z\gamma$ events, with the photon being misidentified as an electron, and $t\bar{t}$ events where a lepton coming from one of the b-hadron decays is associated to one of the two W boson leptons to form a fake Z boson. $W\gamma$ events are also accounted for, but their contribution is found to be negligible, and is merged with that of the $Z\gamma$ events. The reducible background contribution to the event selection is estimated through a data-driven method referred to as the Matrix Method, following the same methodology optimised for the inclusive WZ analysis [46]. A total of eight identification categories is defined, each representing a possible combination of three Loose (L) or Tight (T) leptons, where Tight leptons are leptons passing the W- or Z-lepton selection, while Loose leptons are leptons failing one of the identification criteria. Eight truth-level categories are defined in a similar way, with prompt leptons categorised as Real leptons (R), and non-prompt leptons as Fake leptons (F). The yields measured in each of the eight identification categories can be related to that of the truth-level categories through an 8×8 matrix, whose elements represent the probability for an event to belong to each combination of truth-level and identification categories. The number of events with at least one fake lepton in the analysis selection is then estimated by inverting this matrix.

A MC based fake background estimation method is also used, in order to validate the Matrix-Method estimate.This method, referred to as the Fake Scale Factor method, uses control regions in which scale factors are extracted to correct the MC predictions for the various fake background sources. A set of dedicated control regions is defined for each of the considered signal-faking processes, Z+jets, $t\bar{t}$ and $Z\gamma$, as well as for both electron-faking and muon-faking fakes and separately for W-leptons and Z-leptons. This yields a total of 10 distinct scale factors, that are applied to each truth-matched fake lepton in the analysis region for the samples concerned.

The two methods yield overall very comparable results, with differences typically well within the uncertainty associated to the Matrix method estimate, fixed to 40 %.

The signal and background event yields obtained in the different regions are shown in Table 5.4 for the 36 fb^{-1} analysis. SHERPA 2.2.2 is used as the nominal MC generator for the simulation of both the $WZjj$-EW and $WZjj$-QCD production.

From this table, one can see the event yields are largely overestimated compared to the observed data in most regions. This is thought to be due in large part to known modelling issues coming with the specific versions of SHERPA used for the analysis, that overestimate the $WZjj$-QCD cross-section. Though the issue is known, no other generator was available with enough statistics to be used as the nominal at the time of the study, but extra care was given to the estimation and control of the $WZjj$ modelling, through the design of the signal extraction fit described in Section 5.2.3 and the modelling-related systematic uncertainties estimation strategy described in Section 5.2.4.

Table 5.4: Expected and observed numbers of events in the signal region and in the three control regions for the 36 fb^{-1} analysis. The expected number of $WZjj$-EW events from SHERPA and the estimated number of background events from the other processes are shown. The sum of the reducible background contributions is labelled 'Misid. leptons'. The total uncertainties, as described in Section 5.2.4, are quoted.

	SR	QCD CR	b-CR	ZZ-CR
Data	161	213	141	52
Total predicted	200 ± 41	290 ± 61	160 ± 14	45.2± 7.5
$WZjj$-EW (SHERPA)	24.9± 1.4	8.45±0.37	1.36±0.10	0.21±0.12
$WZjj$-QCD (SHERPA)	144 ± 41	231 ± 60	24.4± 1.7	1.43±0.22
Misid. leptons	9.8 ± 3.9	17.7± 7.1	30 ± 12	0.47±0.21
$ZZjj$-QCD	8.1 ± 2.2	15.0± 3.9	1.96±0.49	35 ± 11
tZj	6.5 ± 1.2	6.6 ± 1.1	36.2± 5.7	0.18±0.04
$t\bar{t}+V$	4.21±0.76	9.11±1.40	65.4±10.3	2.8 ±0.61
$ZZjj$-EW	1.80±0.45	0.53±0.14	0.12±0.09	4.1 ± 1.4
VVV	0.59±0.15	0.93±0.23	0.13±0.03	1.05±0.30

5.2.2 Multivariate analysis for background discrimination

The main challenge of the $WZjj$-EW analysis is to identify the - rather small - electroweak signal from the much more important QCD production of the final state. The most straightforward method to do so is the so-called cut-based approach. It consists in identifying the variables providing most discrimination between the two processes, and apply simple cuts on them in order to maximize the process significance in a, potentially very localized, kinematic

region. Such a method was employed for the 8 TeV ATLAS result on the study of the fully leptonic $WZjj$-EW final state [5], and more recently by the CMS collaboration for their 36 fb^{-1} result on the same final state [64]. The strategy used in the ATLAS results was simply to define a tight enough phase space, similar to the one from the present analysis, in which limits on the cross-section were extracted through a single-bin likelihood fit. CMS used a similar strategy, replacing the single-bin fit by a two-dimensional template fit on $m_{jj} \times \Delta\eta_{jj}$. In both cases, the dimensionality remains low, and potentially relevant information on the process kinematics is surely not used.

For that reason, the choice is made to use a multivariate approach instead. In this approach, a BDT is trained in order to isolate as much as possible the $WZjj$-EW signal. The training is performed using ROOT's TMVA package [85]. Only events from the $WZjj$-EW SR are considered, with all the irreducible background sources combined into a single background category. The choice is made to include all irreducible backgrounds, in order to maximise the overall separation $WZjj$-EW and all the backgrounds, as opposed to the $WZjj$-QCD background only. Nevertheless, the actual gain in sensitivity coming from this choice is found to be negligible. A list of 15 kinematic and topological variables, selected among a much larger pool of potentially interesting variables, is used as input to the BDT. Seven of these variables describe the properties of the tagging jets. These are m_{jj}, the jet multiplicity $\mathrm{N}_{\mathrm{jets}}$, $p_{\mathrm{T}}^{j1,j2}$, η_{j1}, and the difference in pseudorapidity, $\Delta\eta_{jj}$, and in azimuthal angle, $\Delta\phi_{jj}$, between the two tagging jets. Although the $VVjj$-EW processes are typically known to be identifiable through their tagging jet's kinematics, some discriminating features can also be found in the properties of the leptonic system. For that reason, four variables purely related to the W and Z boson kinematics are also included: the rapidity separation between the W lepton and the Z boson $|y_{\ell,W} - y_Z|$, $p_{\mathrm{T}}^{W,Z}$, η_W and m_{T}^{WZ}. Finally, three variables combining information from the jets and bosons are included. These are the angular separation between the first tagging jet and the Z boson $\Delta R(j1, Z)$, following the definition from Section 2.3.1, $R_{p_{\mathrm{T}}}^{\mathrm{hard}}$, defined as the transverse component of the vectorial sum of the momenta of the event's hard final state objects (leptons and jets), divided by the sum of their transverse momenta, and the lepton centrality with respect to the dijet system ζ_{lep}, defined in Equation 1.18 from Section 1.4.1.

The distributions of these 15 variables are compared between the $WZjj$-EW signal and the irreducible backgrounds in Figure 5.3. Some of these variables show no clear separation between the signal and backgrounds. Nevertheless, these still carry some useful information through their correlations, that are used throughout the discriminant optimisation. This is verified through a ranking of the inputs variables, following the method described in Section 4.4. Among the input variables, the less impacting one for the BDT training is found to be η_{j1},

though removing it yields a drop in performance, evaluated in terms of impact on the classifier AUC, of about 0.9%. The modelling of these variables has been thoroughly checked along the development of the analysis.

The modelling was checked in the QCD CR before the SR unblinding. It was found to be good there in terms of the shape description of the distributions. The same assessment is made later on in the signal region, and the corresponding distributions are shown in Figure 5.4. Some variables displayed some discrepancies between the data and MC distributions, but it is verified that the final BDT score distributions shows a very good agreement in the QCD CR.

Additionally, the modelling of the correlations between the fifteen inputs is checked. This is typically done by comparing the correlation matrices obtained with data and MC, but as the number of events in the VBS selection is relatively low, the correlation coefficients obtained from data fluctuate too much to be used for this purpose. Instead the choice is made to decompose the correlation coefficients in order to obtain one-dimensional distributions, for which the data-to-MC agreement can be assessed through a χ^2-test. These decomposed correlation coefficients are computed as

$$r(x_i, x_j) = \frac{(x_i - \langle x_i \rangle)(x_j - \langle x_j \rangle)}{\sigma_i \sigma_j}, \tag{5.5}$$

with $x_{i,j}$ being the value of variable i or j for a given event, and $\sigma_k = \sqrt{\frac{1}{N}\sum_{x=1}^{N}(x_k - \langle x_k \rangle)^2}$ being the standard deviation of this variable. Two of the resulting distributions are illustrated in Figure 5.5. Only the correlations between the lepton centrality ζ_{lep} and m_{jj}, and p_T^{j2} and $\Delta\eta(j1, j2)$ are shown here for illustration purpose, but a good data-to-MC agreement is found for all the other combinations of the BDT inputs.

Many other inputs were considered, and most of them were found not to bring any improvement, or even to worsen the performance. Some other variables considered were found to bring improvement, but were discarded for physics-related reasons. This last point especially concerns variables related to the kinematics of a potential third central jet. As the $WZjj$-EW production is expected to have a suppressed hadronic activity between the two tagging jets, such variables are excellent candidate variables for the $WZjj$-QCD discrimination. Nevertheless, it is found that most of the discriminating power of these variables arose from the separation from events reconstructed with exactly two jets. Additionally, the additional jet activity is suspected to be poorly modelled, and the potential benefits from using related kinematic variables are expected to be largely dampened by the increased uncertainty on the MC modelling.

The proper training of a BDT, or any multivariate algorithm, relies on many parameters

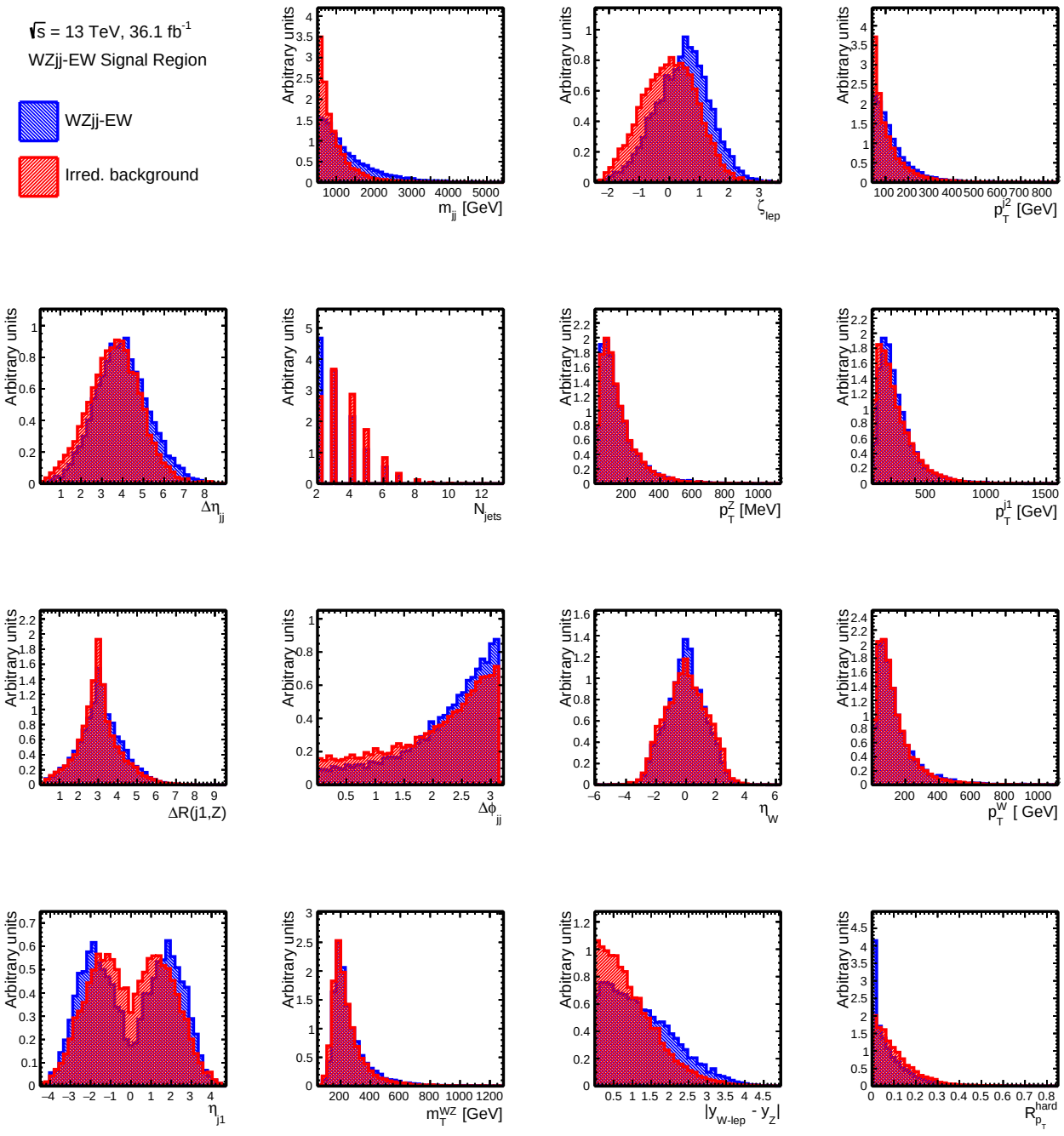

Figure 5.3: Comparative distribution, normalised to the same area, between the $WZjj$-EW signal and the irreducible backgrounds, for the 15 input variables to the BDT training in the SR.

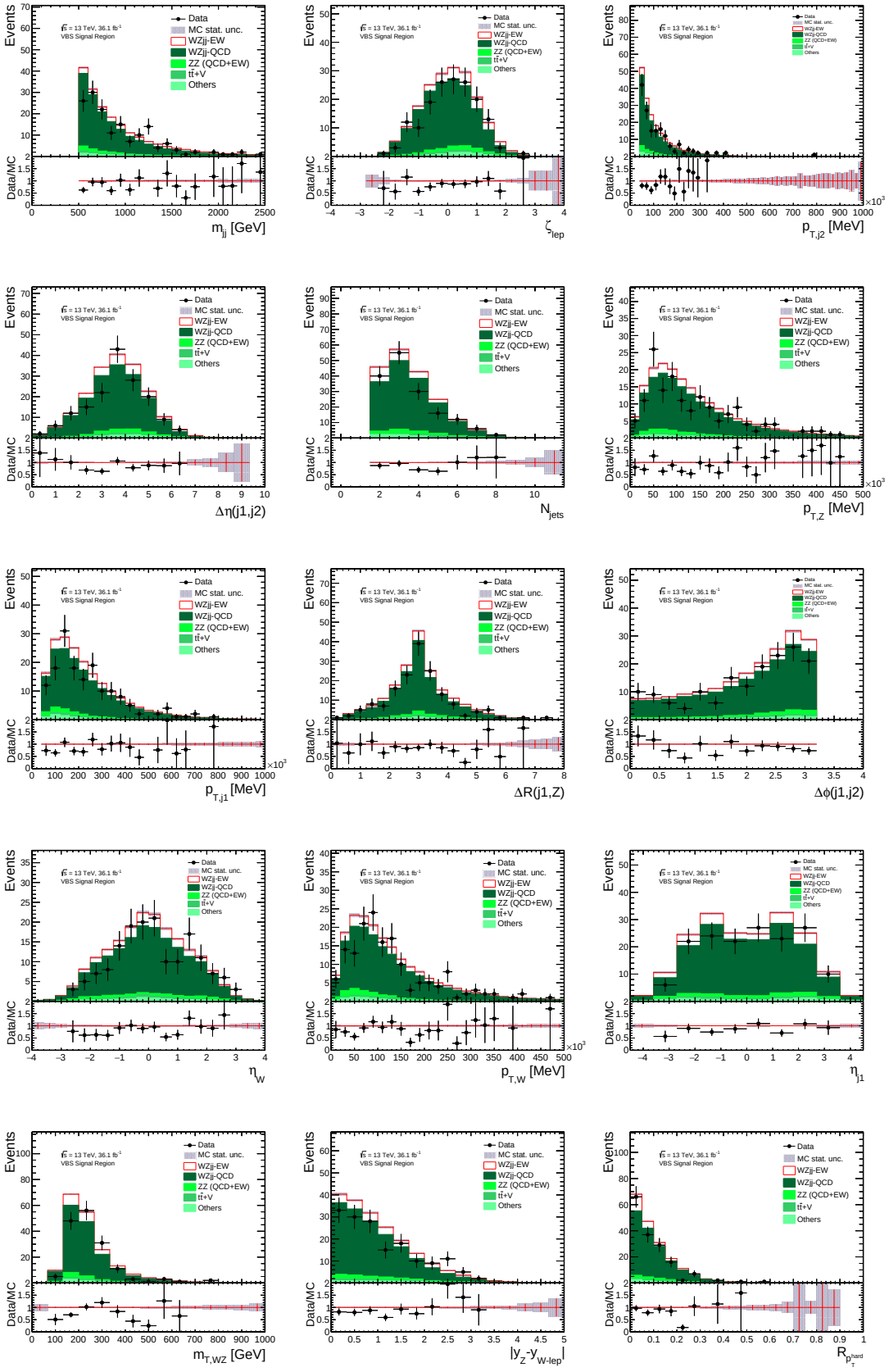

Figure 5.4: Control distributions of the BDT inputs in the Signal region. No correction of the MC distributions normalisations is applied.

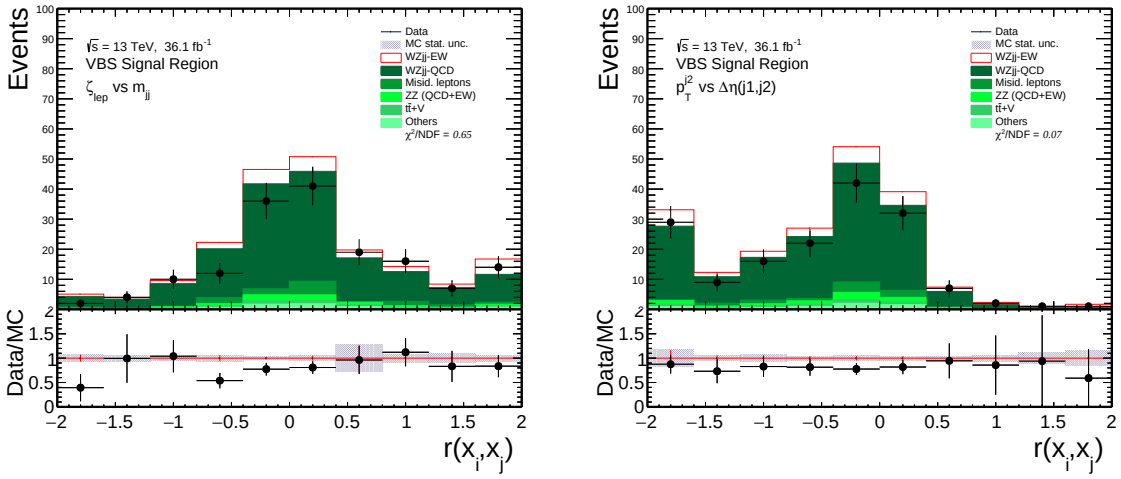

Figure 5.5: Decomposition of the correlation coefficients between ζ_{lep} and m_{jj} (left), and p_T^{j2} and $\Delta\eta(j1, j2)$ (right).

complementing a good choice of input variables. Among these, the available statistics for both the training and validation of the method is of critical importance. In order to optimise the usage of the available statistics, a method called 2-fold cross-training is employed. It consists in splitting the samples into two equal size sub-samples. In a first training, the first half of the sample is used as the training sample, while the second one serves as a validation sample. A second training is then performed, this time inverting the training and validation samples. The two outputs are then merged into a single one, that can be used as the final discriminant. The separation is performed according to the event number, ensuring that the two sub-samples are fully decorrelated, and of similar constitution. This separation is also applied to the data sample, and to the MC samples that are not used in the training process. This method has the advantage of allowing for the use of the full available MC statistics for the classifier training, while avoiding any overlaps between the training and validation MC samples that could bias the performance estimate.

To maximise the effective statistics further, two generations of the $WZjj$-QCD samples, generated using Sherpa 2.2.1 and Sherpa 2.2.2 respectively, are combined. The modelling of these two samples was checked to be in agreement with each other.

Another aspect of multivariate method optimisation is a proper choice of the structural characteristics of the algorithm, referred to as hyper-parameters. One of the advantage of BDTs compared to most other multivariate algorithms is the relative robustness of their performance and stability with respect to the hyper-parameters. This is verified in the present study,

as a number of combinations of hyper-parameters are tested, but no large variations of the performance is observed.

The distributions of the BDT output for $WZjj$-EW MC events is compared to that of the sum of irreducible background events in Figure 5.6. The excellent separation can be noted

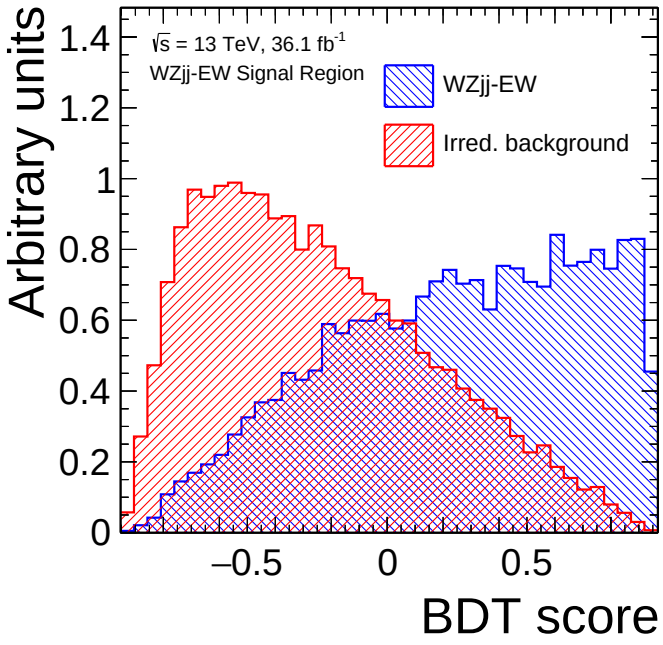

Figure 5.6: Distributions of the BDT output for the $WZjj$-EW signal, and for the sum of irreducible backgrounds.

by looking at the distributions. This is confirmed by comparing the performance with the single most discriminating input, ζ_{lep}. The comparison is shown in Figure 5.7, where the BDT output is shown to provide a 23% improvement in terms of the ROC AUC with respect to ζ_ℓ. Distributions of the BDT output in the QCD-CR and in the SR are shown in Figure 5.8. A rather large discrepancy between data and MC is observed in both regions, and appears to be most significant at lower values of the BDT score, where the $WZjj$-QCD contribution is dominant. Looking at the QCD-CR distribution, the discrepancy is roughly constant, with an apparent excess of MC events of about 20%. It is attributed to the misprediction of the $WZjj$-QCD production cross-section by Sherpa, and is corrected before proceeding to the signal-extraction fit, as described in Section 5.2.3.

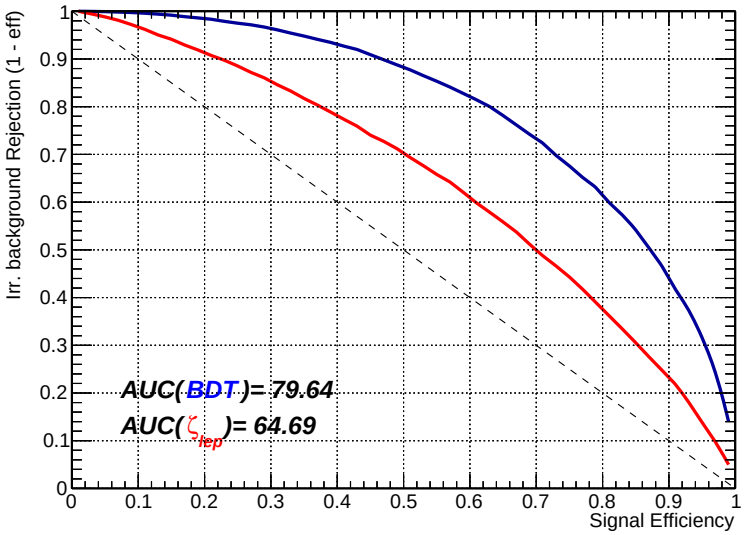

Figure 5.7: ROC curves illustrating the separation performance of the BDT score, and of the lepton centrality ζ_{lep}. The Area Under the Curve (AUC) is given in percent.

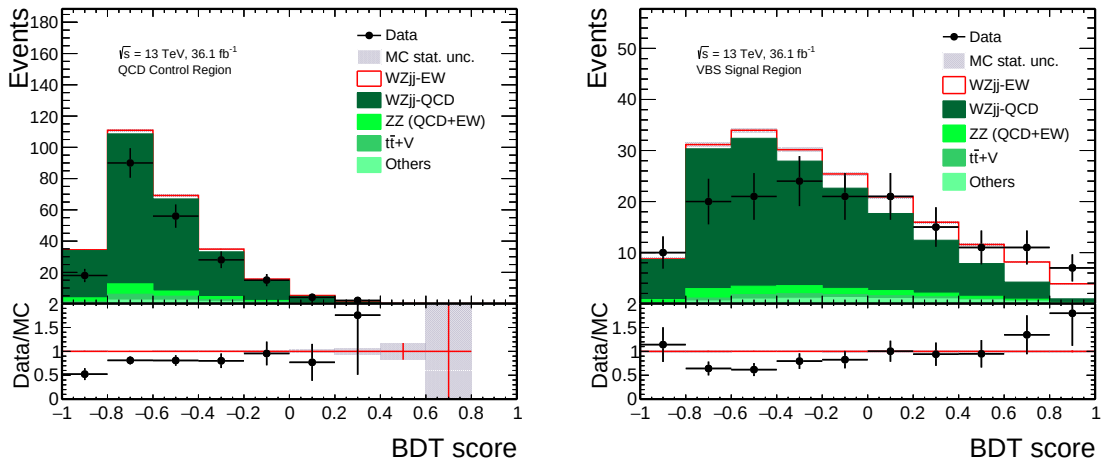

Figure 5.8: Distributions of the BDT score in the QCD-CR (left) and in the SR (right).

5.2.3 Statistical analysis for signal extraction

The powerful discrimination of the BDT score can be used in several ways. The most straightforward approach would be to apply a cut on the BDT score, in order to define a region with an optimal signal purity. Such region could then be used in a fit similar to the one of ATLAS 8 TeV analysis [5] mentioned earlier. Although this approach is valid from a technical point of view, the fiducial phase-space would be very complex, involving in its definition a non-linear combination of the BDT inputs. Another possibility is to use the full shape of the BDT distribution and extract the $WZjj$-EW cross section using a binned template fit to data. With this approach, the measured cross section therefore corresponds to the well defined SR, and benefits from the full available event statistics in this region. The complete setup for the statistical analysis is based on the use and proper definition of such template fits, and is developed mostly based on the HistFactory tool [100].

The complete VBS selection is used in the fitting procedure, although it is designed in such a way that the measured cross-section, and the associated significance are only extracted in the SR. The three control regions, QCD-CR, b-CR and ZZ-CR, are included, in order to provide additional constraint on the uncertainties on the background contributions.

In order to correct for the discrepancies of event yields between data and MC that are seen in the control regions, especially in the QCD-CR, where 36 % more events are predicted by the MC simulation compared to the number of events observed in data, a preliminary fit, referred to as background-only fit, is performed using only the three control regions, in order to extract a correction factor for the normalisation of the dominant background in each region. Correcting for this difference is therefore expected to yield a more accurate estimation of the expected sensitivity to the $WZjj$-EW signal in the SR. This correction only affects the expected results. It is verified that, after the unblinding, the same observed result is obtained using a single-step fit of all regions together, without correcting the normalisation of background MC simulations.

Although the CR are mainly used to correct normalisations, the choice is made to use binned kinematic distributions. In the QCD-CR, the m_{jj} distribution is used as a template, in order to get more reliable extrapolations of the modelling uncertainty constraints into the signal region. For the b-CR, the b-jet multiplicity N_{b-jet} is used, in order to provide a good separation between the $t\bar{t}+V$ background being constrained, and the $tZ+j$ background that has a non-negligible contribution to the total b-CR yield of about 23%, but in which only one b-jet is typically observed. In the ZZ-CR, m_{jj} is also used, but no real change is seen from using a single bin, due to the excellent purity and overall good data-to-MC shape agreement in the region. The template distributions in the three CRs are shown in Figure 5.9. The binning

of the distributions is optimised in order to get the best trade-off between the sensitivity to kinematic trends, and the reduction of statistical fluctuations that could bias the fit. In the case of N_{b-jet} in the b-CR, a merging of the $N_{b-jet} \geq 2$ bins was considered, yielding no difference in the results, so the distribution is used as is.

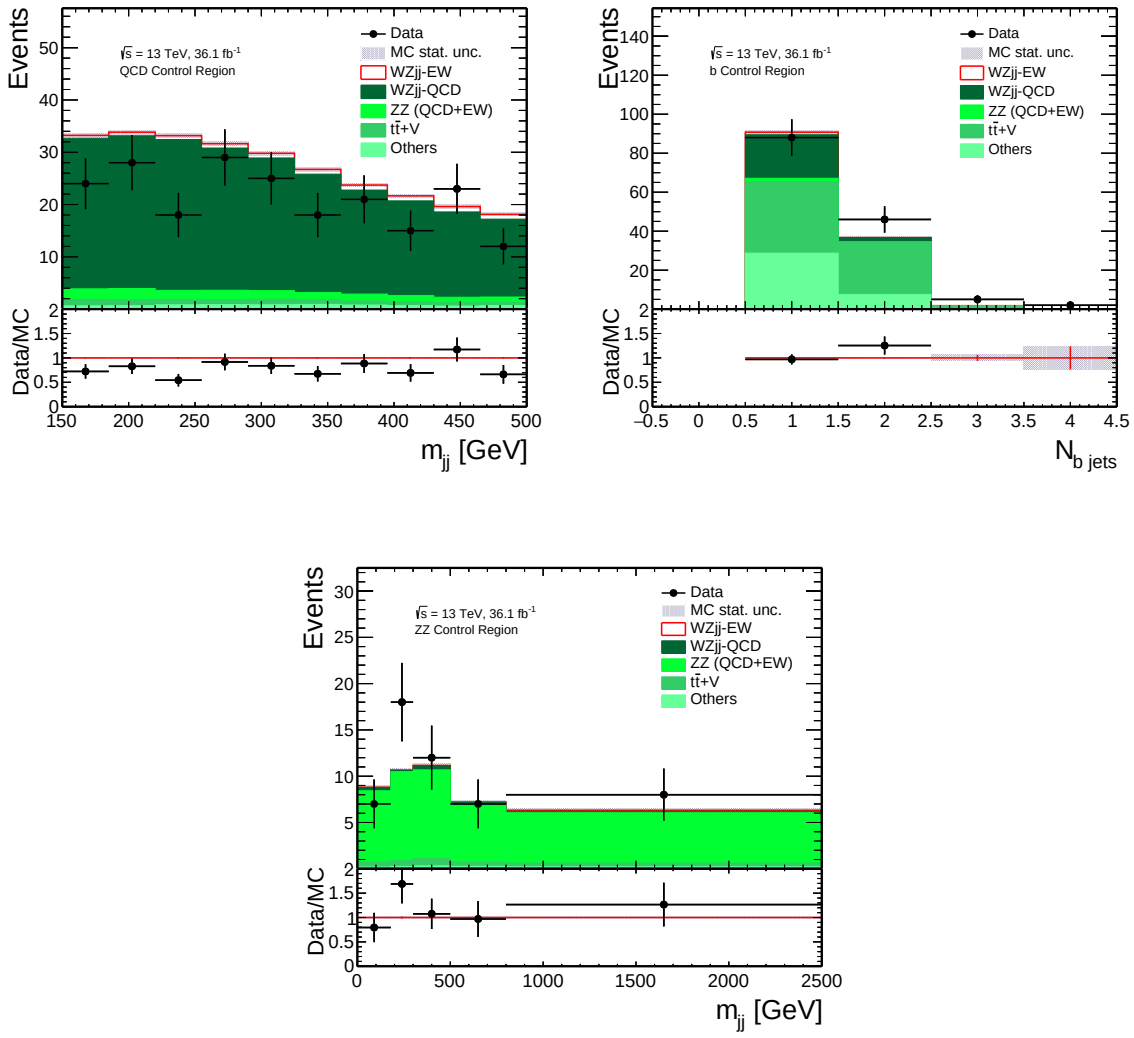

Figure 5.9: Distribution of the template variables, m_{jj} in the QCD-CR (top-left), N_{b-jet} in the b-CR (top-right) and m_{jj} in the ZZ-CR (bottom), as used in the background-only fit.

All the relevant uncertainties, as detailed in Section 5.2.4, are included, and properly correlated between the different samples and regions. Nevertheless, the constraints provided by the fit on these are not directly propagated to the final measurement, and are only implemented in order to get a more robust estimation of the required correction factors. Following

the background-only fit, the normalisation correction factors are applied to the relevant backgrounds, $WZjj$-QCD, $t\bar{t}+V$ and ZZ-QCD in the three CR as well as in the SR.

A combined fit is then performed including the four regions, later on referred to as the signal-extraction fit. The same templates as for the background-only fit are used in the three CR. In the SR, the BDT score is used, as displayed in Figure 5.8 from the previous section. Although the background predictions are corrected from the background-only fit, the three background-normalisation parameters are again included, this time correlated between the CR and SR, in order to account for potential SR-specific behaviour that was not previously accounted for in the backgrounds constraints, ensuring their validity over the full fitted selection.

Both the background-only fit and signal fit are designed in a similar way. These are likelihood fits, aiming at minimising the so-called negative log-likelihood ratio NLL(λ). The variable λ can be defined as a function of free-floating signal strength parameters, noted as μ, representing the correction factors on the sample normalisations, as well as nuisance parameters (NP) θ representing the impact of systematic variations on the measurement, that typically follow a Gaussian constraint. It can be written, in a compact form, as

$$\mathrm{NLL}(\lambda(\mu,\hat{\mu},\hat{\theta},\hat{\hat{\theta}})) = -\ln\frac{\mathcal{L}(\mu,\hat{\hat{\theta}})}{\mathcal{L}(\hat{\mu},\hat{\theta})}. \tag{5.6}$$

In this expression, $(\hat{\mu},\hat{\theta})$ is the parameter combination yielding the overall maximal value of the likelihood function $\mathcal{L}$, while $\hat{\hat{\theta}}$ is the combination of NP values that maximises $\mathcal{L}$ for a given value of μ. The natural logarithm and minus sign are used to facilitate the interpretability, creating a function whose minimum is forced to be equal to 0, and satisfying

$$\mathrm{NLL}(\lambda(\mu=0)) = \frac{Z^2}{2}, \tag{5.7}$$

with Z being the statistical significance, in terms of Gaussian standard deviations, of the best-fit estimate of the parameter of interest μ. For the background-only fit, three μ parameters are fitted simultaneously, noted later on as $\mu_{WZjj\text{-QCD}}$, $\mu_{t\bar{t}+V}$ and μ_{ZZ}. The same three parameters are defined for the signal fit, in addition to the parameter of interest $\mu_{WZjj\text{-EW}}$.

5.2.4 Estimation of systematic uncertainties

The main and most obvious single source of uncertainty for the $WZjj$-EW cross-section measurements is the statistical uncertainty, due to the rarity of the targeted process, and to the correspondingly restrictive definition of the event selection. Nevertheless, many other sources

have to be considered, and are far from being negligible. These uncertainties can be split into two main categories. The first category are the experimental systematic uncertainties, mostly, but not only, related to the reconstruction and calibration of the physics objects used in the analysis. In this category are considered:

- Jet-related uncertainties: this includes uncertainties on the JES and JER calibration, as well as uncertainties on the efficiencies of the pileup-jet and flavour-tagging tools used for the selection.
- Lepton-related uncertainties: similarly to jets, uncertainties on the energy calibration of the leptons are accounted for, as well as on the efficiencies of the quality requirement cuts (identification and isolation). This is true for both muons and electrons, although specific sets of uncertainties are defined for the two flavours separately, and have widely different impacts on the analysis.
- $E_{\mathrm{T}}^{\mathrm{miss}}$-related uncertainties: the uncertainties on the $E_{\mathrm{T}}^{\mathrm{miss}}$ reconstruction are in large part accounted for in the uncertainties of jets and leptons, as these are used in its definition. An additional source of uncertainty comes from the track soft-term, but it is found to have a negligible impact on the analysis sensitivity.
- Luminosity uncertainty: a 2.1% uncertainty is attributed to the measurement of the total integrated luminosity.
- Pileup reweighting uncertainty: this is considered to account for the intrinsic mismodelling of the pileup overlay applied to MC samples, that are generated following distributions of the number of interactions per bunch crossing which do not closely match the data, and so have to be corrected.

The second category regroups all theory-related uncertainties. These are typically more complicated to estimate, but play a critical role in the proper estimation of the analysis sensitivity. Two types of well-defined theory-related uncertainties are considered for both the $WZjj$-EW and $WZjj$-QCD production:

- QCD scale uncertainties: these are defined to account for the, somewhat arbitrary, choice of renormalisation and factorization scale. The QCD scale uncertainties are estimated by varying these two scales independently by a factor 2 or 0.5, then taking the envelope of the resulting distributions as an uncertainty band.
- PDF uncertainties: these are estimated following the method described in Ref. [28]. Two sources are accounted for separately. A first uncertainty band regarding the PDF

choice is defined as the standard deviation of the distribution of 100 MC replicas of the NNPDF 3.0 set. This uncertainty is verified to cover the variations of the distributions obtained using the MMHT2014 and CT14 sets. The second one accounts for the effect of varying the α_S from its nominal value of 0.118 to 0.117 or 0.119 used for the PDF extraction.

The impact of these uncertainties on the BDT score in the SR is shown in Figure 5.10. The QCD scale uncertainty is found to have a +30%/-20% impact on the $WZjj$-QCD process, mostly impacting its normalisation, and of up to about 5% on the $WZjj$-EW process, with a non-negligible impact on the distribution shape. The PDF uncertainties are found to have an overall smaller impact, representing a flat ∼2.5% uncertainty band for $WZjj$-EW and a slightly more shape-impacting variation of similar amplitude for $WZjj$-QCD in the case of the PDF choice uncertainty, and the α_s variation is found to only impact $WZjj$-QCD, also with a ∼2.5% flat uncertainty band.

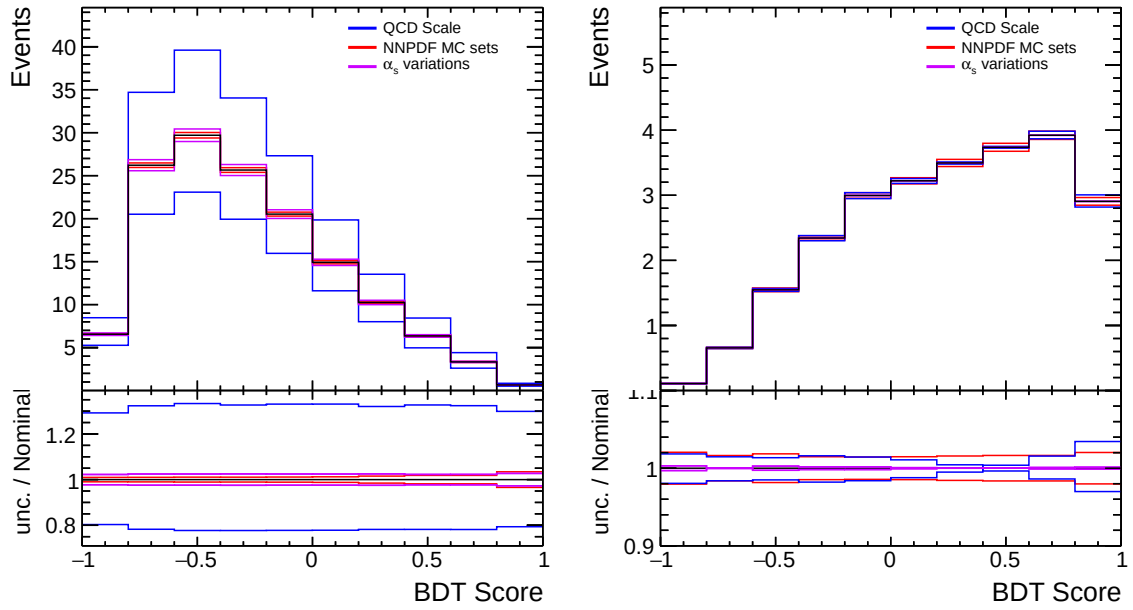

Figure 5.10: QCD scale (blue), PDF choice (red), and α_s uncertainties (purple) on the $WZjj$-QCD background (left) and $WZjj$-EW signal (right).

In addition to these two items, modelling uncertainties are defined by comparing different MC predictions. For both the $WZjj$-EW and $WZjj$-QCD predictions, a generator-level comparison is made between the nominal Sherpa2.2.2 samples and a LO MadGraph sample with up to one jet included in the matrix element, specifically generated for this purpose. In order to propagate the uncertainty to the reconstructed-level, the Sherpa2.2.2 sample is reweighted

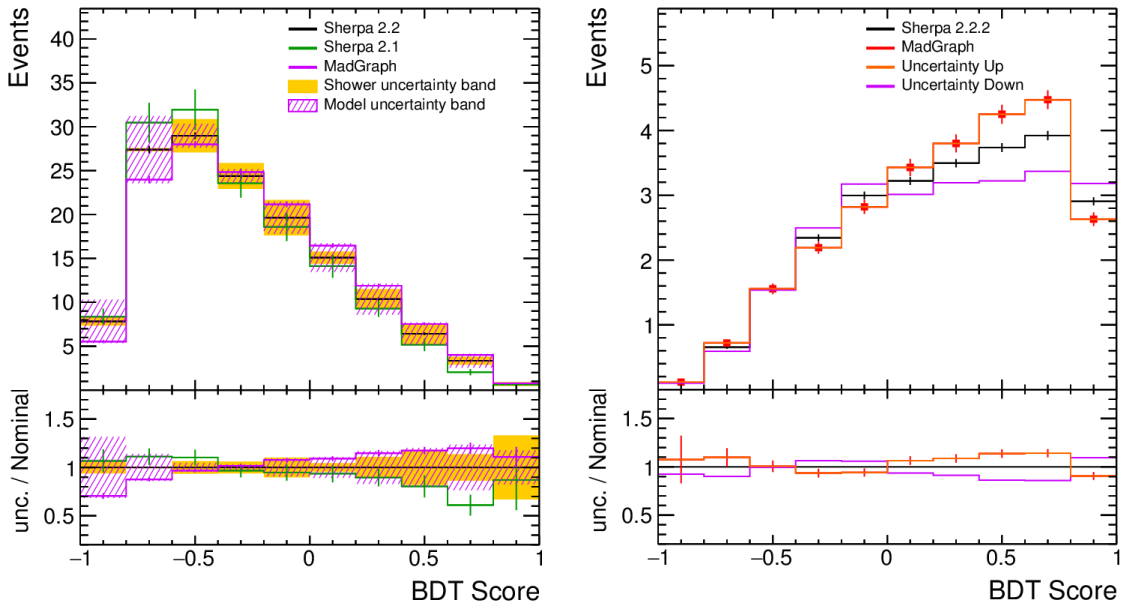

Figure 5.11: Modelling uncertainty band on the $WZjj$-QCD background (left) and $WZjj$-EW signal (right). The $WZjj$-QCD modelling uncertainty is compared to the Shower uncertainty. The corresponding BDT score distribution obtained using Sherpa 2.1 is also shown for the $WZjj$-QCD process for comparison. The error bars shows the statistical uncertainty of each sample.

at generator-level to match the prediction from the MadGraph sample with respect to the BDT score, evaluated using generator-level variables presented in Section 5.2.3. The difference between these distributions and the nominal reconstructed-level Sherpa2.2.2 predictions is then symmetrised, and used as a modelling uncertainty band, as shown in Figure 5.11.

The $WZjj$-QCD modelling uncertainty has been compared with a Parton-Shower-only uncertainty, estimated as the comparison between the template distributions generated using Powheg with either Pythia8 or Herwig7 for the parton shower. The former uncertainty band was found to cover entirely the PS difference, and to be generally more conservative. A similar comparison is made with events generated with an older version of the nominal generator, Sherpa 2.1, whose difference with the nominal $WZjj$-QCD distribution is also found to be mostly covered by the modelling uncertainty. Two bins of the Sherpa 2.1 BDT score distribution are found to lie outside the modelling uncertainty band. However, this sample suffers from relatively low statistics, which is a plausible cause for the difference.

The effect of interference between the $WZjj$-EW and $WZjj$-QCD production is also considered. Dedicated interference-only MC are generated using MadGraph, and are compared to the purely-EW, and purely-QCD predictions at generator level. These interference-only MC

are found to represent about 10% of the purely-EW, and about 4% of the purely-QCD yields. However, the differences observed in the shape of kinematics observable are also considered.

The generator-level BDT score distribution of the purely-EW MC is compared to that of the sum of the purely-EW MC and interference-only template. The ratio between the two distributions is used to reweight the detector-level $WZjj$-EW Sherpa template, in order to create the corresponding uncertainty band.

It is relevant to note that the choice to use the interference as an uncertainty on the signal shape is somewhat arbitrary, as the interference contribution is not exactly a $WZjj$-EW-only feature. From a physics point of view, this translates into the fact that the measurements performed of the $WZjj$-EW cross-section should be interpreted as including the contribution from these interferences.

Finally, concerning the modelling of the non-dominating irreducible backgrounds, normalisation uncertainties are defined following the most up-to-date estimates, or measurements when available, of their cross-sections. This translates into a 20% uncertainty on the VVV production [101], 15% for both $tZ + j$ and $t\bar{t} + V$ [102], and 25% for the ZZ production.

The technical implementation in the analysis statistical framework is done in a similar way for both the experimental and theory-related uncertainties. Each independent uncertainty source is implemented in the fit as a ± 1 σ variation band around the nominal template histograms it is considered for. For the experimental uncertainties, however, the very large number of independent systematics sources is reduced through a pruning procedure, aiming at reducing the fit complexity by removing all the negligible uncertainties. The effect of experimental uncertainties on processes representing less than 2% of the total yield in a given region of the fit is neglected. The uncertainties on the $WZjj$-QCD background are therefore neglected in the ZZ-CR. For the same reason, the uncertainties on the $tZ + j$ background in both the QCD-CR and ZZ-CR, as well as on the ZZ-QCD background in the b-CR are neglected, and for the ZZ-EW background, the experimental uncertainties are only evaluated in the ZZ-CR.

For every other combinations of process and region, each individual uncertainty source is evaluated. A smoothing procedure is applied in order to reduce the impact of statistics-related effects, and in cases where the uncertainty's +1 σ and -1 σ variations are found to pull the nominal distribution in the same direction in a given bin, the largest of these two variation is symmetrized in that bin and used to define the final uncertainty band.

After being treated, the experimental systematic uncertainties are considered only if they are found to create a ± 1 σ variation from the nominal prediction larger than 0.5% in at least

one of the fit's templates bins. This procedures is applied for each sample, and each region separately, resulting in a total of 67 distinct systematic sources conserved, out of 96 considered. A single NP θ is then defined for each individual source, in order to fully correlate its impact on all the processes it is considered for. It is verified that removing the negligible experimental systematic uncertainties does not impact the fits sensitivity. The expected impact from these NP on the sensitivity to the $WZjj$-EW signal is shown in Figure 5.12.

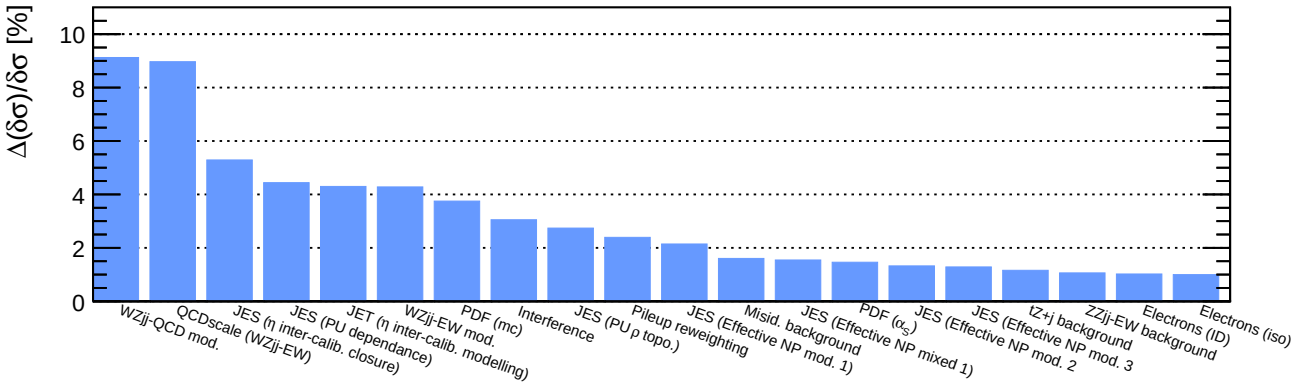

Figure 5.12: Expected relative impact of nuisance parameters on the total uncertainty on the cross-section measurement. Only the 20 top-ranked NP are displayed for readability.

5.3 Observation of $WZjj$-EW production with 36 fb^{-1} of data

This section presents the first observation of the electroweak $WZjj$-EW process. This observation is based on the event selection described in Section 5.1 and analysis strategy discussed above in Section 5.2. In Section 5.3.1, the results are presented, and post-unblinding cross-checks to understand them are described. Section 5.3.2 describes an additional study made to understand the apparent discrepancies in the conclusion between this observation, and the $WZjj$-EW measurement performed by the CMS collaboration, that were both published at a similar time. Finally, Section 5.4 contextualises this observation and establishes the future prospects for the upcoming analyses, wih the full Run 2 LHC data, and with future experiments.

5.3.1 $WZjj$-EW fiducial cross-section measurement

5.3.1.1 Phase-space definition

The first type of measurement performed in the scope of the leptonic $WZjj$-EW analysis at 36 fb^{-1} is that of the fiducial cross-section of the signal process in the so-called VBS phase-space. Dressed leptons are used, accounting for the effect from the final state QED radiation, by adding to the generated lepton the energy from radiated photons within a $\Delta R < 0.1$ cone around it. Leptons originating from a τ-lepton decay are not considered. The dressed leptons are matched to the boson they originate from through the so-called resonant-shape algorithm, where leptons are either associated to the W- or Z-boson depending on the value of the estimator

$$P = \left| \frac{1}{m^2_{\ell^+\ell^-} - (m_Z^{\mathrm{PDG}})^2 + i\Gamma_Z^{\mathrm{PDG}} m_Z^{\mathrm{PDG}}} \right|^2 \times \left| \frac{1}{m^2_{\ell^\pm\nu} - (m_W^{\mathrm{PDG}})^2 + i\Gamma_W^{\mathrm{PDG}} m_W^{\mathrm{PDG}}} \right|^2 , \qquad (5.8)$$

where m_V^{PDG} and Γ_V^{PDG} represent the world average mass and decay width [8] for the boson V (W- or Z-boson). All possible combinations of two same-flavour, opposite-charge leptons are considered as potential Z bosons, with the remaining lepton associated to the W-boson, and the configuration yielding the highest value of P is use to determine the chosen assignment. The jets are reconstructed using the anti-k_t algorithm from all stable particles within a radius parameter $R = 0.4$ from the seed parton, excluding particles associated to the W and Z decays. Only jets with $p_{\mathrm{T}} > 25$ GeV are considered.

The particle-level requirements made on lepton and jets to define the VBS phase-space are referenced in Table 5.5. These requirements are defined so that the phase-space closely matches the SR definition, defined in Section 5.1, and includes a particle-level b-quark veto, applied in order to exclude the $tZ + j$ contribution from the signal definition, as discussed is Section 1.4.2.

5.3.1.2 $WZjj$-EW and Inclusive $WZjj$ Fiducial cross-section definitions

The $WZjj$-EW fiducial cross section $\sigma^{\mathrm{fid.,meas.}}_{WZjj\text{-EW}}$ can be estimated directly through the measurement of the $WZjj$-EW signal strength $\mu_{WZjj\text{-EW}}$, defined as

$$\mu_{WZjj\text{-EW}} = \frac{N^{\mathrm{signal}}_{\mathrm{data}}}{N^{\mathrm{signal}}_{\mathrm{MC}}} = \frac{\sigma^{\mathrm{fid.,meas.}}_{WZjj\text{-EW}}}{\sigma^{\mathrm{fid.,MC}}_{WZjj\text{-EW}}} , \qquad (5.9)$$

Table 5.5: Fiducial phase-space definition for the $WZjj$ cross-section measurements.

Variable	Phase-space requirement
Lepton $\|\eta\|$	< 2.5
$p_{\mathrm{T}}^{\ell_Z}$ [GeV]	> 15
$p_{\mathrm{T}}^{\ell_W}$ [GeV]	> 20
$\|m_Z - m_Z^{\mathrm{PDG}}\|$ [GeV]	< 10
m_{T}^W [GeV]	> 30
$\Delta R(\ell_Z^-, \ell_Z^+)$	> 0.2
$\Delta R(\ell_Z, \ell_W)$	> 0.3
two leading jets [GeV]	> 40
$\|\eta_j\|$ two leading jets	< 4.5
Jet multiplicity	≥ 2
$\eta_{j1} \cdot \eta_{j1}$	< 0
m_{jj} [GeV]	> 500
$\Delta R(j, \ell)$	> 0.3
$N_{b-\mathrm{quark}}$	$= 0$

where $N_{\mathrm{data}}^{\mathrm{signal}}$ ($N_{\mathrm{MC}}^{\mathrm{signal}}$) is the number of signal events evaluated from (before) the signal-extraction fit, and $\sigma_{WZjj\text{-EW}}^{\mathrm{fid.,MC}}$ is the predicted cross section by Sherpa 2.2.2. It is expressed as the average over the four decay channels eee, $ee\mu$, $\mu\mu e$ and $\mu\mu\mu$.

In addition, the inclusive $WZjj$ fiducial cross-section is also measured. This correspond to the sum of $WZjj$-EW and $WZjj$-QCD processes and their interference. As the $WZjj$-QCD production is constrained in the fit in a broader selection than the $WZjj$-EW signal, and considering that its normalisation is treated as a source of uncertainty on the $WZjj$-EW measurement, the choice is made not to directly extract the inclusive $WZjj$ cross-section from the fit. It is instead evaluated as

$$\sigma_{WZjj}^{\mathrm{fid.}} = \frac{N_{\mathrm{data}} - N_{\mathrm{bkg}}}{\mathcal{L} \cdot C_{WZjj}} \times \left(1 - \frac{N_\tau}{N_{\mathrm{all}}}\right) . \tag{5.10}$$

In this formula, N_{data} and N_{bkg} represent the observed data yield in the SR and the post-signal-extraction-fit background yield respectively. The quantity $\mathcal{L} = 36.1 \pm 0.8$ fb^{-1} is the integrated luminosity. The term between parentheses accounts for, and removes, the contribution from τ-lepton decays, assuming lepton universality. This contribution depends on the relative contribution of $WZjj$-EW and $WZjj$-QCD to the measured $WZjj$ cross-section, and therefore cannot be estimated and subtracted, as done for the other backgrounds. It is estimated using the post-fit MC and is found to contribute about 4.7 % of the selection. The uncertainties on this estimate are found to be negligible. The quantities N_τ and N_{all} respectively the post-fit

number of $WZjj$ events with at least one of the final state leptons originating from a τ-lepton decay, and the total number of $WZjj$ events entering the selection, summing the post-fit $WZjj$-QCD and $WZjj$-EW contributions.

Finally, $C_{WZjj} = 0.52 \pm 0.04$ is a correction factor accounting for the detector-related effects affecting the final state particle reconstruction and identification. It is computed using Sherpa, as the mean over the four considered WZ decay channels of the ratio between the number of reconstructed signal events in the SR at detector level over the number of generator-level events in the fiducial VBS phase space defined in Section 5.3.1.1. The uncertainty on its value is evaluated by comparing the coefficient value obtained using Sherpa and MadGraph predictions. Additional sources of uncertainties were evaluated, and found to be negligible. This includes the MC statistical uncertainty, and PDF and QCD scale uncertainties.

5.3.1.3 Fiducial cross-section measurement results

The measurement is performed following the strategy explained in Section 5.2.3, consisting in a two-step template fit: the background-only fit to correct for the suspected misprediction of the main background processes cross-sections, followed by the signal-extraction fit.

The correction factors obtained for the $WZjj$-QCD, $t\bar{t}+V$ and ZZ-QCD processes from the background-only fit are listed in Table 5.6. One can especially note the 32 % downscaling required for the $WZjj$-QCD process to match data, which demonstrates that Sherpa predicts a too high cross-section for this process. The associated uncertainties are shown in order to illustrate the good constrain power of the CRs on the background normalisations, and contains the contribution from all the systematics implemented in the signal-extraction fit, as constrained by the CRs. However, it is not possible to test the validity of the propagation of these constraints to the signal region in the setup used, and the pre-background-only-fit uncertainties are again used in the signal-extraction fit.

Table 5.6: Correction factors extracted from the background-only fit. The corresponding total uncertainties are quoted.

Correction factor	Value
$\mu_{WZjj\text{-QCD}}$	0.68 ± 0.21
$\mu_{t\bar{t}+V}$	1.22 ± 0.23
$\mu_{ZZ\text{-QCD}}$	1.20 ± 0.31

Figure 5.13 shows the template distributions after application of these correction factors. One can note the improved data-to-MC agreement in the three CRs, with respect to the

corresponding pre-fit distributions shown in Figure 5.9 from Section 5.2.3.

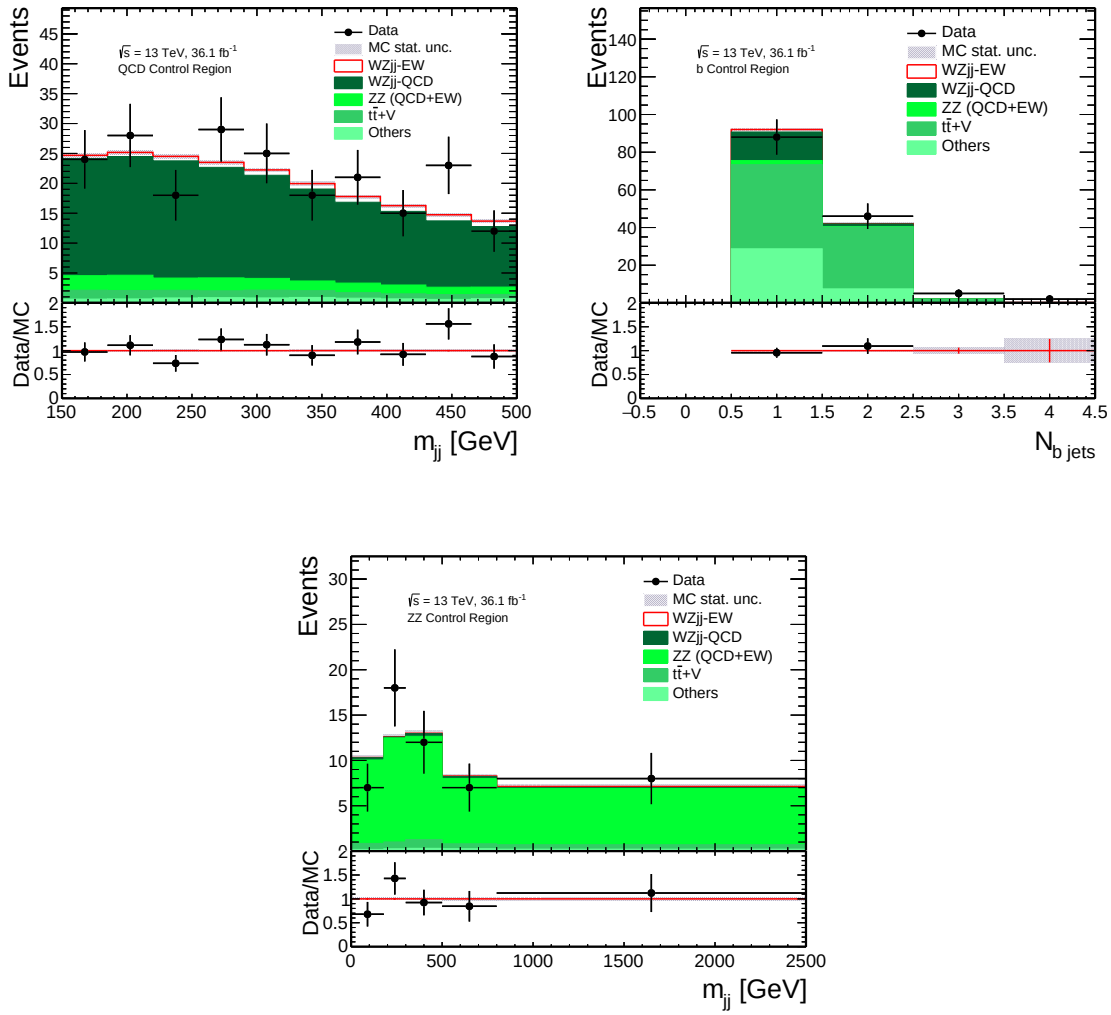

Figure 5.13: Control distributions of m_{jj} in the QCD-CR (top-left), $N_{b\text{-jets}}$ in the b-CR (top-right) and m_{jj} in the ZZ-CR (bottom) after application of the $WZjj$-QCD, $t\bar{t}+V$ and ZZ-QCD correction factors from the background-only fit.

A similar observation can be made looking at the post-background-only-fit BDT score distribution in the QCD-CR, as illustrated by the left distribution from Figure 5.14.

These corrected distributions are used as inputs to the signal-extraction fit. Before the SR unblinding, this fit is performed using a pseudo-dataset, referred to later on as the Asimov dataset [103], both in the SR and in the three control regions. This dataset is constructed by summing the MC contributions from all the processes considered in the fitted regions, and setting the statistical uncertainty in each bin to $\sqrt{N}$, with N the number of events in the bin.

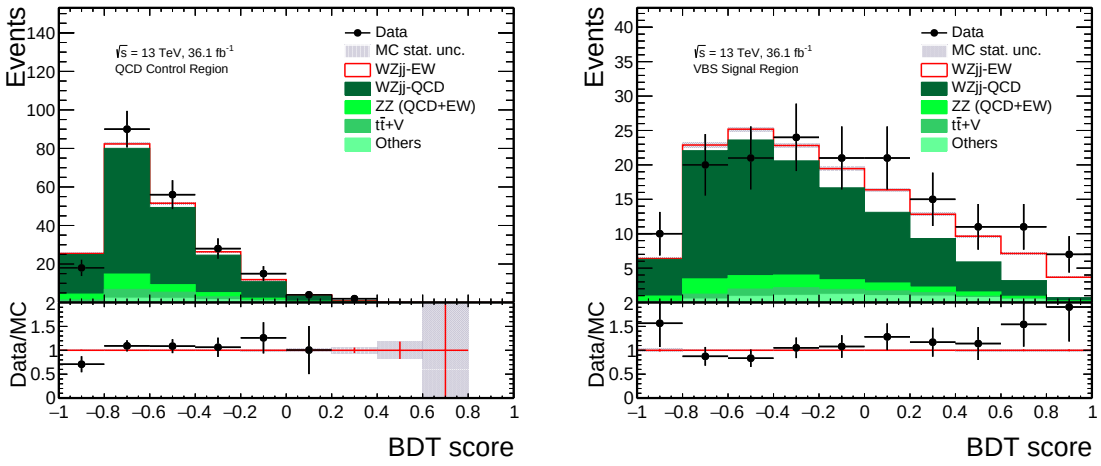

Figure 5.14: Control distributions of the BDT score in the QCD-CR (left) and in the SR (right) after application of the $WZjj$-QCD, $t\bar{t}+V$ and ZZ-QCD correction factors from the background-only fit.

By performing the fit on the Asimov dataset, the achievable sensitivity, assuming a perfect accuracy of the MC predictions, can be evaluated.

This fit led to an expected significance of 3.2 σ on the measurement, and to a measured $WZjj$-EW cross-section with an associated total uncertainty of 39 %, largely dominated by the statistical uncertainty, which represents alone an uncertainty of 37 % of the cross-section. The same fit performed on data led to somewhat unexpected conclusions. Although correction factors were applied before performing the fit, from constraints coming from the three CRs, the inclusion of the SR is found to provide an additional, non-negligible, impact on the correction factors for the $WZjj$-QCD, $t\bar{t}$+V and ZZ-QCD normalisations, thanks to the important shape discrimination arising from the use of the BDT score as a template variable. The additional correction factors $\mu_{WZjj\text{-QCD}} = 0.82 \pm 0.23$, $\mu_{t\bar{t}+V} = 0.87 \pm 0.23$ and $\mu_{ZZ\text{-QCD}} = 1.12 \pm 0.37$ are extracted. By multiplying these to the already applied correction factors obtained from the background-only fit, the total correction to the corresponding processes are obtained. These are listed in Table 5.7.

The signal strength is measured to be

$$\mu_{WZjj\text{-EW}} = 1.77\ ^{+0.44}_{-0.40}\,(\text{stat.})\ ^{+0.15}_{-0.12}\,(\text{exp. syst.})\ ^{+0.15}_{-0.12}\,(\text{mod. syst.})\ ^{+0.04}_{-0.02}\,(\text{lumi.}) = 1.77\ ^{+0.49}_{-0.43}\ ,$$

with the total uncertainty split into its statistical, experimental, and theoretical components, separating as well the impact from the luminosity measurement uncertainty.The background-

Table 5.7: Combined correction factors to the $WZjj$-QCD, $t\bar{t}+V$ and ZZ-QCD production cross-sections, computed as the product of the parameters extracted from the background-only fit and signal-extraction fit. The corresponding total uncertainties, extracted from the signal-extraction fit and scaled to the combined correction factor values, are quoted.

Correction factor	Value
$\mu_{WZjj\text{-QCD}}$	0.56 ± 0.16
$\mu_{t\bar{t}+V}$	1.07 ± 0.28
$\mu_{ZZ\text{-QCD}}$	1.34 ± 0.44

only hypothesis is excluded with a significance of 5.3 standard deviations by this measurement.

The expected and measured significance are found to be very different, and cross-checks are performed on how the treatment of the $WZjj$-QCD background could have influenced the observed significance. Three additional fits are performed, where the signal-extraction fit setup is used with different treatments of the $WZjj$-QCD background. In the first fit, the background-only fit correction to the $WZjj$-QCD background is not applied, but $\mu_{WZjj\text{-QCD}}$ is kept as a free parameter of the fit. For the second fit, the correction factor is applied, but not $\mu_{WZjj\text{-QCD}}$. Finally, for the third fit, the correction factor is not applied, and $\mu_{WZjj\text{-QCD}}$ is also removed. The results from these fit are compared to the signal-extraction fit results in Table 5.8. The significance of the observation is found to be similar for the three cross-check fits, and does not deviate significantly from that of the signal-extraction fit. The main differences appear in the pull of the $WZjj$-QCD theory- and modelling-related nuisance parameters. When $\mu_{WZjj\text{-QCD}}$ is absent from the fit, its impact appears to be absorbed by the QCD scale uncertainty, that gets pulled down by up to 1.6 standard deviations in the case where the background-only fit correction is also not applied.

Table 5.8: Comparison of cross-check fit results to the signal-extraction fit. The differences between the signal-extraction fit (Main result) and the three cross-checks are referenced in the first two rows, corresponding to the pre-fit correction applied to the $WZjj$-QCD background, and to the value of $\mu_{WZjj\text{-QCD}}$ when included (N/A otherwise).

	Cross-check 1	Cross-check 2	Cross-check 3	Main result
$WZjj$-QCD correction	1	0.68	1	0.68
$\mu_{WZjj\text{-QCD}}$	0.59 ± 0.16	N/A	N/A	0.82 ± 0.23
QCD scale pull [σ]	0.34 ± 0.95	-0.27 ± 0.42	-1.6 ± 0.38	0.00 ± 0.99
QCD modelling pull [σ]	0.22 ± 0.81	0.13 ± 0.71	0.0 ± 0.73	0.21 ± 0.79
$\mu_{WZjj\text{-EW}}$	1.74 ± 0.43	1.75 ± 0.48	1.69 ± 0.40	1.77 ± 0.46
Significance (exp.) [σ]	2.7	3.2	2.7	3.2
Significance (meas.) [σ]	5.3	5.3	5.2	5.3

A comparison of the expected results to the actual measurement is shown in Figure 5.15, on which the NLL dependence on $\mu_{WZjj\text{-EW}}$ is illustrated. The good sensitivity of the measurement appears to be partly due to the asymmetrical behaviour of the NLL curves. This asymmetry is explained by the good signal-background separation provided by the BDT score, and the correspondingly large event statistics effectively useful to the signal constraint. This is verified by performing an additional fit using the lepton centrality ζ_ℓ as a template variable, that yielded similar results in terms of the measured parameter central value of $\mu_{WZjj\text{-EW}} = 1.66 \pm 0.56$ (stat.), but a much more symmetrical NLL and a correspondingly larger relative statistical uncertainty, and lower significance of 3.2 σ (1.6 σ expected) Deviations from

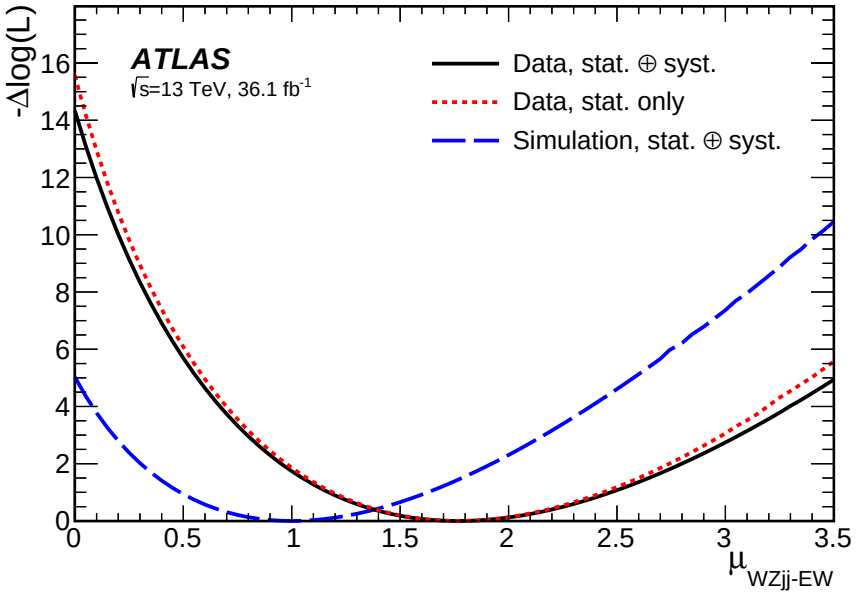

Figure 5.15: Negative Log. Likelihood of the $WZjj$-EW signal-extraction fit as a function of the signal strength $\mu_{WZjj\text{-EW}}$. The full black line shows the measurement, while the dotted red line shows a measurement performed considering only the statistical uncertainty, and the dashed blue line the expected results using the Asimov dataset.

one can also be noted for both $\mu_{WZjj\text{-EW}}$ and $\mu_{WZjj\text{-QCD}}$, indicating a non-negligible underestimation of the $WZjj$-EW production cross-section from Sherpa for the former, and oppositely an overestimate of the $WZjj$-QCD prediction from this generator for the latter. However, the significance of the observed deviations is less than two standard deviations, because of the still large theory-related and statistical uncertainties. As an additional post-unblinding cross-check to validate this observation, a comparison is made between two simplified fits. These fits use identical setups, with the exception of the $WZjj$-EW signal template, generated using either Sherpa or MadGraph, only accounting for the statistical uncertainty, and the uncertain-

ties on the minor background normalisations described in Section 5.2.4. The corresponding $WZjj$-EW signal strengths are found to be compatible, with

$$\mu^{\text{Sherpa}}_{WZjj\text{-EW}} = 1.72 \pm 0.42$$

and

$$\mu^{\text{MadGraph}}_{WZjj\text{-EW}} = 1.41 \pm 0.35.$$

The prediction from MadGraph is found to be closer to the measurement. Moreover, both these fits exclude the background-only hypothesis with the same significance of 5.4 σ, strengthening the validity of the observation.

The post-fit distributions of the template variables are shown in Figure 5.16, in which much improved agreement is seen. The corresponding yields are detailed in Table 5.9.

Table 5.9: Observed and expected numbers of events in the signal region and in the three control regions, after the fit. The expected number of $WZjj$-EW events from Sherpa and the estimated number of background events from the other processes are shown. The sum of the backgrounds containing misidentified leptons is labelled 'Misid. leptons'. The total correlated post-fit uncertainties are quoted.

	SR	QCD-CR	b-CR	ZZ-CR
Data	161	213	141	52
Total predicted	167 ± 11	204 ± 12	146 ± 11	51.3 ± 7.0
$WZjj$-EW (signal)	44 ± 11	8.52 ±0.41	1.38±0.10	0.211±0.004
$WZjj$-QCD	91 ± 10	144 ± 14	13.9± 3.8	0.94 ± 0.14
Misid. leptons	7.8 ± 3.2	14.0 ± 5.7	23.5± 9.6	0.41 ± 0.18
ZZ-QCD	11.1± 2.8	18.3 ± 1.1	2.35±0.06	40.8 ± 7.2
$tZ + j$	6.2 ± 1.1	6.3 ± 1.1	34.0± 5.3	0.17 ± 0.04
$t\bar{t} + V$	4.7 ± 1.0	11.14±0.37	71 ± 15	3.47 ± 0.54
ZZ-EW	1.80±0.45	0.44 ±0.10	0.10±0.03	4.2 ± 1.2
VVV	0.59±0.15	0.93 ±0.23	0.13±0.03	1.06 ± 0.30

The total uncertainties are shown in both cases. Their impact, split by categories, are detailed in Table 5.10. The impact from each category is evaluated by running alternative versions of the signal-extraction fit, in which all the nuisance parameters related to this category are fixed to their nominal value, and subtracting in quadrature the total uncertainty obtained from this fit to the total uncertainty from the signal-extraction fit. With this method, the evaluated contribution to the total uncertainty doesn't account for the correlations between the different categories.

Although the uncertainties on the measurement are largely dominated by the statistical

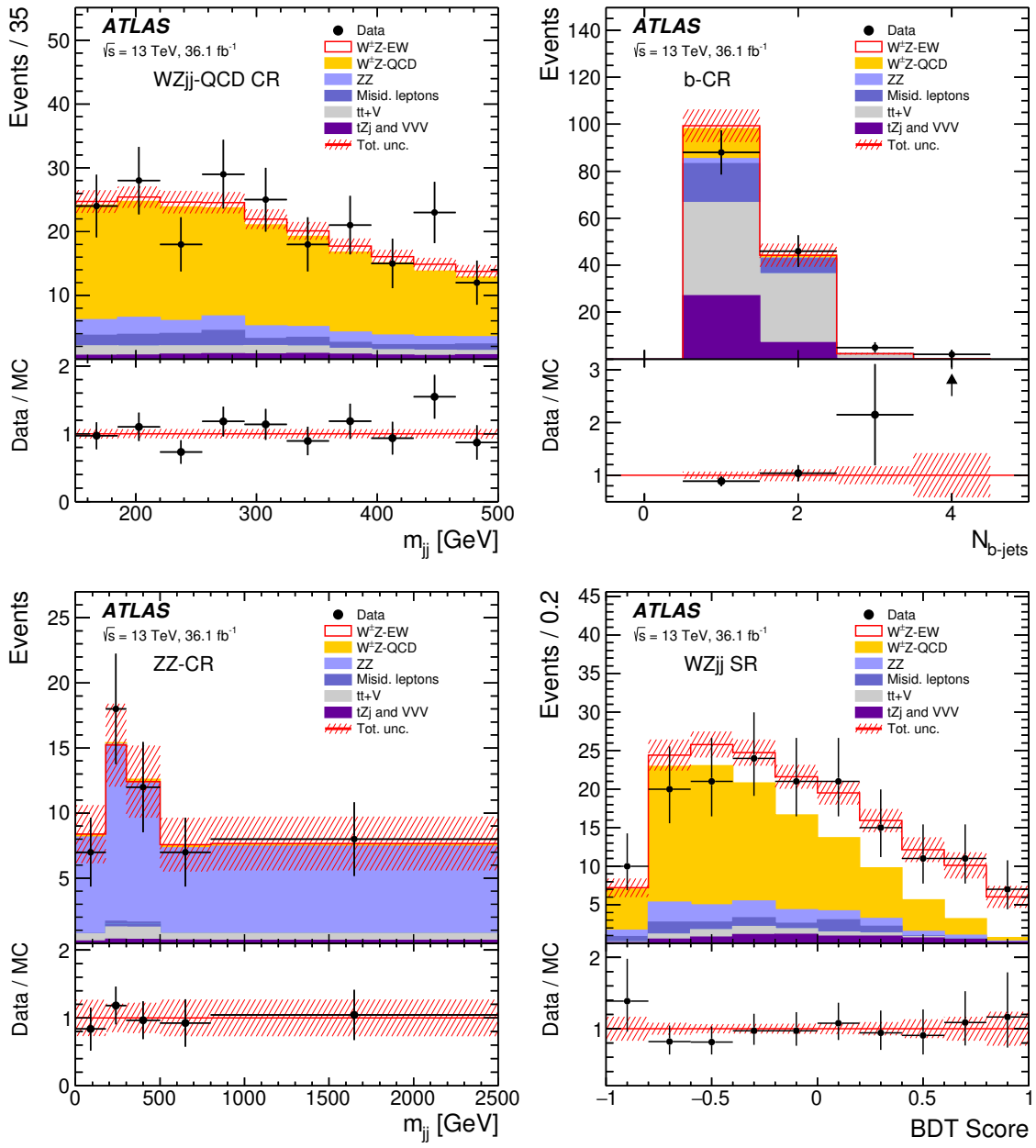

Figure 5.16: Distributions of m_{jj} in the QCD-CR (top-left), $N_{b\text{-jets}}$ in the b-CR (top-right), m_{jj} in the ZZ-CR (bottom-left) and the BDT score in the SR (bottom-right) after the signal extraction fit.

Table 5.10: Summary of the relative uncertainties on the fiducial cross-section measurement. The uncertainties are reported as percentages.

Source	Uncertainty [%]
$WZjj$-EW theory modelling	4.8
$WZjj$-QCD theory modelling	5.2
$WZjj$-EW and $WZjj$-QCD interference	1.9
Jets	6.6
Pile-up	2.2
Electrons	1.4
Muons	0.4
b-tagging	0.1
MC statistics	1.9
Misid. lepton background	0.9
Other backgrounds	0.8
Luminosity	2.1
Total Systematic uncertainty	10.7

uncertainty, the impact of systematic uncertainties is found to be non-negligible. This is especially true for the modelling uncertainties, and jet-related uncertainties. Both the uncertainties on the $WZjj$-EW and $WZjj$-QCD modelling are found to contribute about 5 %, while jet uncertainties are found to be the leading systematic source, with a 6.6 % contribution to the total uncertainty on the measurement.

The measured value of $\mu_{WZjj\text{-EW}}$ corresponds to an integrated fiducial cross-section, for a single fully-leptonic decay channel (eee, $ee\mu$, $\mu\mu e$ or $\mu\mu\mu$), of

$$\begin{aligned}\sigma^{\text{fid.}}_{WZjj\text{-EW}} &= 0.57\,^{+0.14}_{-0.13}\,(\text{stat.})\,^{+0.05}_{-0.04}\,(\text{exp. syst.})\,^{+0.05}_{-0.04}\,(\text{mod. syst.})\,^{+0.01}_{-0.01}\,(\text{lumi.})\ \text{fb}\\ &= 0.57\,^{+0.16}_{-0.14}\ \text{fb},\end{aligned}$$

that can be compared to the corresponding prediction from Sherpa 2.2.2:

$$\sigma^{\text{fid., EW th.}}_{\text{Sherpa}} = 0.321 \pm 0.002\,(\text{stat.})^{+0.005}_{-0.005}\,(\text{PDF})^{+0.027}_{-0.023}\,(\text{scale})\ \text{fb}\,. \tag{5.11}$$

It is worth reminding that, as discussed in Section 5.2.4, the measured cross-section includes the contribution from the interference between $WZjj$-EW and $WZjj$-QCD production, which is not the case for the predicted value from Sherpa. Additionally, this cross-section only accounts for the leptonic decay channels, excluding the $W^{\pm}$ and Z decays into τ leptons.

The measured $WZjj$ cross-section is found to be

$$\begin{aligned}\sigma^{\text{fid.}}_{W^{\pm}Zjj} &= 1.68 \pm 0.16\,(\text{stat.}) \pm 0.12\,(\text{exp. syst.}) \pm 0.13\,(\text{mod. syst.}) \pm 0.044\,(\text{lumi.})\ \text{fb}\,, \\ &= 1.68 \pm 0.25\ \text{fb}\,.\end{aligned}$$

This can be compared to the predicted cross-section from SHERPA of

$$\sigma^{\text{fid., Sherpa}}_{WZjj} = 2.15 \pm 0.01\,(\text{stat.}) \pm 0.05\,(\text{PDF})^{+0.65}_{-0.44}\,(\text{scale})\ \text{fb},$$

where the interference contribution isn't accounted for. This comparison is illustrated, and detailed for each of the considered $WZjj$ decay channels, in Figure 5.17.

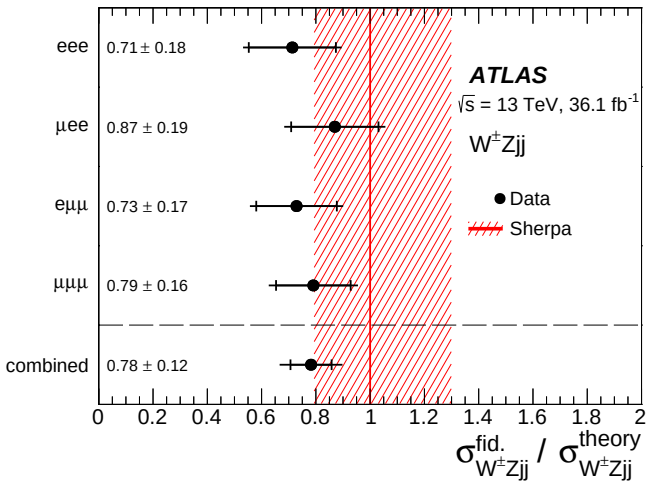

Figure 5.17: Ratio of the measured $WZjj$ fiducial cross-section and the prediction from SHERPA, for the four WZ decay channels and their combination.

5.3.2 Comparison to CMS results

In a close time-scale to the publication of the $WZjj$-EW observation presented in this thesis, the CMS Collaboration published their study of the $WZjj$-EW production with data from 2015 and 2016 [64]. The strategy defined for this measurement is very different from the one used here, and yielded very different observations, most notably a null hypothesis disfavoured with a significance of only 2.2 σ. The expected sensitivities of the two analyses are also different, although less so, with 2.5 σ expected by CMS and 3.2 σ for this thesis work.

Due to the large differences in the analysis strategies, the published results cannot be directly compared. An alternative event selection is therefore defined, in order to evaluate the impact on the observed sensitivity of an analysis strategy resembling that of the CMS experiment. The main differences between the selection used by the CMS collaboration (CMS selection) and that of the observation described in this thesis, used to define the VBS signal region (hereafter referred to as the observation selection), as well as the new requirement implemented for the comparison (modified selection), are given in Table 5.11.

Table 5.11: Comparison of the CMS and ATLAS event selection requirements for the 36 fb^{-1} $WZjj$-EW analyses. Only the requirements with notable differences are listed in the first two columns. The third column references the modifications applied to the ATLAS selection for the reanalysis.

Requirements	CMS selection	Obs. selection	Mod. selection
$m_{3\ell}$[GeV]	> 100	–	> 100
$m_{\ell\ell}$[GeV]	> 4	–	> 4
p_T^j[GeV]	> 50	> 40	> 50
$\Delta\eta(j1, j2)$	≥ 2.5	–	≥ 2.5
$\eta_{j1} \cdot \eta_{j2}$	–	< 0	–
$\lvert\eta_{3\ell} - \frac{1}{2}(\eta_{j1} + \eta_{j2})\rvert$	< 2.5	–	< 2.5

Although the modified selection is much closer to the CMS selection, a few differences still exist, with, for instance, the CMS analysis using a Z-mass window cut $|m_Z - m_Z^{\text{PDG}}| < 15$ GeV, that is not reproduced, and the lepton isolation and identification requirements are not trivially comparable. Due to the remaining differences, no direct comparison can be made between the published CMS results and results obtained using the modified selection. However, comparing the observation and modified selections can give an insight into the conclusions such comparison would yield.

On top of the different event selections, the fit strategies are not the same for both analysis. While our observation relies on the use of a BDT discriminant as a template variable in the high-m_{jj} signal region, CMS uses a two-dimensional distribution of $m_{jj} \times \Delta\eta(j1, j2)$.

This distribution is reproduced for the comparison, and is shown in Figure 5.18 for both the observation and modified selection.

The MC samples used for the comparison are the same as for the rest of the analysis, and the correction factors derived from the background-only fit are applied to the $WZjj$-QCD, $t\bar{t}+V$ and $ZZjj$ contributions. The misidentified background estimate, however, is not data-driven, but is instead taken from MC.

Additional key differences between the analyses are found in the evaluation and impact of the systematic uncertainties. The impact of object-related uncertainties heavily depend on the detector design, and choices made for the particle reconstruction methods, and therefore cannot be fully reproduced either. For the theory-related uncertainty, a fair comparison can only be made with the same MC generators. CMS uses MadGraph5_aMC@NLO v2.4.2 to simulate both the $WZjj$-EW and $WZjj$-QCD production, which was not available for this study. Following these points, the choice is made to only include statistical uncertainty in the comparison.

Four binned likelihood fits are performed for the comparison. The observation and modified selections are compared, using either the main analysis' BDT score, or the two-dimensional $m_{jj} \times \Delta\eta(j1, j2)$ distribution as template. The BDT score distribution used for the modified selection fit is shown in Figure 5.19, and can be compared to that of the VBS signal region shown in Figure 5.14.

In the four fits compared, the measured parameter is the $WZjj$-EW signal strength $\mu_{WZjj\text{-EW}}$, with the $WZjj$-QCD normalisation also left free to float. These fits are performed both to Asimov data and to the 2015-2016 dataset. A single signal region is used, with $m_{jj} > 500$ GeV and $N_{b\text{-jet}} = 0$, as defined both in the present analysis and that of the CMS collaboration. The background control regions are not implemented, as the background normalisations are already corrected, and no systematic uncertainties are implemented.

The results of these fits are compared in Table 5.12. One can note that the selection has little impact on the sensitivity.On the other hand, using the BDT score as a template is found to bring a large improvement on the expected sensitivity, and the difference is found to be much larger for the fits to data. Concerning the measured parameter $\mu_{WZjj\text{-EW}}$, similar conclusions can be drawn with respect to the actual measurement. The measured value of $\mu_{WZjj\text{-EW}}$ reported for MadGraph is obtained by scaling down the measured value with Sherpa by a factor 0.88, corresponding to the ratio of the predicted cross sections from the two generators in the VBS phase space for both the observation and modified selections, making the approximation that this ratio is not affected by the differences between them. Larger deviation of the signal strength from one is seen with the BDT score, with the two other variables yielding parameter

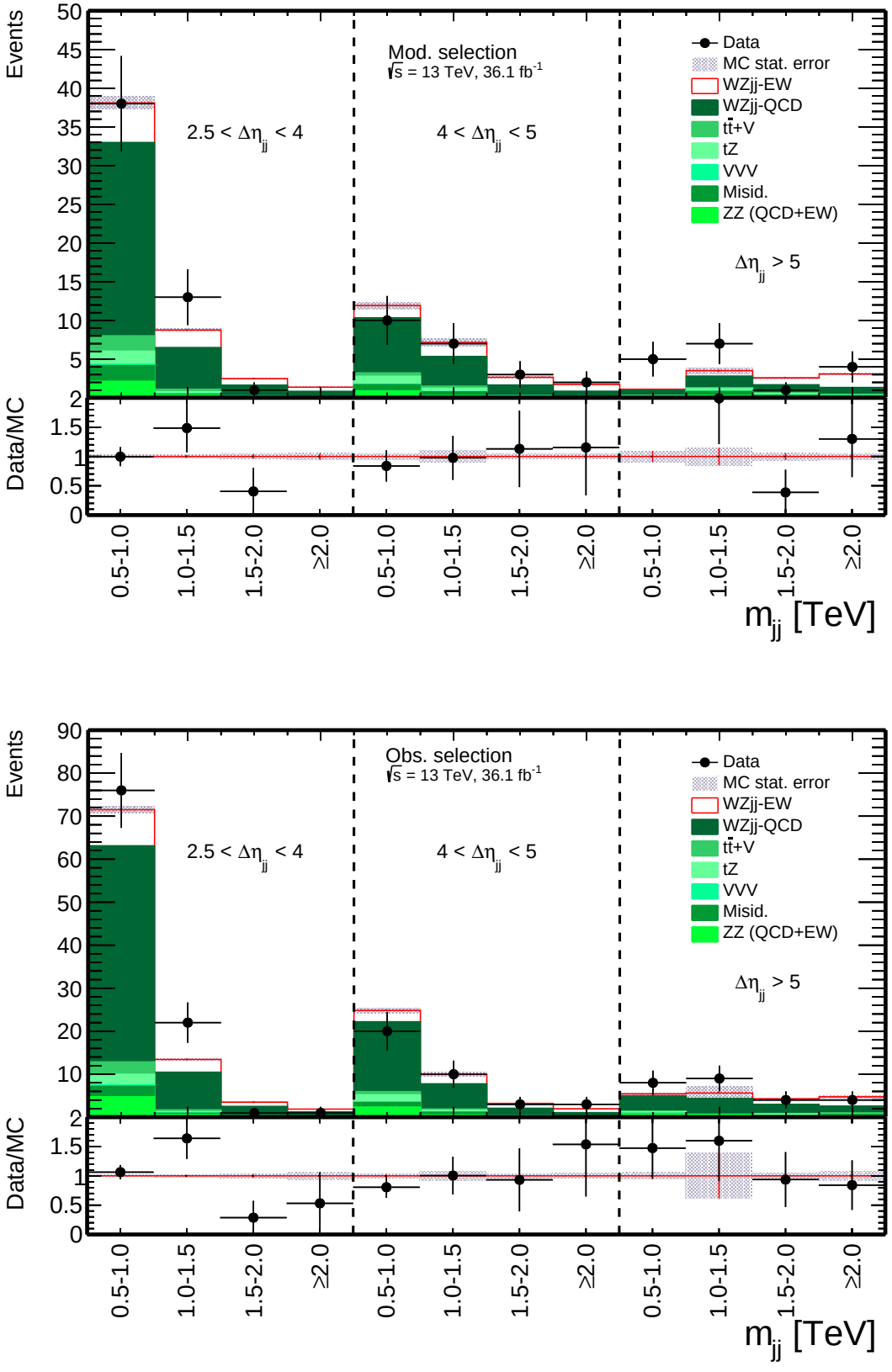

Figure 5.18: 2D distribution of m_{jj} and $|\Delta\eta(j1, j2)|$, as defined in Ref. [64], for the modified selection (top) and the observation selection (bottom).

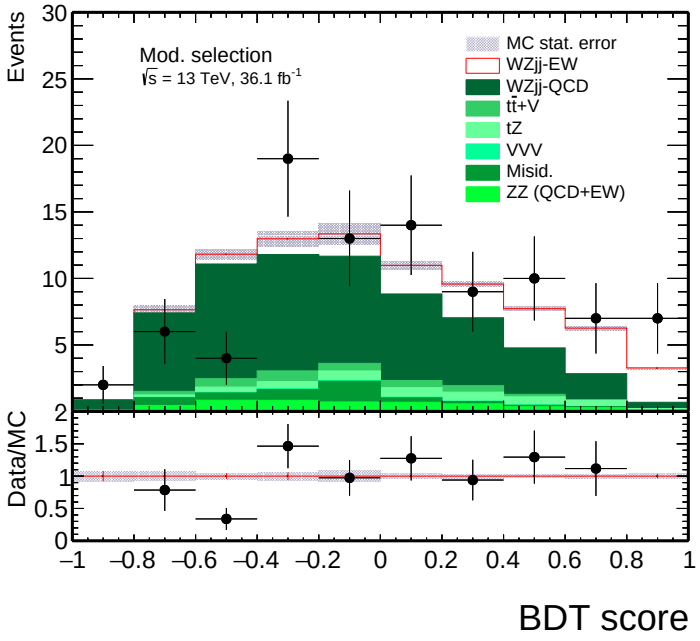

Figure 5.19: Pre-fit distribution of the BDT score in the modified selection.

values compatible with the predictions within the statistical-only uncertainties. This can be explained by the high purity of $WZjj$-QCD events at low BDT score, and the large data-to-MC discrepancy observed in this region, that tend to indicate a larger mismodelling of the $WZjj$-QCD background in the SR than what is measured and corrected in the QCD-CR, which justified the implementation of unconstrained modelling uncertainties as inputs to the signal-fit in our published result.

Table 5.12: Comparison of the fit results in the modified and observation event selections. The signal strengh is evaluated using SHERPA signal template, and scaled down for comparison with MADGRAPH. The uncertainties are only statistical.

	$m_{jj} \times \Delta\eta(j1, j2)$		BDT score	
	Mod.	Obs.	Mod.	Obs.
$\mu_{WZjj\text{-EW}}$ (SHERPA)	1.21 ± 0.53	1.12 ± 0.53	1.72 ± 0.46	1.72 ± 0.42
$\mu_{WZjj\text{-EW}}$ (MADGRAPH)	1.06 ± 0.46	0.98 ± 0.46	1.51 ± 0.40	1.51 ± 0.37
Significance (exp.) [σ]	2.23	2.12	3.16	3.36
Significance (meas.) [σ]	2.60	2.30	5.24	5.58

5.4 Discussion and prospects

The observation of the $WZjj$-EW production and the various studies performed around it confirmed, among other things, the benefits arising from the use of multivariate methods for the signal extraction in analyses with complex topologies, and from a well-defined fitting strategy to constrain both the signal and the dominating background. Incidentally, a similar strategy has been employed by the CMS collaboration for their full Run 2 analysis of the process [65]. Although it has notable differences with the observation we presented, most notably the combined measurement of the ss$WWjj$-EW and $WZjj$-EW processes, the $WZjj$-EW signal extraction is made possible thanks to the implementation and use of a BDT discriminant and of additional control regions for the background constraint.

However, our analysis also highlights some issues that will have to be worked on for the future of such analyses, and are already considered for the ongoing development, at the time of this thesis writing, of the full Run 2 follow-up $WZjj$-EW analysis, that will take advantage of the 139 fb^{-1} of data collected between 2015 and 2018 by ATLAS. Among these issues, the large disagreement between data and simulation that is seen in the studies has to be characterised better. First of all, and concerning all $VVjj$-EW processes, large discrepancies are seen between the various generators used to model the $WZjj$-EW and $WZjj$-QCD processes. Some recent studies allow to partially understand them, to some extent, with, for instance, the identified color-flow propagation bug found in Sherpa 2.2.2 [52], that tend to give the $WZjj$-EW production more QCD-like kinematics. This issue is accounted for in the presented measurement through the conservative estimate of the modelling uncertainty, but its treatment should be improved in the future, to ensure a more accurate evaluation of the potential effects creating the discrepancies, while reducing the impact of the associated uncertainties. Moreover, additional measurements, such as of the differential cross-section for notoriously poorly modelled variables would be highly beneficial as new points of comparison with the current and future generations of Monte Carlo models.

More importantly, the $WZjj$-EW and $WZjj$-QCD productions are simulated at LO for the present analysis, and do not include the potentially large effects of NLO contributions that are discussed in Section 1.4.3. This likely justifies the observed mismatch of about 20 % between the total $WZjj$ cross section measurement and the LO prediction from Sherpa, but the comparison would need to be made with the NLO corrections implemented in order to verify this assumption. The corrections are already known in the case of the $WZjj$-EW production, but have yet to be implemented in the measurements. In addition, this would be helpful in order to perform meaningful interpretations of data, for instance, in the scope of

SMEFT parameter limit setting where a good description of the Standard Model background is required.

Such studies will become critical with the increase of statistics, as both the total $WZjj$ and $WZjj$-EW cross-section measurements will soon be systematically-limited. This will likely happen within the (HL-)LHC data-taking program, with the total luminosity expected to reach 3000 fb^{-1}, or about 20 times more than the full Run 2 statistics by the end of HL-LHC operation, at a center-of-mass energy of $\sqrt{s} = 14$ TeV. Recent prospective studies show that the HL-LHC could allow to perform measurements of the $WZjj$-EW production with close to negligible impact from the statistical uncertainties [104, 105, 106], and to potentially reach sub-percent uncertainties on the $WZjj$-EW cross-section. These prospects indicate that the HL-LHC could allow to gain sensitivity to the $V_LV_L \to V_LV_L$ processes, with a significance of up to 2.7 σ for the ss$W^\pm W^\pm jj$ process using a standard likelihood fit in a VBS-enriched selection, and sensitivity above 3 σ reachable with only 2 ab^{-1} of data through a combination of ATLAS and CMS results. Similar studies have been performed for the W_LZ_L scattering [105] and Z_LZ_L [107], providing more pessimists sensitivity estimates, but however showing that carefully constructed signal extraction methods may improve the expected sensitivity substantially.

Investigation also started about the impact of future generations of colliders on VBS analyses, with some optimistic prospects. Among them, the HE-LHC [108], one of the future collider candidates, is being studied. This collider would operate at a center-of-mass energy of $\sqrt{s} = 27$ TeV, and might be expected to collect 15 ab^{-1} of data in its complete data-taking period, that would potentially allow to reach up to 20 % precision on V_LV_L scattering measurements in the ZZ channel, with the current state-of-the-art signal extraction techniques [104].

More challenging and costly alternatives to the HE-LHC are also considered, with, for instance the FCC-hh [109] that would add an additional 100 km accelerator to the already existing CERN accelerator complex, with the ultimate aim of delivering about 30 ab^{-1} of pp collisions at a center-of-mass energy of $\sqrt{s}$ =100 TeV. This collider could allow to perform systematics-limited measurements of the $W_L^\pm W_L^\pm$ scattering cross section, with down to $\simeq 2$ % uncertainties [110], reaching the precision regime, and opening new perspectives in the search for new physics.

Conclusion

The first observation of the fully-leptonic electroweak $WZjj$ production was presented in this thesis. The measurement is performed with 36 fb^{-1} of pp collision data collected in 2015 and 2016 by the ATLAS experiment at a center-of-mass energy of $\sqrt{s} = 13$ TeV.

This measurement, as well as all other studies targeting $VVjj$ production processes, is aiming to constrain the Vector Boson Scattering sub-process. These processes allow access to the quartic gauge boson coupling, and to the V_LV_L scattering, that closely relate it to the Higgs boson properties and the electroweak symmetry breaking. At the time this result was presented, the only observation of a $VVjj$-EW production process was performed in the $W^{\pm}W^{\pm}jj$ channel, that benefits from a relatively large cross section, and a low contamination from $WWjj$-QCD production. The $W^{\pm}W^{\pm}jj$-EW process is, however, highly impacted by background arising from the misidentification of its final state object. The $WZjj$-EW process was then seen as the second-to-best candidate process for the $VVjj$ observation, and the study of Vector Boson Scattering. Its study benefits from a lower background contamination from misidentified objects compared to the ss$W^{\pm}W^{\pm}jj$, thanks to the three final-state charged leptons, but is however impacted by a large $WZjj$-QCD background and by a lower cross section.

The $WZjj$-EW observation is made possible in large part thanks to the signal-extraction strategy developed in the scope of this thesis, that provides an optimised characterisation of the $WZjj$-QCD background, and separation from the $WZjj$-EW. A BDT discriminant is built for this purpose, in a VBS-enriched signal region. It is based on the characteristic kinematic properties of the $WZjj$-EW signal, that is found to improve the separation with the $WZjj$-QCD background by about 25 % with respect to the single most discriminating kinematic variable, the lepton centrality ζ_ℓ. The analysis statistical framework is developed around the BDT score, by defining a combined binned likelihood fit across the signal region, and three control regions used to constrain three of the main backgrounds to the analysis: the $WZjj$-QCD, $t\bar{t}+V$ and $ZZjj$ productions. The background only hypothesis is rejected with a significance of 5.3 standard deviations (3.2 expected), and the $WZjj$-EW fiducial cross section is measured to be

$$\begin{aligned}\sigma^{\text{fid.}}_{WZjj\text{-EW}} &= 0.57\,^{+0.14}_{-0.13}\,(\text{stat.})\,^{+0.05}_{-0.04}\,(\text{exp. syst.})\,^{+0.05}_{-0.04}\,(\text{mod. syst.})\,^{+0.01}_{-0.01}\,(\text{lumi.})\ \text{fb}\\ &= 0.57\,^{+0.16}_{-0.14}\ \text{fb},\end{aligned}$$

for a single leptonic decay channel (eee, $ee\mu$, $\mu\mu e$ or $\mu\mu\mu$).

A similar analysis was performed by the CMS Collaboration, using a dataset of similar luminosity from events recorded in 2015 and 2016 ,based on a simpler signal extraction procedure, and reached a lower sensitivity of 2.2 σ. More recently, the CMS Collaboration published a new result on the process using the full Run 2 data. Using a strategy closer to the one defined in this thesis, with a BDT discriminant used in a four-region template-fit, they were able to reach much better sensitivity, confirming the strength of the approach developed in this thesis. This allowed a second independent observation of the $WZjj$-EW production.

Although the measurement performed in this thesis is statistically dominated, a non-negligible impact is found from the systematic uncertainties, amounting for 10.7 % of the total uncertainty. Uncertainties on the $WZjj$-EW signal and $WZjj$-QCD theory modelling are found together to be the main contributors to the total systematic uncertainties, followed by the jet-related uncertainties, corresponding respectively to 7.1 % and 6.6 % of the total uncertainty.

The impact from pileup jets is found to be negligible in this analysis. It is however expected to gain in importance for future iterations of the study, starting with the follow-up analysis with full Run 2 data, that are collected in overall higher pileup conditions. For such analysis, the forward detector region is especially relevant, as a large fraction of the $VVjj$ tagging jets are emitted with $|\eta| > 2.5$.

Pileup-jet tagging in this region is handled with the topology-based fJVT discriminant. This tagger is already efficient at suppressing QCD-PU jets, but is not defined adequately for stochastic pileup jets, whose importance is rapidly increasing with the increasing number of pileup events.

A new pileup-jet tagger is therefore developed. This tagger is build as an array of BDT discriminants, combining the pre-existing fJVT discriminant to information on jets shape and structure, allowing the discrimination of stochastic pileup jets. It is found to improve the hard-scatter jet tagging efficiency by up to 25 % in phase-space regions in which the contamination from pile-up jets is the largest, for an overall pileup rejection equivalent to that of the fJVT.

The calibration of this tagger for EMTopo jets is presented, alongside that of the fJVT for both EMTopo and PFlow jets. Two distinct calibration methods are used for EMTopo and PFlow jets, and are compared for the former jet type, showing good method closure. The newly defined MVfJVT is still under study, notably in order to characterise its efficiency dependence on the quark-gluon fraction in data. Its definition is expected to evolve, and to take advantage of the future software and hardware developments that will improve the PU-jet tagging capability, in the upcoming high-pileup regimes.

The impact of both the MVfJVT and fully-calibrated fJVT will be evaluated in the scope of the $WZjj$-EW analysis with the full Run 2 data. In addition, several studies are ongoing for this analysis, both with the aim of providing more precise measurements of the $WZjj$-EW and inclusive $WZjj$ cross sections, and to provide additional, more technically challenging, physical quantities, such as differential cross section for the electroweak signal, in order to prepare future studies aiming at the observation and study of $V_L V_L$ scattering.

Bibliography

[1] G. Valencia and S. Willenbrock. Goldstone-boson equivalence theorem and the higgs resonance. *Phys. Rev. D*, 42:853–859, Aug 1990. (Cited on page 1.)

[2] Aidan Robson. Diboson Physics at the Tevatron. *EPJ Web Conf. Proceedings*, 28:06001, 2012. (Cited on page 1.)

[3] CMS Collaboration. Study of vector boson scattering and search for new physics in events with two same-sign leptons and two jets. *Phys. Rev. Lett.*, 114:051801, Feb 2015. (Cited on pages 1 and 22.)

[4] The ATLAS Collaboration. Measurement of $W^{\pm}W^{\pm}$ vector-boson scattering and limits on anomalous quartic gauge couplings with the atlas detector. *Phys. Rev. D*, 96:012007, Jul 2017. (Cited on pages 1 and 22.)

[5] The ATLAS Collaboration. Measurements of $W^{\pm}Z$ production cross sections in pp collisions at $\sqrt{s} = 8$ TeV with the ATLAS detector and limits on anomalous gauge boson self-couplings. *Phys. Rev. D*, 93(9):092004, 2016. (Cited on pages 1, 91 and 98.)

[6] CMS Collaboration. Observation of electroweak production of same-sign W boson pairs in the two jet and two same-sign lepton final state in proton-proton collisions at $\sqrt{s} =$ 13 TeV. *Phys. Rev. Lett.*, 120(8):081801, 2018. (Cited on pages 1 and 23.)

[7] The ATLAS Collaboration. Observation of electroweak $W^{\pm}Z$ boson pair production in association with two jets in pp collisions at $\sqrt{s} = 13$ TeV with the ATLAS detector. *Phys. Lett. B*, 793:469–492, 2019. (Cited on pages 2 and 23.)

[8] M. Tanabashi et al. Review of Particle Physics. *Phys. Rev. D*, 98(3):030001, 2018. (Cited on pages 4 and 108.)

[9] Tadao Nakano and Kazuhiko Nishijima. Charge Independence for V-particles*. *Progress of Theoretical Physics*, 10(5):581–582, 11 1953. (Cited on page 5.)

[10] UA1 Collaboration. Experimental observation of isolated large transverse energy electrons with associated missing energy at $\sqrt{s} = 540GeV$. *Phys. Lett. B*, 122(CERN-EP-83-13):103–116. 31 p, Jan 1983. (Cited on page 6.)

[11] UA2 Collaboration. Evidence for $Z^0 \to e^+e^-$ at the CERN $\bar{p}p$ Collider. *Phys. Lett. B*, 129:130–140, 1983. (Cited on page 6.)

[12] Antonio Pich. The Standard Model of Electroweak Interactions. In *2010 European School of High Energy Physics*, pages 1–50, 1 2012. (Cited on page 8.)

[13] Jeffrey Goldstone, Abdus Salam, and Steven Weinberg. Broken Symmetries. *Phys. Rev.*, 127:965–970, 1962. (Cited on page 8.)

[14] The ATLAS Collaboration. Observation of a new particle in the search for the Standard Model Higgs boson with the ATLAS detector at the LHC. *Phys. Lett. B*, 716:1–29, 2012. (Cited on page 8.)

[15] CMS Collaboration. Observation of a New Boson with Mass Near 125 GeV in *pp* Collisions at $\sqrt{s} = 7$ and 8 TeV. *JHEP*, 06:081, 2013. (Cited on page 8.)

[16] Peter W. Higgs. Broken Symmetries and the Masses of Gauge Bosons. *Phys. Rev. Lett.*, 13:508–509, 1964. (Cited on page 8.)

[17] F. Englert and R. Brout. Broken symmetry and the mass of gauge vector mesons. *Phys. Rev. Lett.*, 13:321–323, Aug 1964. (Cited on page 8.)

[18] John C. Collins, Davison E. Soper, and George F. Sterman. *Factorization of Hard Processes in QCD*, volume 5, pages 1–91. 1989. (Cited on page 9.)

[19] V.N. Gribov and L.N. Lipatov. Deep inelastic e p scattering in perturbation theory. *Sov. J. Nucl. Phys.*, 15:438–450, 1972. (Cited on page 9.)

[20] Guido Altarelli and G. Parisi. Asymptotic Freedom in Parton Language. *Nucl. Phys. B*, 126:298–318, 1977. (Cited on page 9.)

[21] Yuri L. Dokshitzer. Calculation of the Structure Functions for Deep Inelastic Scattering and e+ e- Annihilation by Perturbation Theory in Quantum Chromodynamics. *Sov. Phys. JETP*, 46:641–653, 1977. (Cited on page 9.)

[22] H1 and ZEUS Collaborations. Combination of measurements of inclusive deep inelastic $e^{\pm}p$ scattering cross sections and QCD analysis of HERA data. *Eur. Phys. J. C*, 75(12):580, 2015. (Cited on page 9.)

[23] Jun Gao, Marco Guzzi, Joey Huston, Hung-Liang Lai, Zhao Li, Pavel Nadolsky, Jon Pumplin, Daniel Stump, and C.-P. Yuan. CT10 next-to-next-to-leading order global analysis of QCD. *Phys. Rev. D*, 89(3):033009, 2014. (Cited on page 9.)

[24] Richard D. Ball, Luigi Del Debbio, Stefano Forte, Alberto Guffanti, Jose I. Latorre, Juan Rojo, and Maria Ubiali. A first unbiased global NLO determination of parton distributions and their uncertainties. *Nucl. Phys. B*, 838:136–206, 2010. (Cited on page 9.)

[25] Sayipjamal Dulat, Tie-Jiun Hou, Jun Gao, Marco Guzzi, Joey Huston, Pavel Nadolsky, Jon Pumplin, Carl Schmidt, Daniel Stump, and C.P. Yuan. New parton distribution functions from a global analysis of quantum chromodynamics. *Phys. Rev. D*, 93(3):033006, 2016. (Cited on page 9.)

[26] NNPDF Collaboration. Parton distributions for the LHC Run II. *JHEP*, 04:040, 2015. (Cited on page 9.)

[27] L.A. Harland-Lang, A.D. Martin, P. Motylinski, and R.S. Thorne. Parton distributions in the LHC era: MMHT 2014 PDFs. *Eur. Phys. J. C*, 75(5):204, 2015. (Cited on page 9.)

[28] Jon Butterworth et al. PDF4LHC recommendations for LHC Run II. *J. Phys. G*, 43(arXiv:1510.03865. OUTP-15-17P. SMU-HEP-15-12. TIF-UNIMI-2015-14. LCTS-2015-27. CERN-PH-TH-2015-249):023001. 65 p, Oct 2015. (Cited on pages 10 and 103.)

[29] Matthias Schott and Monica Dunford. Review of single vector boson production in pp collisions at $\sqrt{s} = 7$ TeV. *Eur. Phys. J. C*, 74:2916, 2014. (Cited on page 11.)

[30] Stefan Höche. Introduction to parton-shower event generators. In *Theoretical Advanced Study Institute in Elementary Particle Physics: Journeys Through the Precision Frontier: Amplitudes for Colliders*, pages 235–295, 2015. (Cited on pages 11 and 13.)

[31] Enrico Bothmann et al. Event Generation with Sherpa 2.2. *SciPost Phys.*, 7(3):034, 2019. (Cited on page 11.)

[32] Johannes Bellm et al. Herwig 7.0/Herwig++ 3.0 release note. *Eur. Phys. J. C*, 76(4):196, 2016. (Cited on page 11.)

[33] D. Amati and G. Veneziano. Preconfinement as a Property of Perturbative QCD. *Phys. Lett. B*, 83:87–92, 1979. (Cited on page 11.)

[34] Torbjorn Sjöstrand, Stephen Mrenna, and Peter Z. Skands. A Brief Introduction to PYTHIA 8.1. *Comput. Phys. Commun.*, 178:852, 2008. (Cited on pages 11 and 58.)

[35] Bo Andersson, G. Gustafson, G. Ingelman, and T. Sjostrand. Parton Fragmentation and String Dynamics. *Phys. Rept.*, 97:31–145, 1983. (Cited on page 11.)

[36] The ATLAS Collaboration. Diboson Physics Studies. Technical Report ATL-PHYS-PUB-2009-038. ATL-COM-PHYS-2009-103, CERN, Geneva, Mar 2009. CSC Note from SM. (Cited on page 12.)

[37] The ATLAS Collaboration. $ZZ \to \ell^+\ell^-\ell'^+\ell'^-$ cross-section measurements and search for anomalous triple gauge couplings in 13 TeV pp collisions with the ATLAS detector. *Phys. Rev. D*, 97(3):032005, 2018. (Cited on page 12.)

[38] CMS Collaboration. Measurement of differential cross sections for Z boson pair production in association with jets at $\sqrt{s} = 8$ and 13 TeV. *Phys. Lett. B*, 789:19–44, 2019. (Cited on page 12.)

[39] The ATLAS Collaboration. Measurement of fiducial and differential W^+W^- production cross-sections at $\sqrt{s} = 13$ TeV with the ATLAS detector. *Eur. Phys. J. C*, 79(10):884, 2019. (Cited on page 12.)

[40] CMS Collaboration. Measurement of the $\mathrm{W^+W^-}$ cross section in pp collisions at $\sqrt{s} = 8$ TeV and limits on anomalous gauge couplings. *Eur. Phys. J. C*, 76(7):401, 2016. (Cited on page 12.)

[41] The ATLAS Collaboration. Higgs boson production cross-section measurements and their EFT interpretation in the 4ℓ decay channel at $\sqrt{s} = 13$ TeV with the ATLAS detector. 4 2020. (Cited on page 12.)

[42] The ATLAS Collaboration. Measurements of gluon-gluon fusion and vector-boson fusion Higgs boson production cross-sections in the $H \to WW^* \to e\nu\mu\nu$ decay channel in pp collisions at $\sqrt{s} = 13$ TeV with the ATLAS detector. *Phys. Lett. B*, 789:508–529, 2019. (Cited on page 12.)

[43] The ATLAS Collaboration. Search for diboson resonances in hadronic final states in 139 fb^{-1} of pp collisions at $\sqrt{s} = 13$ TeV with the ATLAS detector. *JHEP*, 09:091, 2019. (Cited on page 12.)

[44] CMS Collaboration. Search for $\mathrm{Z}\gamma$ resonances using leptonic and hadronic final states in proton-proton collisions at $\sqrt{s} = 13$ TeV. *JHEP*, 09:148, 2018. (Cited on page 12.)

[45] Kaustubh Agashe, Hooman Davoudiasl, Gilad Perez, and Amarjit Soni. Warped gravitons at the cern lhc and beyond. *Phys. Rev. D*, 76:036006, Aug 2007. (Cited on page 12.)

[46] The ATLAS Collaboration. Measurement of $W^{\pm}Z$ production cross sections and gauge boson polarisation in pp collisions at $\sqrt{s} = 13$ TeV with the ATLAS detector. *Eur. Phys. J. C*, 79(6):535, 2019. (Cited on pages 12, 81 and 90.)

[47] The ATLAS Collaboration. Observation of light-by-light scattering in ultraperipheral Pb+Pb collisions with the ATLAS detector. *Phys. Rev. Lett.*, 123(5):052001, 2019. (Cited on page 14.)

[48] David L. Rainwater, R. Szalapski, and D. Zeppenfeld. Probing color singlet exchange in Z + two jet events at the CERN LHC. *Phys. Rev. D*, 54:6680–6689, 1996. (Cited on page 15.)

[49] Christian Gumpert. Measurement of Electroweak Gauge Boson Scattering in the Channel $pp \to W^{\pm}W^{\pm}jj$ with the ATLAS Detector at the Large Hadron Collider, Dec 2014. Thesis defended 27 Feb 2015. (Cited on pages 16 and 17.)

[50] Enrico Bothmann et al. Event Generation with Sherpa 2.2. *SciPost Phys.*, 7(3):034, 2019. (Cited on page 18.)

[51] J. Alwall, R. Frederix, S. Frixione, V. Hirschi, F. Maltoni, O. Mattelaer, H. S. Shao, T. Stelzer, P. Torrielli, and M. Zaro. The automated computation of tree-level and next-to-leading order differential cross sections, and their matching to parton shower simulations. *JHEP*, 07:079, 2014. (Cited on page 18.)

[52] The ATLAS Collaboration. Modelling of the vector boson scattering process $pp \to W^{\pm}W^{\pm}jj$ in Monte Carlo generators in ATLAS. Technical Report ATL-PHYS-PUB-2019-004, CERN, Geneva, Jan 2019. (Cited on pages 19 and 123.)

[53] Stefano Frixione, Paolo Nason, and Carlo Oleari. Matching NLO QCD computations with Parton Shower simulations: the POWHEG method. *JHEP*, 11:070, 2007. (Cited on pages 19, 20 and 58.)

[54] Benedikt Biedermann, Ansgar Denner, and Mathieu Pellen. Complete NLO corrections to W^+W^+ scattering and its irreducible background at the LHC. *JHEP*, 10:124, 2017. (Cited on pages 20 and 23.)

[55] Ansgar Denner, Stefan Dittmaier, Philipp Maierhöfer, Mathieu Pellen, and Christopher Schwan. QCD and electroweak corrections to WZ scattering at the LHC. *JHEP*, 06:067, 2019. (Cited on pages 20 and 21.)

[56] The ATLAS Collaboration. Studies of $Z\gamma$ production in association with a high-mass dijet system in pp collisions at $\sqrt{s} = 8$ TeV with the ATLAS detector. *JHEP*, 07:107, 2017. (Cited on page 22.)

[57] CMS Collaboration. Measurement of the cross section for electroweak production of z in association with two jets and constraints on anomalous quartic gauge couplings in protonproton collisions at s=8ătev. *Physics Letters B*, 770:380 – 402, 2017. (Cited on page 22.)

[58] The ATLAS Collaboration. Measurements of $W^{\pm}Z$ production cross sections in pp collisions at $\sqrt{s} = 8$ TeV with the ATLAS detector and limits on anomalous gauge boson self-couplings. *Phys. Rev. D*, 93(9):092004, 2016. (Cited on pages 22 and 81.)

[59] The ATLAS Collaboration. Search for anomalous electroweak production of ww/wz in association with a high-mass dijet system in pp collisions at $\sqrt{s} = 8$ TeV with the atlas detector. *Phys. Rev. D*, 95:032001, Feb 2017. (Cited on page 22.)

[60] CMS Collaboration. Measurement of electroweak-induced production of Wγ with two jets in pp collisions at $\sqrt{s} = 8$ TeV and constraints on anomalous quartic gauge couplings. *JHEP*, 06:106, 2017. (Cited on page 22.)

[61] O. J. P. Éboli, M. C. Gonzalez-Garcia, and J. K. Mizukoshi. $pp \to jje^{\pm}\mu^{\pm}\nu\nu$ and $jje^{\pm}\mu^{\mp}\nu\nu$ at $\mathcal{O}(\alpha_{\rm em}^6)$ and $\mathcal{O}(\alpha_{\rm em}^4\alpha_s^2)$ for the study of the quartic electroweak gauge boson vertex at cern lhc. *Phys. Rev. D*, 74:073005, Oct 2006. (Cited on page 22.)

[62] Ana Alboteanu, Wolfgang Kilian, and Jürgen Reuter. Resonances and unitarity in weak boson scattering at the LHC. *Journal of High Energy Physics*, 2008(11):010–010, nov 2008. (Cited on page 22.)

[63] The ATLAS Collaboration. Observation of electroweak production of a same-sign W boson pair in association with two jets in pp collisions at $\sqrt{s} = 13$ TeV with the ATLAS detector. *Phys. Rev. Lett.*, 123(16):161801, 2019. (Cited on page 23.)

[64] CMS Collaboration. Measurement of electroweak WZ boson production and search for new physics in WZ + two jets events in pp collisions at $\sqrt{s} = 13$TeV. *Phys. Lett. B*, 795:281–307, 2019. (Cited on pages 23, 91, 119 and 121.)

[65] CMS Collaboration. Measurements of production cross sections of WZ and same-sign WW boson pairs in association with two jets in proton-proton collisions at $\sqrt{s} = 13$ TeV. 5 2020. (Cited on pages 23 and 123.)

[66] The ATLAS Collaboration. Evidence for electroweak production of two jets in association with a $Z\gamma$ pair in pp collisions at $\sqrt{s} = 13$ TeV with the ATLAS detector. *Phys. Lett. B*, 803:135341, 2020. (Cited on page 23.)

[67] CMS Collaboration. Measurement of the cross section for electroweak production of a Z boson, a photon and two jets in proton-proton collisions at $\sqrt{s} = 13$ TeV and constraints on anomalous quartic couplings. *JHEP*, 06:076, 2020. (Cited on page 23.)

[68] CMS Collaboration. Measurement of vector boson scattering and constraints on anomalous quartic couplings from events with four leptons and two jets in proton–proton collisions at $\sqrt{s} = 13$ TeV. *Phys. Lett. B*, 774:682–705, 2017. (Cited on page 23.)

[69] The ATLAS Collaboration. Observation of electroweak production of two jets and a Z-boson pair with the ATLAS detector at the LHC. 4 2020. (Cited on page 23.)

[70] CMS Collaboration. Evidence for vector boson scattering in events with four leptons and two jets in proton-proton collisions at sqrt(s) = 13 TeV. Technical Report CMS-PAS-SMP-20-001, CERN, Geneva, 2020. (Cited on page 23.)

[71] Esma Mobs. The CERN accelerator complex. Complexe des accélérateurs du CERN. Jul 2016. General Photo. (Cited on page 26.)

[72] (Cited on page 27.)

[73] The ATLAS Collaboration. Public luminosity results. `https://twiki.cern.ch/twiki/bin/view/AtlasPublic/LuminosityPublicResultsRun2`, 2020. (Cited on pages 28 and 29.)

[74] The ATLAS Collaboration. The ATLAS Experiment at the CERN Large Hadron Collider. *JINST*, 3:S08003, 2008. (Cited on pages 30, 34 and 36.)

[75] The ATLAS Collaboration. ATLAS Insertable B-Layer Technical Design Report. Technical Report CERN-LHCC-2010-013. ATLAS-TDR-19, Sep 2010. (Cited on page 33.)

[76] The ATLAS Collaboration. Electron reconstruction and identification in the ATLAS experiment using the 2015 and 2016 LHC proton-proton collision data at $\sqrt{s}$ =13 TeV. *Eur. Phys. J. C*, 79:639, 2019. (Cited on pages 40 and 41.)

[77] The ATLAS Collaboration. Muon reconstruction performance of the ATLAS detector in proton–proton collision data at $\sqrt{s}$ =13 TeV. *Eur. Phys. J. C*, 76(5):292, 2016. (Cited on page 44.)

[78] Matteo Cacciari, Gavin P. Salam, and Gregory Soyez. The anti-k_t jet clustering algorithm. *JHEP*, 04:063, 2008. (Cited on page 45.)

[79] S. Catani, Yuri L. Dokshitzer, M. Olsson, G. Turnock, and B.R. Webber. New clustering algorithm for multi - jet cross-sections in e+ e- annihilation. *Phys. Lett. B*, 269:432–438, 1991. (Cited on page 46.)

[80] Gavin P. Salam. Towards Jetography. *Eur. Phys. J. C*, 67:637–686, 2010. (Cited on page 46.)

[81] Matteo Cacciari and Gavin P. Salam. Pileup subtraction using jet areas. *Phys. Lett. B*, 659:119–126, 2008. (Cited on page 47.)

[82] The ATLAS Collaboration. Jet energy scale and resolution measured in proton-proton collisions at $\sqrt{s} = 13$ TeV with the ATLAS detector. Technical report, 7 2020. (Cited on page 48.)

[83] The ATLAS Collaboration. Pile-up subtraction and suppression for jets in ATLAS. (ATLAS-CONF-2013-083), Aug 2013. (Cited on page 52.)

[84] The ATLAS Collaboration. Tagging and suppression of pileup jets. (ATLAS-CONF-2014-018), May 2014. (Cited on pages 52, 53 and 54.)

[85] Andreas Hoecker, Peter Speckmayer, Joerg Stelzer, Jan Therhaag, Eckhard von Toerne, and Helge Voss. TMVA: Toolkit for Multivariate Data Analysis. *PoS*, ACAT:040, 2007. (Cited on pages 53, 57 and 92.)

[86] The ATLAS Collaboration. Identification and rejection of pile-up jets at high pseudorapidity with the ATLAS detector. *Eur. Phys. J. C*, 77(9):580, 2017. [Erratum: Eur.Phys.J.C 77, 712 (2017)]. (Cited on page 54.)

[87] The ATLAS Collaboration. Forward jet vertex tagging using the particle flow algorithm. Technical Report ATL-PHYS-PUB-2019-026, CERN, Geneva, Jul 2019. (Cited on page 55.)

[88] François Chollet et al. Keras. `https://keras.io`, 2015. (Cited on page 57.)

[89] Jerome H. Friedman. Data Analysis Techniques for High-Energy Particle Physics. In *3rd CERN School of Computing*, page 271, 10 1974. (Cited on page 70.)

[90] Taoli Cheng. Recursive Neural Networks in Quark/Gluon Tagging. *Comput. Softw. Big Sci.*, 2(1):3, 2018. (Cited on page 78.)

[91] Gregor Kasieczka, Nicholas Kiefer, Tilman Plehn, and Jennifer M. Thompson. Quark-Gluon Tagging: Machine Learning vs Detector. *SciPost Phys.*, 6(6):069, 2019. (Cited on page 78.)

[92] The ATLAS Collaboration. Technical Design Report for the ATLAS Inner Tracker Pixel Detector. Technical Report CERN-LHCC-2017-021. ATLAS-TDR-030, CERN, Geneva, Sep 2017. (Cited on page 79.)

[93] The ATLAS Collaboration. Technical Design Report: A High-Granularity Timing Detector for the ATLAS Phase-II Upgrade. Technical Report ATL-COM-UPGRADE-2020-019, CERN, Geneva, Jun 2020. (Cited on page 79.)

[94] The ATLAS Collaboration. Identification of Jets Containing b-Hadrons with Recurrent Neural Networks at the ATLAS Experiment. Technical Report ATL-PHYS-PUB-2017-003, CERN, Geneva, Mar 2017. (Cited on page 79.)

[95] Patrick Komiske, Eric Metodiev, and Matthew Schwartz. Deep learning in color: towards automated quark/gluon jet discrimination. *Journal of High Energy Physics*, 2017, 12 2016. (Cited on page 79.)

[96] The ATLAS Collaboration. Quark versus Gluon Jet Tagging Using Charged Particle Multiplicity with the ATLAS Detector. 4 2017. (Cited on page 79.)

[97] S. Schael et al. Precision electroweak measurements on the Z resonance. *Phys. Rept.*, 427:257–454, 2006. (Cited on page 84.)

[98] (Cited on page 87.)

[99] The ATLAS Collaboration. Measurements of b-jet tagging efficiency with the ATLAS detector using $t\bar{t}$ events at $\sqrt{s} = 13$ TeV. *JHEP*, 08:089, 2018. (Cited on page 89.)

[100] Kyle Cranmer, George Lewis, Lorenzo Moneta, Akira Shibata, and Wouter Verkerke. HistFactory: A tool for creating statistical models for use with RooFit and RooStats. 6 2012. (Cited on page 99.)

[101] The ATLAS Collaboration. Multi-Boson Simulation for 13 TeV ATLAS Analyses. Technical Report ATL-PHYS-PUB-2016-002, CERN, Geneva, Jan 2016. (Cited on page 106.)

[102] The ATLAS Collaboration. Modelling of the $t\bar{t}H$ and $t\bar{t}V$ ($V = W, Z$) processes for $\sqrt{s} = 13$ TeV ATLAS analyses. Technical Report ATL-PHYS-PUB-2016-005, CERN, Geneva, Jan 2016. (Cited on page 106.)

[103] Glen Cowan, Kyle Cranmer, Eilam Gross, and Ofer Vitells. Asymptotic formulae for likelihood-based tests of new physics. *Eur. Phys. J. C*, 71:1554, 2011. [Erratum: Eur.Phys.J.C 73, 2501 (2013)]. (Cited on page 110.)

[104] P. Azzi et al. *Report from Working Group 1: Standard Model Physics at the HL-LHC and HE-LHC*, volume 7, pages 1–220. 12 2019. (Cited on page 124.)

[105] The ATLAS Collaboration. Prospective study of vector boson scattering in WZ fully leptonic final state at HL-LHC. Technical Report ATL-PHYS-PUB-2018-023, CERN, Geneva, Oct 2018. (Cited on page 124.)

[106] CMS Collaboration. Prospects for the measurement of electroweak and polarized WZ to 3lv production cross sections at the High-Luminosity LHC . Technical Report CMS-PAS-FTR-18-038, CERN, Geneva, 2018. (Cited on page 124.)

[107] Junho Lee, Nicolas Chanon, Andrew Levin, Jing Li, Meng Lu, Qiang Li, and Yajun Mao. Polarization fraction measurement in ZZ scattering using deep learning. *Phys. Rev. D*, 100(11):116010, 2019. (Cited on page 124.)

[108] A. Abada et al. HE-LHC: The High-Energy Large Hadron Collider: Future Circular Collider Conceptual Design Report Volume 4. *Eur. Phys. J. ST*, 228(5):1109–1382, 2019. (Cited on page 124.)

[109] A. Abada et al. FCC-hh: The Hadron Collider: Future Circular Collider Conceptual Design Report Volume 3. *Eur. Phys. J. ST*, 228(4):755–1107, 2019. (Cited on page 124.)

[110] L. Borgonovi et al. Higgs measurements at FCC-hh. Technical Report CERN-ACC-2018-0045, CERN, Geneva, Oct 2018. (Cited on page 124.)

Abstract: Vector Boson Scattering is among the most sought after types of electroweak process at high-energy collider experiments, as one of the very few processes allowing to probe the quartic gauge boson coupling, and for its close relation to the electroweak symmetry breaking mechanism. These processes are studied through the electroweak production of two bosons associated to two jets ($VVjj$-EW), that suffer from small cross sections, and generally from high background contamination from the QCD-driven $VVjj$ production. This thesis presents studies around the $WZjj$-EW production. Proton-proton collision data collected with the ATLAS experiment at the LHC between 2015 and 2016 at a center-of-mass energy of $\sqrt{s} = 13$ TeV is used, corresponding to an integrated luminosity of 36 fb^{-1}. A first part of the work concerns the suppression of pileup jets, not originating from the primary vertex of the process of interest. Pileup jets in the forward regions of the detector cannot be suppressed using tracking information, and the main tagging tool in this region uses full-event topology instead. However, this tool can only suppress hadronic pileup jets. With the increasing pileup conditions through Run 2, a non-negligible fraction of jets is reconstructed from stochastic energy deposits in the detector. A new tool combining the original tool with jet shape observables is therefore developed, allowing the identification of these stochastic pile-up jets, and an improved overall tagging efficiency. In a second part, the study of the $WZjj$ production in its fully leptonic decay channels is presented. A multivariate discriminant is developed to optimally separate the $WZjj$-EW and $WZjj$-QCD productions. The statistical framework used for the signal extraction is developed around this discriminant, and allowed for the first observation of the $WZjj - EW$ production, with a significance of 5.3 σ, with its cross section measured to be $\sigma^{\text{fid.}}_{W^{\pm}Zjj-EW} = 0.57^{+0.14}_{-0.13}(\text{stat.})^{+0.07}_{-0.06}(\text{syst.})$.

Résumé: La diffusion de bosons vecteurs fait partie des processus du Modèle Standard les plus recherchés dans les collisionneurs de particules. Ils font partie des rares processus permettant d'accéder aux couplages de jauge quartiques, et sont étroitement liés au mécanisme de brisure de symétrie électrofaible. Ces processus sont étudiés au travers de la production électrofaible de deux bosons associés à deux jets ($VVjj$-EW), dont les sections efficaces sont très faibles, et qui sont impactés par une grande contamination des bruits de fond $VVjj$-QCD. Cette thèse présente des études sur la production $WZjj$-EW. Les données de collisions proton-proton collectées avec l'expérience ATLAS au LHC entre 2015 et 2016, avec une énergie au centre de masse $\sqrt{s} = 13$ TeV, sont utilisées, correspondant à une luminosité intégrée de 36 fb^{-1}. Une première partie présente des études sur la suppression des jets d'empilement, ne provenant pas du vertex d'interaction primaire du processus d'intérêt. Les jets d'empilement dans les régions à l'avant du détecteur ne peuvent pas être supprimés en se servant d'information de trajectrographie, et l'outil principal pour les identifier utilise la topologie globale des évènements. Cependant, cet outil peut seulement supprimer les jets d'empilement hadroniques. Avec l'augmentation de l'empilement au travers du Run 2, une fraction non-négligeable des jets est reconstruite à partir de dépots d'énergie stochastiques dans le détecteur. Un nouvel outil est donc développé, pour permettre à la fois l'identification des jets d'empilement stochastiques et une amélioration globale de l'efficacité d'identification. Dans une seconde partie, l'étude de la production $WZjj$, où les bosons se désintègrent en leptons, est présentée. Un discriminant multivarié est développé, de manière à séparer de manière optimale les évènements $WZjj$-EW et $WZjj$-QCD. La méthode statistique utilisée pour l'extraction du signal est développée autour de ce discriminant, et permet la première observation de la production $WZjj$-EW, avec une signification statistique de 5.3 σ, et sa section efficace est estimée à $\sigma^{\text{fid.}}_{W^{\pm}Zjj-EW} = 0.57^{+0.14}_{-0.13}(\text{stat.})^{+0.07}_{-0.06}(\text{syst.})$.